SOLID STATE NANOPORE : SIMULATION, CHARACTERIZATION AND MOLECULAR SENSING

by

Uppiliappan Rengarajan

A thesis submitted in partial fulfillment of the requirements for the degree of

Master of Science

in

Materials Engineering

Department of Chemical and Materials Engineering
University of Alberta

Abstract

Single molecule passing through a nanopore is a process that is important in science. Some molecules develop a surface charge when diffused into a salt solution, when these molecules pass through the nanopore, they reduce or increase the ionic current. The drop or rise in the current level is dependent on the size and shape of the molecule, and consequently differs for each molecule. Hybrid nanopores, a sensing device which integrates biological and synthetic nanopores is a powerful tool for nanopore-based sensing. A detailed characterization of the synthetic or solid state nanopores is required to integrate it with biological nanopores.

In this thesis a detailed characterization of solid state nanopores is performed by comparing experimental and simulated conductance models. Solid state nanopores fabricated using Transmission Electron Microscope, ranging in size from 4 to 10 nm were measured for conductance, using Axopatch 200B. Cleanroom-based cleaning and mounting of the nanopore (and related accessories) was utilized to improve the yield of functional nanopores, prior to conductance measurements. The experimentally measured conductance was then matched with conductance obtained from finite element modeling (using COMSOL Multiphysics platform) of the electrokinetic processes occurring in a nanopore. Poisson-Nernst-Planck system coupled with Navier stokes equations was used for this purpose. The experimental and simulated conductance results of various solid state nanopores matched within an error range of $10 - 25$ % . Upon validation of the COMSOL model, the model was used for analyzing various parametric effects on conductance. Conductance dependence on pore shape and size was analyzed in detail. The simulation technique can be used to predict the required size and shape of a solid state pore for desired conductance. Effect of pore size, shape, thickness and the membrane surface charge on nanopore conductance has been discussed.

Nanopore sensing has been explored, by testing translocation of different molecules, namely, DNA, polysaccharides and proteins. Size and conformation prediction of DNA, polysaccharide molecules as they translocate through nanopores has been demonstrated. An attempt to create a hybrid nanopore, by inserting protein pore (OmpG) onto a solid

state nanopore was conducted. Protein pore(s) insertion onto the solid state nanopore with and without guiding DNA molecule was observed. Subsequently, protein partial closing and opening has also been observed, hinting at the capability of nanopore sensors to act as powerful tools in selective sensing. In summary, this thesis demonstrates the ability of simulation technique to predict the conductance of a solid state nanopore under different chemical, physical and surface property conditions of the pore. These results could be further used to fine tune the fabrication of solid state nanopores to better understand and facilitate formation of hybrid nanopores elegantly.

“ I think it’s much more interesting to live not knowing than to have answers which might be wrong. I have approximate answers and possible beliefs and different degrees of uncertainty about different things, but I am not absolutely sure of anything and there are many things I don’t know anything about, such as whether it means anything to ask why we’re here. I don’t have to know an answer. I don’t feel frightened not knowing things, by being lost in a mysterious universe without any purpose, which is the way it really is as far as I can tell. ”

- Richard P. Feynman

“ We can judge our progress by the courage of our questions and the depth of our answers, our willingness to embrace what is true rather than what feels good. ”

- Carl Sagan

Acknowledgements

I would like to thank my supervisors Dr. Carlo Montemagno and Dr. Manisha Gupta for providing me with this project. Their relentless passion and involvement towards research, inspired me to work harder. I′m grateful for the trust and freedom they bestowed on me, which made me more responsible as a researcher and as a person. Our discussions, constantly motivated me with new ideas for solving various research problems and cheered me up during my tough times. I am grateful to my committee member Dr. Dominic Sauvageau for his insightful comments on the thesis.

I would like to thank Dr. Hiofan Hoi, for preparing and taking time to explain about most of the biological substances used in this thesis. Her meticulousness in performing hands on experiments and providing attention to detail, helped me to work in a more organized fashion and re-examine my work, essentially enhancing the qualitative output.

Special thanks to Hui Qian for making all the TEM drilled pores used in the experimentation pertaining to this thesis. I would like to thank Elham Rafie Borujeny for helping to setup the COMSOL model used in this thesis, and all the nanoFAB and NINT cleanroom staffs who trained me on various fabrication techniques used in the course of this thesis. Last but not the least, I would like to thank Jeffrey Germain, Susan Kuzmak, all my friends at Ingenuity lab and at NINT for helping me on numerous occasions through this journey.

I dedicate this thesis to my mother, father, Sarana, Priya and Siva, who have always been there to support me and have taken pride in my accomplishments.

Contents

List of Figures

List of Tables

Chapter 1

Introduction

A nanopore, a hole of the order of nano, a realm at molecular level, is capable of acting as an intricate doorway for molecular passage, and thus molecular detection. Nanopores have existed in every life form for a very long time, thanks to evolution. They help in selective passage of molecules in our body. Figure 1.1 shows some of the naturally existing nano-sized biomolecules.

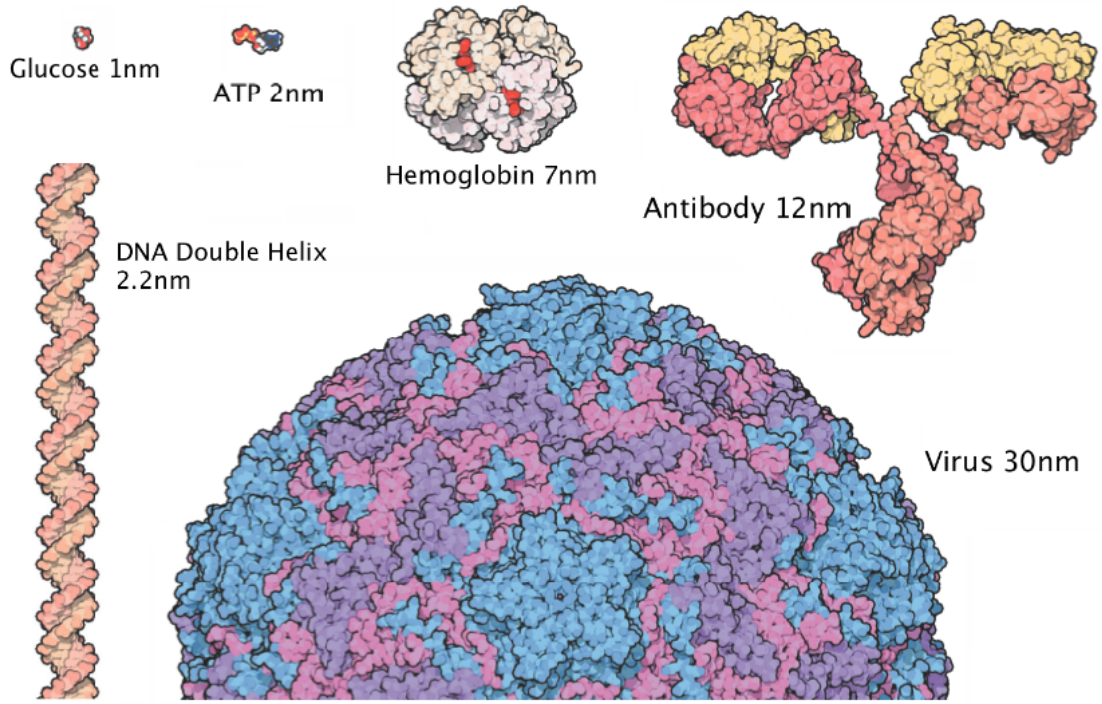

Figure 1.1: Nanometer sized molecules. Image adapted from [1].

Some of the naturally occurring nanopores include, porins (channels the passage of small molecules like amino acids, sugar and ions), potassium channels (conduct potassium ions rapidly and selectively [10]) and alpha haemolysin (secreted by bacterium *staphylococcus*,

it facilitates permeation of molecules and ions). In the past couple of decades, nanopore-based sensing has emerged as the most popular technique for molecular translocation and sequencing measurements, immunoasays and protein detection [11]. Nanopore sensing is based upon the Coulter principle, pioneered by Wallace Coulter. Patented in 1953, the principle was first applied to count blood cells by measuring change in conductance as cells passed through a small aperture [12]. Figure 1.2 shows a schematic diagram of the technique adopted by Coulter for blood cell counting. Later in 1996, Kasianowicz *et al* used the same principle for detecting Deoxyribo Nucleic Acid (DNA). They published their work describing the detection of single stranded DNA's electronic behavior while passing through α-haemolysin [13], this marked the beginning of nanopore-based molecular sensing technique.

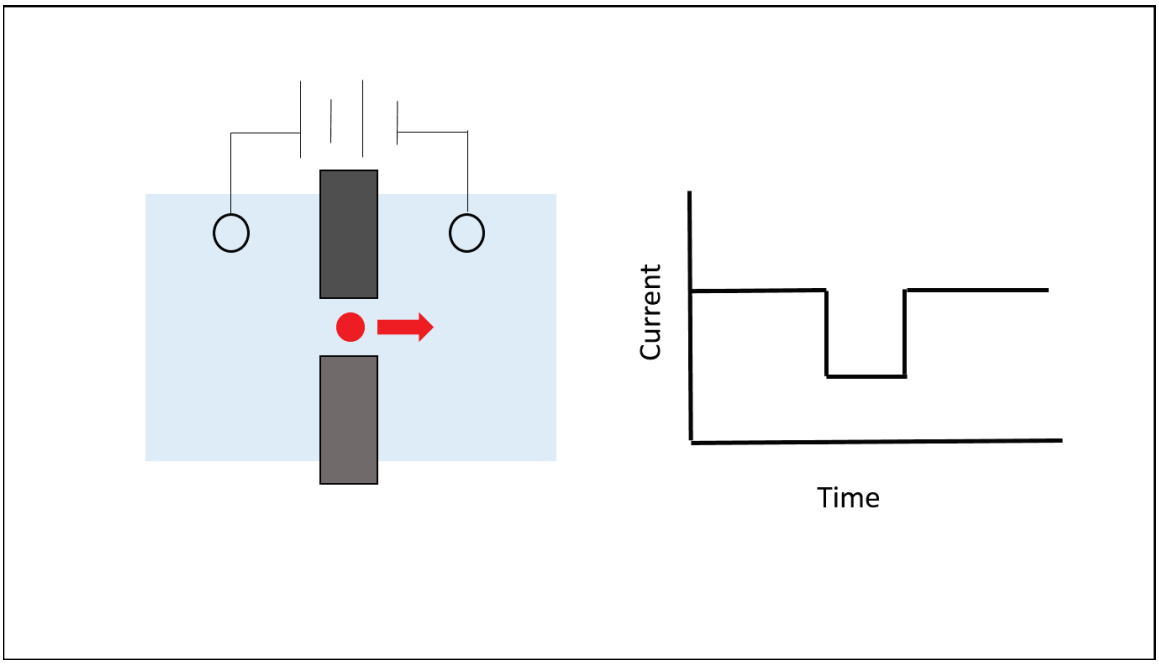

Figure 1.2: Schematic of the electrochemical blood counting method proposed by Wallace Coulter.

1.1 Motivation

Nanopores can be classified as : biological and solid state nanopores. Biological nanopores are typically protein pores, inserted onto a lipid bilayer. Most of the biological nanopores are of the oder of 2 - 3 nm in diameter and about 5 nm in length. Biological nanopores are highly reproducible in terms of size, and are congenial with chemical modification [14]. However

these advantages come with some drawbacks, they are overly sensitive to the change in ambiance, such as temperature, pH, buffer concentration change. They are also limited by a short life time and unsuited for conventional semiconductor fabrication process. Solid state nanopores are nanometer sized holes made on an insulating membrane by removing material. They are a superior alternative to biological nanopore sensors in terms of robustness and durability. They are immune to harsher chemical and mechanical environment and can be integrated with the semiconductor technology. They can also be fabricated in different sizes ranging from a single nanometer to hundreds. However, solid state nanopores suffer from poor size reproducibility, non-specificity and host a fast translocation of molecules as compared to their biological counterparts. These shortcomings on either side, has given rise to a new age of nanopores, hybrid nanopores.

By integrating a biological pore onto a solid state pore, it is possible to overcome several limitations. For the purpose of integration, a proper shape and size specific characterization of solid state nanopore is critical. This thesis presents a method to characterize the solid state nanopores by comparing them with the conductance obtained from finite element analysis, performed using COMSOL Multiphysics simulations. The effect of pore dimensions (size, shape and structure) on the conductance of solid state nanopores has been looked into in detail using the simulation technique. Size and shape control of the solid state nanopores has been done using electron beam based fabrication technique. Protocols performed in cleanroom used for the experimental characterization of solid state nanopores has proven to be highly efficient in providing a greater yield of ($> 70\%$ overall) clean nanopores that display clean and stable conductance, while in general it could be as low as 20% [15]. With the precise characterization of solid state nanopores, it is possible to reduce the time and cost spent, consequently making solid state nanopores more approachable for a wide array of potential applications such as molecular detection, molecular sequencing, molecule seperation, bio-computing, and other sensing fields. The motivation behind this thesis is the final goal of being able to construct hybrid nanopores, by precise fabrication and characterization of nanometer or sub-nanometer sized solid state nanopores.

1.2 Outline

Outline for rest of the thesis is presented here,

Chapter 2 discusses the various techniques used for solid state nanopore fabrication, nanopore-based measurement techniques and proceeds to discuss the applications. The

chapter also provides a theoretical insight on the characterization of solid state nanopores, and a discussion on the various physics involved in the electrokinetic modeling done using COMSOL Multiphyscis platform.

Chapter 3 discusses the fabrication of solid state nanopores from the wafer level to the pore, and how the fabricated pore is processed for experimental characterization through a series of articulate cleaning and conditioning steps, including the detail on instrumentation and experimental setup. The chapter also discusses the setup of COMSOL Multiphysics model that has been used in rest of the thesis for solid state nanopore characterization purposes, describing the construction of pore geometry, physics involved, mesh structure, etc.

Chapter 4 discusses the conductance-based characterization results performed using experiments and simulations. Followed by a detailed discussion on the effect of pore shape, structure, geometric dimensions and surface charge on conductance of the nanopore. The chapter concludes with a discussion on molecular sensing results from nanopore sensing experiments.

Chapter 5 summarizes the thesis, and presents a few concluding remarks. The chapter also discusses a few ongoing and future projects intended towards enhancement of the nanopore-based sensing platform.

Chapter 2

Literature Review and Background

In order to study and characterize solid state nanopores, it is necessary to understand and review the different techniques involved in nanopore fabrication and measurements. Also, the study on applications of solid state nanopore-based sensing provides an insight on its capabilities. This review on different techniques and applications is then followed with a theoretical discussion on characterization of solid state nanopore. The final section of the chapter describes the physics involved in electrokinetic model build up for solid state nanopore-based numerical measurements.

2.1 Fabrication of solid state nanopores

Solid state nanopores are made by removing material on a insulating free standing membrane. Three types of techniques are generally used for fabricating solid state nanopores, namely, ion beam sculpting, e-beam sputtering and chemical etching techniques.

2.1.1 Ion beam Sculpting or Focused Ion Beam

Ion beam sculpting or focused ion beam (FIB) was the first technique to be used for making solid state nanopores. In 2001 Li *et al* [2] used a 3 keV Ar^+ ion beam to sputter out bowl shaped pores of the order of 10 - 100 nm. Figure 2.1 shows the schematic diagram of ion beam sculpting technique used by Li *et al*. Ga^+ ion has been used to make pores in the pore size range of 20 - 100 nm (pore size refers to diameter of the pore in rest of the thesis, unless otherwise mentioned) using $\sim$ 30 keV beam. Ga^+ ion owing to its heavier size causes deposition [16] in the substrate, which is undesirable for nanopore sensing. He^+ ion has been used for pore thinning and pore making at sub-nanometer precision, owing to the smaller size of helium [17]. He^+ ion has been used a lot recently, to make single nanometer sized pores. Ion beam technique has been used to make pores on SiN_x, SiO_2

and SiC membranes [2,18–22]. FIB directly drills the surface to open a pore, pore shrinking happens when pore size is smaller than membrane thickness and is facilitated more easily by heavier ions [23]. FIB has generally been used to make pores bigger than 15 - 20 nm in size.

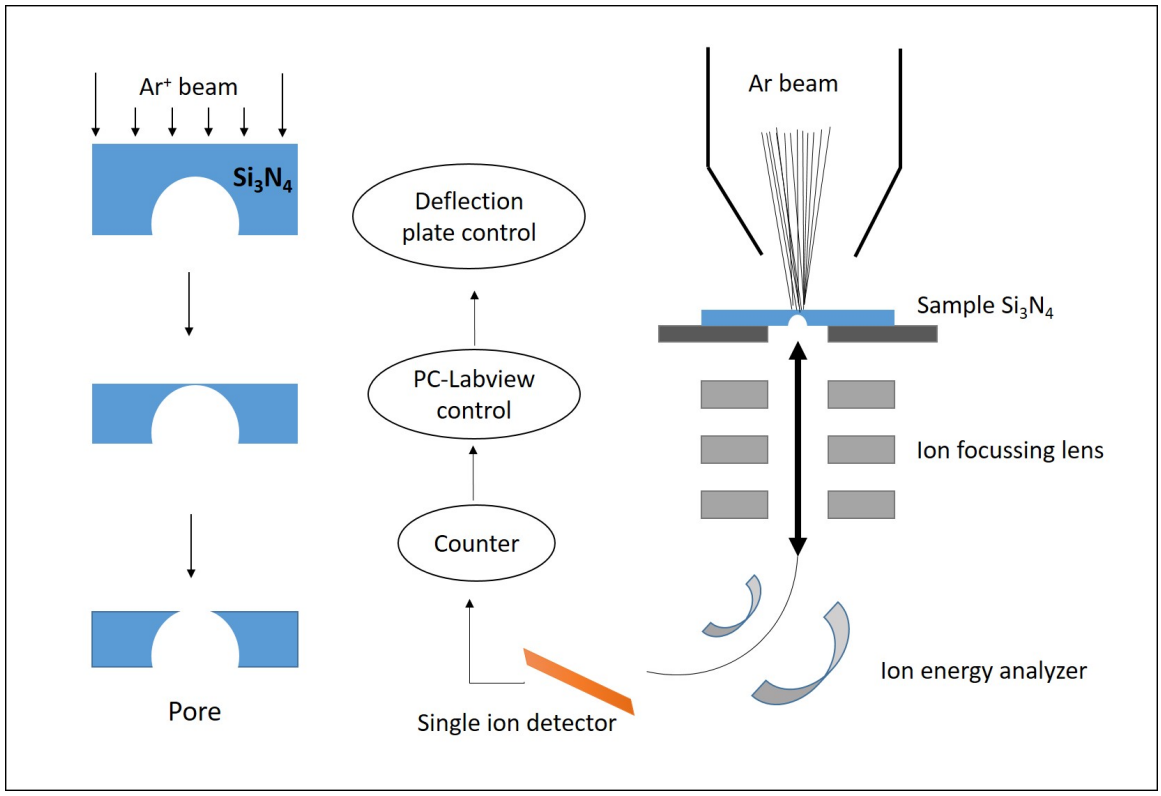

Figure 2.1: Schematic of ion beam sculpting technique with Ar^+ ion. Image adapted from [2].

2.1.2 e-beam based sputtering

Electron beam or e-beam was first used by Storm *et al* in 2003 for drilling a nanopore directly on a SiO_2 membrane [24]. They used e-beam lithography to pattern the pore size to 20 nm and used Transmission Electron Microscope (TEM) for further shrinking or expansion of the nanopore. Nanopores of the order of 2 - 200 nm can be fabricated using TEM depending upon the thickness of the membrane [24–27]. Nanopore expansion is observed with high intensity e-beam, and surface tension driven shrinking has been observed to occur at low e-beam intensities [28]. Scanning Electron Microscope (SEM) has also been used to make pores, in the size range of 50 - 200 nm, and further shrunk to 10 nm [29]. Typical membrane materials subjected for e-beam pore fabrication include SiN_x, Al_2O_3, SiO_2 and graphene. TEM has mostly been used to make pores of size 2 - 15 nm. This size range is

also more suitable for hybrid pore applications. We have used both ion beam and e-beam based drilling for our research here. As we are more interested in smaller nanopores in the size range of 2 to 5 nm, e-beam has been explored more than FIB.

2.1.3 Chemical etching

Chemical etching or wet etching is used for making nanopore arrays and larger nanopores of conical and pyramidal shapes [30] as compared with e-beam and ion beam techniques. Wet etching technique is employed on materials like Si and SiO_2. Conventional lithography and deposition techniques are used to pattern the material and further anisotropic etching is done in an alkaline medium (like KOH). Nanopores made using chemical etching techniques are generally not desirable for sensitive molecular detection experiments, owing to the large size. Hence, this technique was not pursued for the purpose of this thesis.

2.2 Detection techniques used in nanopore sensing

For the nanopore to act as a sensor, it requires a platform to function upon. The major nanopore sensing technique used by most groups working in this field is ionic current variation-based variation. The following are some of the generally used electrical detection techniques.

2.2.1 Ionic current variation-based detection

This technique is based on the Coulter principle. The nanopore is mounted onto an enclosure and sandwiched between two electrolytic reservoirs, with the pore acting as the only path between the two reservoirs for fluid to flow. A potential bias is applied across the pore and charged molecules added to one of the reservoirs are electrophoretically driven through the nanopore. The translocation of the polymer or molecule is then observed as a change in observed current. For a negatively charged analyte like DNA, this change is in the form of a blockade. Figure 2.2 illustrates the working of ion blockade technique. This technique has been most widely used for nanopore sensing and analysis. All the experiments in this thesis are based on the ionic current variation-based detection technique.

2.2.2 Detection method based on capacitance variation

This technique uses Metal Oxide Semiconductor (MOS) capacitor integrated into the nanopore for charged molecule detection. The technique was primarily proposed for DNA detection and sequencing [4]. The setup is similar to the previous technique, along with additional

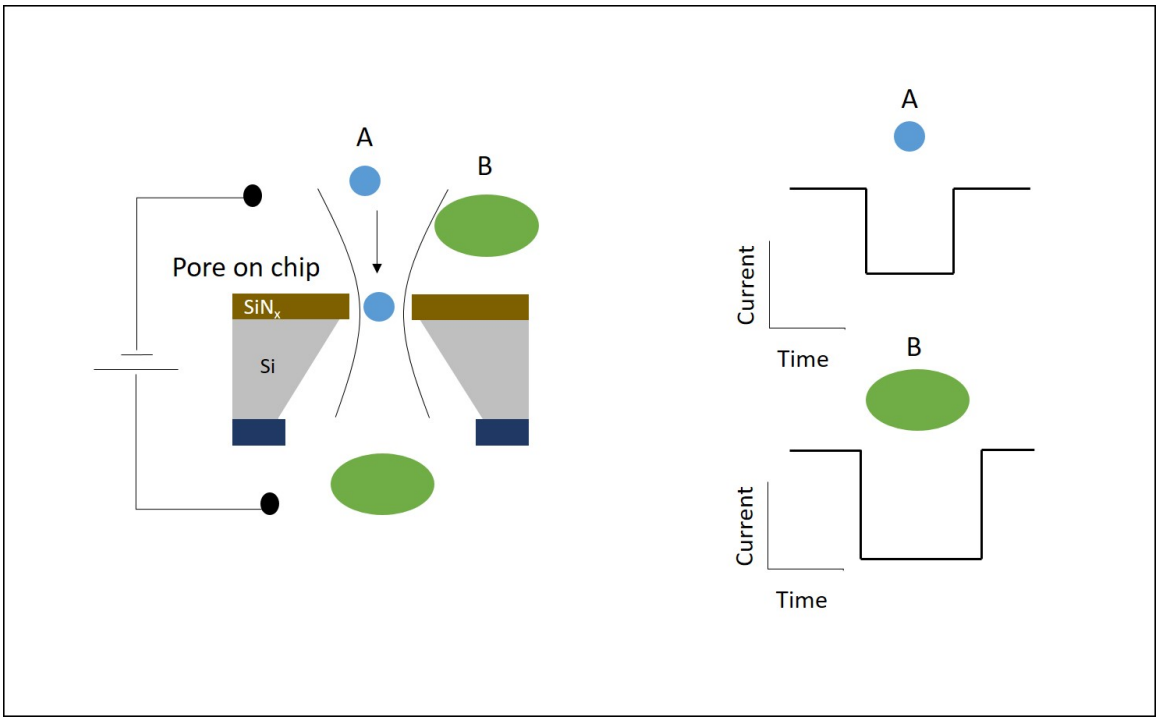

Figure 2.2: Schematic of ion current blockade, illustrating the different blockades observed for different types of molecules depending on its size, structure. A,B are two different molecules displaying different current blockade.

layers of materials incorporated at the pore region for the construction of a capacitor. As the DNA polynucleotide translocates through the pore, it polarizes the capacitor owing to the charge on the bases. Each base has a unique charge, triggering unique voltage levels. Due to experimental and fabricational difficulties [4, 31], the field remains to be explored for practical applications. Figure 2.3 shows a schematic of DNA translocation through a capacitor nanopore [4].

2.2.3 Tunneling current based detection

This technique was specifically proposed for DNA sequencing. The setup is similar to ionic current variation technique, additionally a couple of nanometer-scale electrodes are placed around the nanopore region. As the nucleobases of a DNA strand pass between the electrodes, a tunneling current is produced, and this current is theoretically specific for each base, since each base has a different chemical and electronic structure. Figure 2.4 shows a schematic diagram of how the tunneling current technique works. For DNA sequencing purposes, the thickness of tunneling electrodes and the pore needs to be $\sim$ 0.4 nm [13]. Also, the rate of base movement through pore must be slower than time resolution of ionic

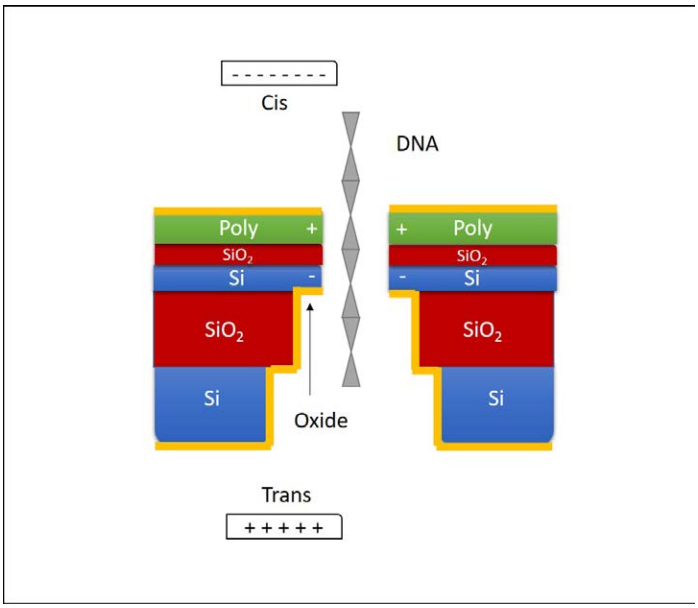

Figure 2.3: Schematic of DNA translocation through a capacitor nanopore. *Cis* and *trans* represent the two electrolytic reservoirs which sandwich the pore, and the '+' and '-' signs the respective bias. Image adapted from [4]

current measurement system [13] and each base must produce a unqiue current blockage [13]. Graphene has been identified as the most promising material for the electrode [32], owing to its ability to be designed at subnanometer precision. The technique still faces a lot of experimental [33, 34] and fabricational difficulties, and remains to be explored.

2.3 Applications of solid state nanopore

Owing to the elegant operating principle of solid state nanopores, a rapid development in nanopore-based sensing is on-going. Nanopores could be used for molecular detection, understanding molecular interactions and could go as far as replicating the functions of biological systems. The ability of a solid state nanopore to sense the presence of a charged foreign molecule, has been put to use into three broad categories [23].

2.3.1 Molecular translocation

As explained in the introduction section, molecular translocation is a regular process in biological system. Translocation of molecules or polymers through solid state nanopores, has been observed by different groups working in the field [35, 36]. The length and size of the translocating molecule respectively corresponds to the duration and amplitude of the drop (or peak) observed in the recorded current. Several linear [13] and exponential relation

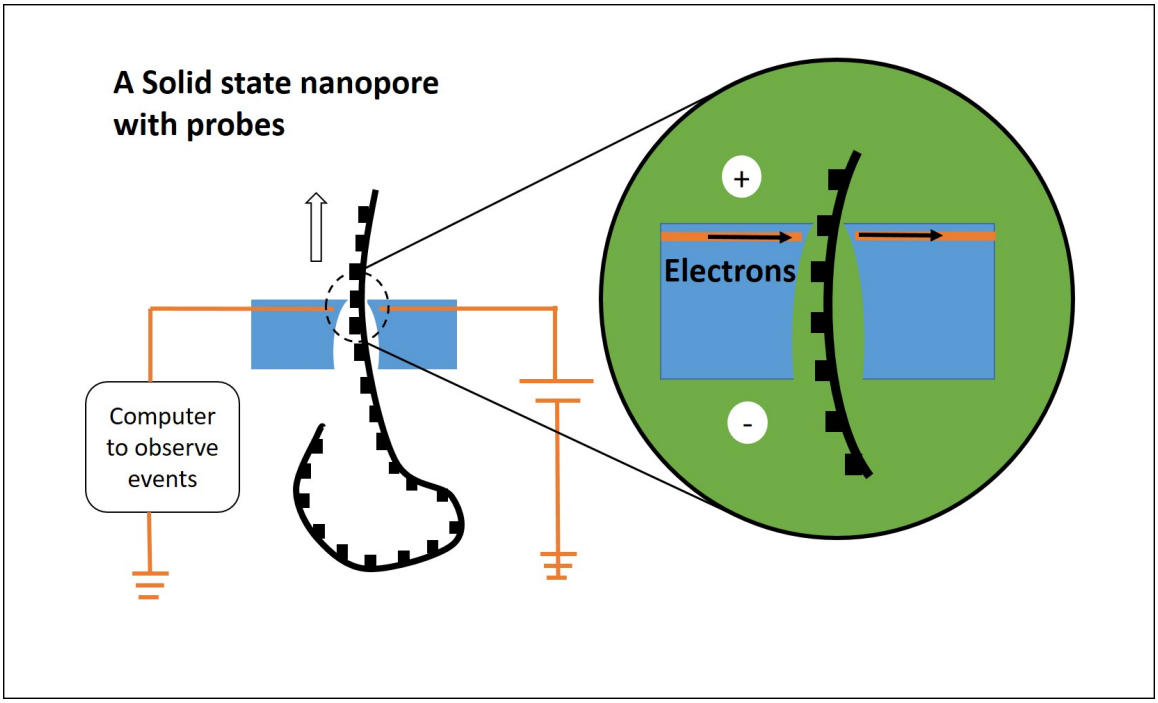

Figure 2.4: Schematic of tunneling current read out as DNA strand translocates between the pore, electrodes. Image adapted from [5].

between the length of translocating molecule and duration of drop have been proposed. The speed of the translocating molecule is dependent on various factors such as hydrodynamic drag, electrical driving force, and the size and shape of the pore [37]. In general, a longer molecule displays a longer translocation duration and a larger molecule displays a larger current blockade. The conformation of the translocating molecule could also be derived from the structure of the current drops. While a folded molecule displays a larger current drop, an unfolded molecule displays a shorter drop amplitude [24]. Figure 2.5 illustrates the different conformations of an analyte and the corresponding current drop.

2.3.2 DNA sequencing

The ability to sequence DNA provides information about genetic code. DNA sequencing contributes to critical advancements in various fields like biology, medicine, forensics and other sciences. DNA strands are composed of the four nucleobases, Adenine (A), Thymine (T), Guanine (G), Cytosine (C). Each base has a specific charge and size, which would result in a unique current blockade for each base as it translocates through a nanopore. DNA sequencing is one of the most attractive applications of nanopore sensing. DNA sequencing

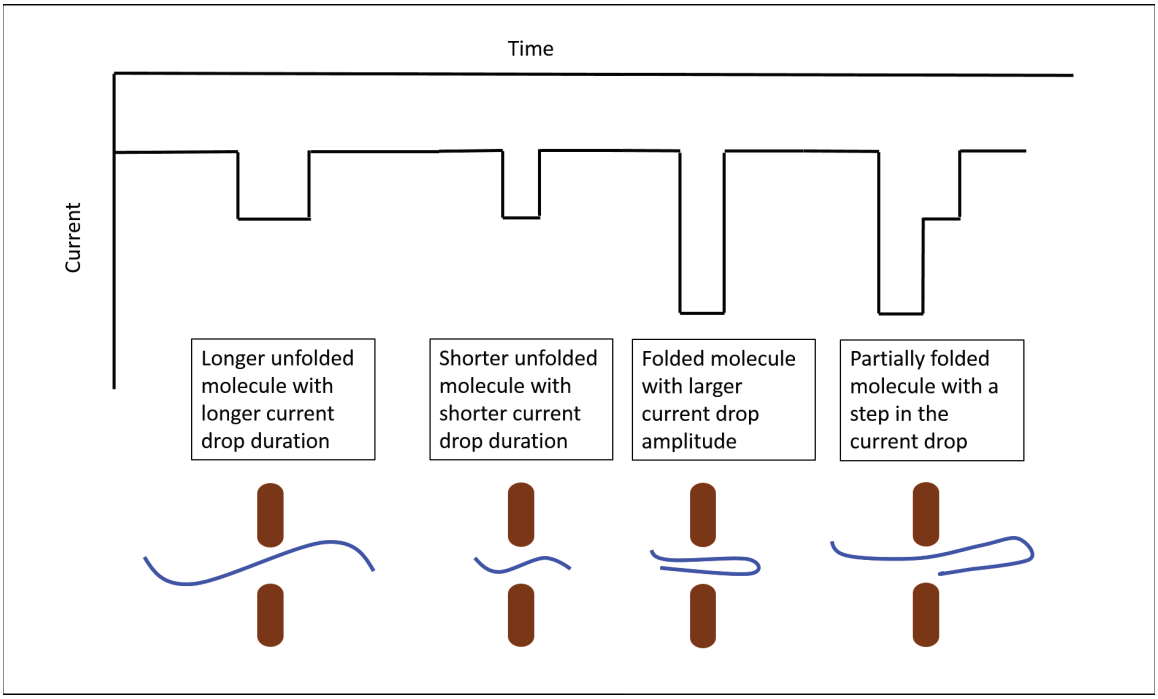

Figure 2.5: Schematic of different analyte conformations as it passes through the solid state pore and the corresponding expected current drops.

was first proposed by Sanger *et al* in 1977 [38]. Several other techniques like Illumina and Ion Torrent sequencing have been used, but nanopore devices show great advantages in terms of cost, speed, through-put and sample quantity. Li *et al* [39] first demonstrated the capability of solid state nanopores for DNA sequencing applications. α-haemolysin inserted onto a synthetic membrane has been predominately used for DNA sequencing [40].

2.3.3 Protein detection

The conversion of normal protein to misfolded ones, has been reported to be the reason for many diseases [41]. A solid state nanopore could be used to analyse the size, conformation and charge at single protein molecule level. Protein detection using nanopores could be used to understand conformation changes [11].

Here some studies have been performed using solid state nanopores for DNA, polysaccharide and protein measurements.

2.4 Hybrid nanopore

Hybrid nanopores with both biological and solid state counterparts, filters out the shortcomings of either nanopores as discussed in the introduction chapter. In 2010, Hall *et al*

successfully inserted α-haemolysin (attached to a 3Kbp dsDNA, which acted as a guide) onto a SiN_x nanopore ($\sim$ 3.6 nm in diameter) [6]. The hybrid pore displayed higher robustness, with the biological pore portraying superior control on translocating DNA. Figure 2.6 shows the schematic of step by step insertion of α-haemolysin onto solid state nanopore, and the corresponding current drop adapted from Hall *et al*'s work.

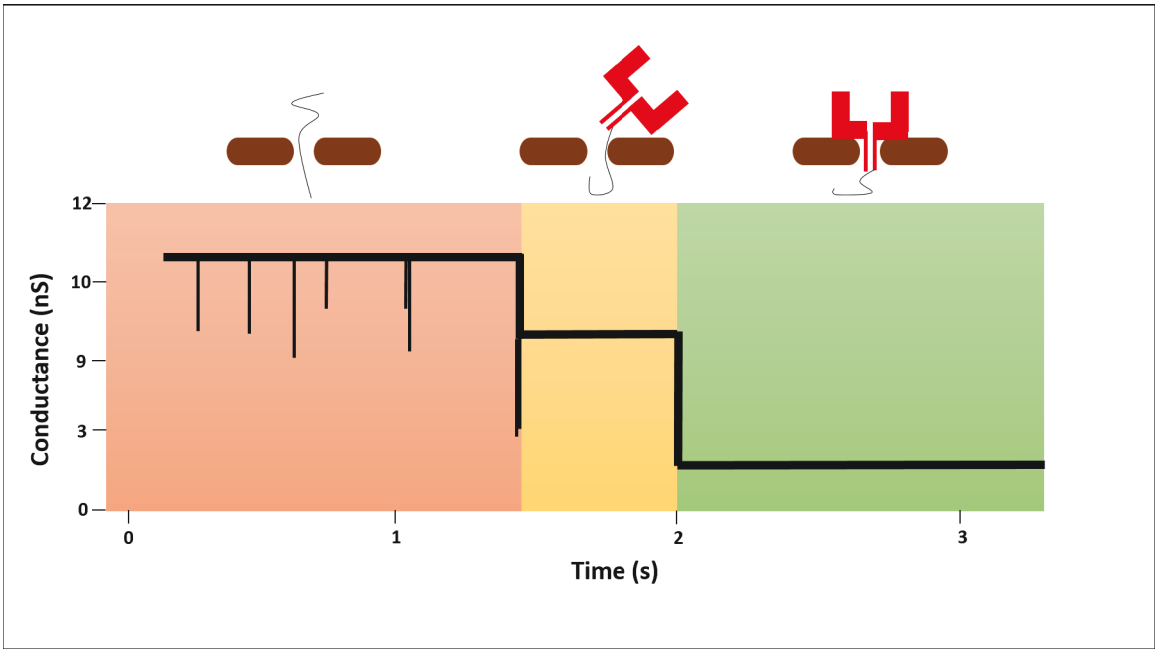

Figure 2.6: Schematic of step by step insertion of α-haemolysin onto solid state nanopore, and the corresponding current drop (Hall *et al* [6]). The mushroom shaped, red color structure indicates α-haemolysin and the black thread indicates the guiding dsDNA. Image adapted from [6].

Other hybrid pore structures have also been proposed, Yusko *et al* coated a lipid bilayer onto a SiN_x nanopore, the size of the nanopore was tuned (varied by $\sim$ 1.4 nm) by varying the temperature to shrink and expand the lipid. Protein translocation speeds were observed to be reduced by this technique [42]. Further theoretical and experimental work is required to test the design [43]. Similarly, hair pin loop DNA coated solid state nanopore structures have also been developed, to enhance interaction with translocating DNA, thereby slowing it for improved measurement resolutions [44].

2.5 Solid state nanopore characterization

The solid state nanopore can be represented by a simplified equivalent circuit as shown in Figure 2.7. The nanopore acts like a resistance, the insulating membrane bearing the pore

acts like a capacitance, with surface charge on either side. The membrane capacitance can be approximated to,

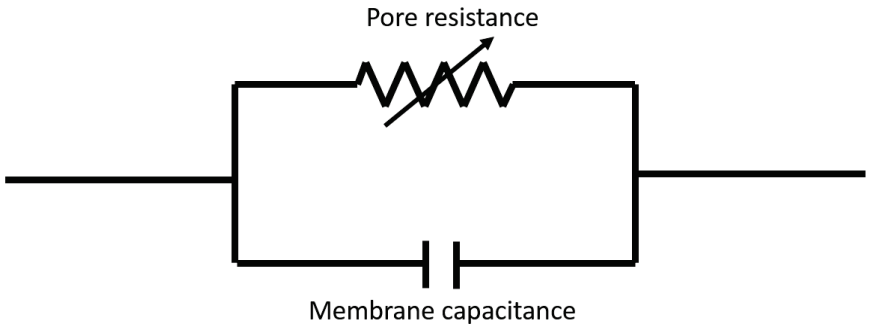

Figure 2.7: Equivalent circuit of a solid state nanopore

$$C_{membrane} = \epsilon_0 \epsilon_r \frac{A}{t} \tag{2.1}$$

where A is the area of the insulating membrane, t is the thickness of the insulating membrane, ϵ_0, ϵ_r are permittivity of vacuum and relative permittivity of the insulating membrane material respectively. The smaller the membrane capacitance, the smaller is the noise contribution [45].

Consider a cylindrical nanopore in an insulating membrane placed between two electrolytic reservoirs with a resistivity ρ. The resistance of the pore is given by,

$$R_{pore} = \rho \left(\frac{4l}{\pi d^2} \right) \tag{2.2}$$

where, R_{pore} is the pore resistance, ρ is the resistivity of the electrolytic liquid at temperature T, l and d are the thickness and diameter of the pore respectively. We also have the access resistance along the convergent path from the bulk (reservoir region, to account for the electrolyte and electrode resistance) to the pore [7], given by,

$$R_{access} = \frac{\rho}{2d} \tag{2.3}$$

where, R_{access} is the access resistance, the conductance of the pore is then given by the

inverse of the total resistance (which is the sum of Equation 2.1 and twice Equation 2.2),

$$G = \sigma \left[\frac{4l}{\pi d^2} + \frac{1}{d} \right]^{-1} \tag{2.4}$$

where, G is the conductance of the pore and σ is the conductivity of the electrolytic fluid at temperature T. Equation 2.4, proposed by Kowalczyk *et al* [7], is most widely used analytical model for solid state nanopore conductance estimation. However in reality, the pore shape is rarely a perfect cylinder. Pore shape specific models have been proposed by different groups [7,28,46], for their respective experimental data. However these models are experiment specific and also do not take into account the surface chemistry arising out of the surface charge on the pore surface. Frament *et al*, proposed more rigorous analytical models for a few shapes, taking into consideration nanopore geometry and surface chemistry in their study to determine the shape and size based on conductance [47]. However, unsymmetrical shapes (for example cone shaped pore, portraying ion current rectification) were not studied, and a good correlation between the pore shape and conductance required further research [47].

2.6 Electrokinetics in a nanopore

Some commonly encountered electrokinetic phenomena are,

- **Electroosmosis** is the movement of an ionic solution relative to a stationary charged surface, due to an externally applied electric field.
- **Streaming potential** is the reverse of electroosmosis. When the ionic solution is made to flow relative to a stationary charged surface by applying an external pressure, an electric field is created.
- **Electrophoresis** is the movement of a charged particle or surface relative to a stationary liquid, due to an applied electric field.
- **Sedimentation potential** is the electric field created when charged particles move relative to a liquid, due to gravitational or centrifugal fields.

COMSOL Multiphysics has been used in this thesis to model the electrokinetic processes in the nanopore. This section is a discussion on the physics governing the transport processes through a nanopore. Classical continuum physics has been proven to work for pore

sizes beyond ~ 2.2 nm [48, 49]. The following physics, have been effective in describing the processes happening in a nanopore immersed in an electrolytic solution [50, 51], Poisson′s equation governing the electric potential, Nernst-Planck equation governing the ion concentrations and the Navier stokes equation governing the fluid flow. A coupled solution of the above described physics, is obtained to understand the processes at a nanopore.
Poisson′s equation governing the space charge density ρ_v dependent electric potential V, is given by,

$$\nabla^2 V = -\frac{\rho_v}{\epsilon_0 \epsilon_r} \tag{2.5}$$

where ϵ_0, ϵ_r are the permittivity of free space and material dependent relative permittivity respectively. The space charge distribution is related to the molar ionic concentrations by,

$$\rho_v = F \sum_i (z_i c_i) \tag{2.6}$$

where F is the Faraday constant, z_i and c_i are the valence and molar concentration of species i respectively.
Nernst-Planck equation governs the flux J_i of an ionic species i. The equation is made up of three different contributions. The flux due to concentration gradients, given by Fick's first law,

$$N_{i,D} = -D_i \nabla c_i \tag{2.7}$$

where $N_{i,D}$ is the flux due to diffusion, as a result of Brownian motion of molecules. D_i is the diffusion coefficient of species i. When a potential gradient is applied onto an electrolytic system, the mass transport of the charged species contributes to the transport flux or migration flux. The migration flux $N_{i,M}$ is given by,

$$N_{i,M} = c_i w_i F_{ext} \tag{2.8}$$

where, w_i is the mobility of the species i and F_{ext} is the external force acting on the molecules. Einstein assumed that the species move at a terminal velocity under the effect of friction from surrounding medium and external force, the mobility is then given by, $w_i = D_i/k_B T$, and the external force for an ionic system under the effect of an electric field is given by, $F_{ext} = q_i E$ and $q_i = z_i e$, $E = -\nabla V$, k_B is the Boltzmann constant, T is

Temperature, q_i the charge of species i, e is the elementary charge and E the electric field. Equation 2.8, can then be given by,

$$N_{i,M} = -\frac{z_i e c_i D_i}{k_B T} \nabla V \tag{2.9}$$

The final contribution comes in from the convective flux $N_{i,C}$, with a fluid velocity of u is given by,

$$N_{i,C} = c_i u \tag{2.10}$$

In conventional electrochemistry, Faraday constant F is used instead of elementary charge e and the universal gas constant R instead of Boltzmann constant k_B. Also e/k_B can be written as F/R. The Nernst-Planck equation is then the sum of all the flux contributions given by,

$$N_i = -D_i \nabla c_i - z_i \left(\frac{D_i}{RT} \right) F c_i \nabla V + u c_i \tag{2.11}$$

The fluid flow in a Newtonian fluid is described by the continuity (Equation 2.12) and momentum (Navier-Stokes, Equation 2.13) Equations, given by,

$$\frac{\partial \rho}{\partial t} = -\nabla.(\rho u) \tag{2.12}$$

$$\rho \frac{\partial u}{\partial t} + \rho u.\nabla u = -\nabla P + \mu \nabla^2 u + f_{ext} \tag{2.13}$$

where ρ is the fluid density, t represents time, p is the fluid pressure, μ the fluid viscosity and f_{ext} represents any other body force (per unit volume) acting on the fluid. For steady incompressible fluid flow, the fluid density is independent of time and Equation 2.12 reduces to $\nabla.u = 0$. Each term on Equation 2.13 represent a force acting on unit volume of fluid. $\rho \frac{\partial u}{\partial t}$ gives the rate of change of momentum, which can be removed for steady state conditions. The term $\rho u.\nabla u$ is due to fluid inertia. ∇P gives the contribution of pressure and the term, $\mu \nabla^2 u$ measures viscous momentum transport. In electrokinetic transport processes, devoid of gravity effects, the electric field is the only external volume force $F_v = f_{ext}$ and

$F_v = -F\sum_i(z_i c_i)\nabla V$. The reduced Navier stokes equation is then given by,

$$\rho u.\nabla u = -\nabla P + \mu\nabla^2 u - F\sum_i(z_i c_i)\nabla V \tag{2.14}$$

In a typical finite element modeling-based, electrokinetic problem, the above discussed physics are coupled and solved simultaneously to observe and analyze the processes in the system under study, in this case a solid state nanopore.

Chapter 3

Fabrication, Experimental and Numerical Model Setup

Solid state nanopore characterization required the fabrication of a device, an experimental setup and the setup of numerical model. For this purpose, free standing silicon nitride (SiN_x) membranes were built on a silicon base using conventional fabrication techniques, like lithography, chemical deposition, wet and dry etch. Nanopores ranging in size from 4 to 10 nm were then drilled using Transmission electron microscope (TEM) on several membranes. Fabricated pores were then systematically cleaned and mounted onto a specially designed cell for conductance determination and molecular sensing experiments. The numerical electrokinetic model used to characterize the conductance of nanopores was setup using the COMSOL Multiphyscis platform. The results of all the numerical studies presented in this thesis was performed using COMSOL Multiphysics, until otherwise specified.

3.1 Fabrication

Fabrication of nanopore, was a two-step process : fabrication of free standing membrane and drilling of pores on the membrane. The process flow of the fabrication involved and difficulties faced are discussed in this section.

3.1.1 Free standing membrane fabrication

The first step involved the fabrication of free standing $SiNx$ membrane. 50 nm thick double-sided, LS LPCVD SiN_x (Low stress silicon nitride deposited using Low pressure chemical vapor deposition) coated 4", 525 $\pm$ 25 μm thick silicon (Si) wafers, cut along $\langle 100 \rangle$ plane orientation was purchased from Rogue Valley Mircodevices. The SiN_x coated silicon wafers were used to fabricate free standing SiN_x membranes. The following processing steps were performed in a class 1000 Cleanroom.

- The wafers were cleaned in freshly prepared Piranha solution (96% H_2SO_4 : 30% H_2O_2 in 3:1 ratio) for 20 minutes, to render the surface free off organic materials. Proper acid gear was worn to prevent any piranha spill on the body.

- Plasma enhanced chemical vapor deposited (PECVD) SiN_x was coated onto one side of the silicon wafer using Orion III PECVD from Trion Technology. Typical deposition time for 1 μm coating is around 27 minutes at 40 W RF power, 500 mT pressure, 300° C temperature. The flow rates of different gases used were 40 sccm NH_3, 55 sccm N_2, 25 sccm DES. This layer of SiN_x acted as good substrate and as a mask for patterning and etching the silicon underneath.

- Photo-lithography was used to pattern and create openings on the PECVD SiN_x for further etching of silicon. L-Edit was used to create the layout for photomask fabrication. Photomask used for this process is shown in Figure 3.1. The dark

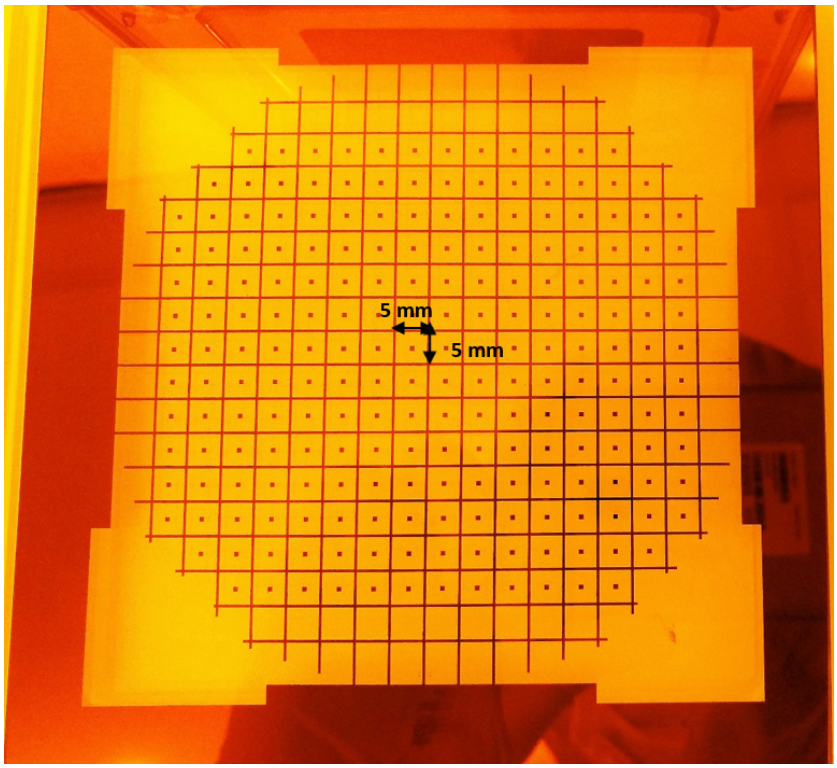

Figure 3.1: Mask layout used for photo-lithography.

brown part of the mask is chromium and the transparent part is glass. The mask was designed to have grooves between the 5 x 5 mm chips to enable easy separation after etching. AZ 5214 photoresist was used to pattern the SiN_x, 5 - 10 mL of the photoresist was spin coated onto the PECVD SiN_x at spread speed of 500 RPM for 10

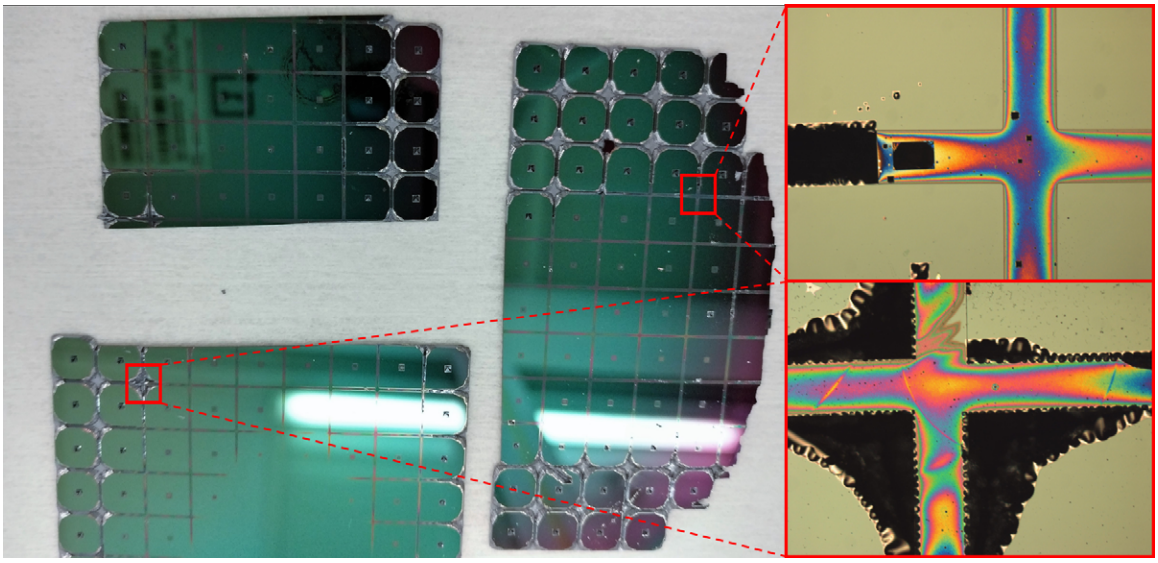

Figure 3.2: Failed photo-lithography image. Typical result of resist cross linking in unexpected regions, causing improper/wrong patterning of SiN_x. Zoomed out images show the etching of silicon at unexpected regions leading to undesired patterns.

s and spin speed of 4000 RPM for 40 s. The resist was then soft baked at 90° C for 90 s. The resist was then UV exposed under the mask for 4 s at 64 mW.cm^{-2} for pattern transfer. A post exposure bake was performed at 118° C for 120 s. The temperature and time of this bake is critical [52]. A higher temperature of 130° C resulted in the resist cross linking in unexposed regions, providing no pattern. On the other hand, a lower temperature of around 110° C resulted in improper cross linking. A typical result of improper resist cross linking is shown in Figure 3.2. Finally a flood UV exposure (without mask) of the resist was done for 60 s, to easily remove the unlinked resist. Alternatively, the chromium and glass regions in the mask could be swapped during mask making, to schedule an easier single step lithography process. MF CD 319 developer was used to remove the unlinked resist.

- The patterned SiN_x surface was then etched by Reactive Ion Etch (RIE) for 220 s at 125 W radio frequency (RF) power, 150 mT pressure, 45 sccm CF_4, 5 sccm O_2 using Phantom III RIE from Trion Technology.

- The exposed silicon was etched anisotropically in a 32% potassium hydroxide (KOH) solution for 5 hours and 40 minutes for a typical silicon thickness of 525 m at an etch rate of 1.6 μm/min. Isopropyl alcohol (IPA), 10% by volume, was added to the bath to minimize surface roughness, the bath was maintained at 85° C throughout the etching process. KOH etches silicon preferentially along the (100) plane at 54.7°,

leaving out 50 nm thick free standing SiN_x membranes, ranging from 50 to 80 square μm in dimension. The smaller solid squares in the mask in Figure 3.1 are the actual size of SiN_x openings, which provide the doorway for KOH to etch through the silicon wafer (for further information on free standing SiN_x dimension calculation, refer to Appendix A).

- As a final step, the individual 5 x 5 mm chips, each holding a free standing membrane were cleaved out in a solvent atmosphere, IPA was used for this purpose. It was observed that the solvent atmosphere prevented formation of debris on the surface of the chip during cleaving. The silicon etch is not fully through at the edges of each 5 x 5 mm (refer Figure 3.1) chip, leaving the wafer intact with all the chips. Carbon fiber tipped tweezers were used to handle the chips. Steel tipped tweezers caused severe damage to the edges of the chips, steel being harder than silicon. The debris from this damage tends to stay on the membrane, making it difficult to fabricate pores on the surface. Post pore fabrication handling of the chip using steel tweezers sometimes resulted in pore blockage. Neither Piranha nor plasma cleaning (Ozone plasma) was found to be effective in removing the debris. Figure 3.3 shows a typical chip damage caused by steel tweezers.

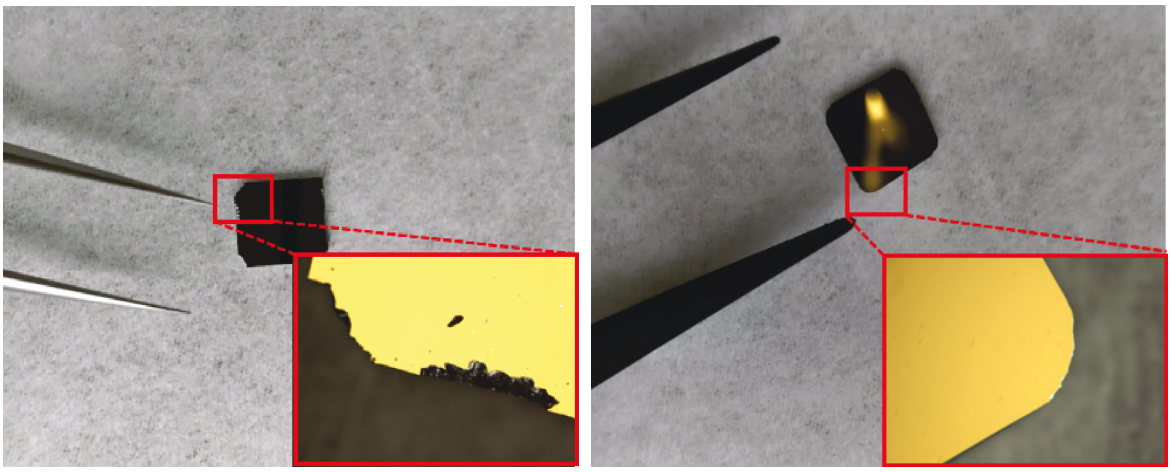

(a) (b)

Figure 3.3: Chip handling with tweezer. (a) Chip with damaged edges caused by Steel tweezer; inset shows zoomed in image of the damage under a microscope. (b) Clean edge when carbon fiber tipped tweezer was used to handle the chip; inset shows zoomed in image of edge.

Fabricated free standing membrane bearing chips were safely sorted and placed in a cleanroom environment.

3.1.2 Nanopore fabrication

A single nanopore was drilled on each free standing membrane. In order to be able to integrate the solid state nanopores with biological pores, they needed to be as small as possible (< 5 nm). Nanopore fabrication was attempted using two different pore making techniques, ion beam (FIB) and electron beam (TEM)

3.1.2.1 Focused Ion beam

Pore fabrication was initially attempted using focused ion beam sculpting. 30 keV, Ga^+ ion beam was used to make pores on a 75 nm thick SiN_x membrane (these SiN_x membranes were deposited using PECVD, specifically for FIB based pore drilling tests, and are different from the LPCVD coated 50 nm thick membranes used in the experiments). The fabricated pores varied in size from 40 nm to 100 nm, and were found to be too large for the purpose of this thesis. Figure 3.4 shows SEM images of pores fabricated using Ga^+ ion beam.

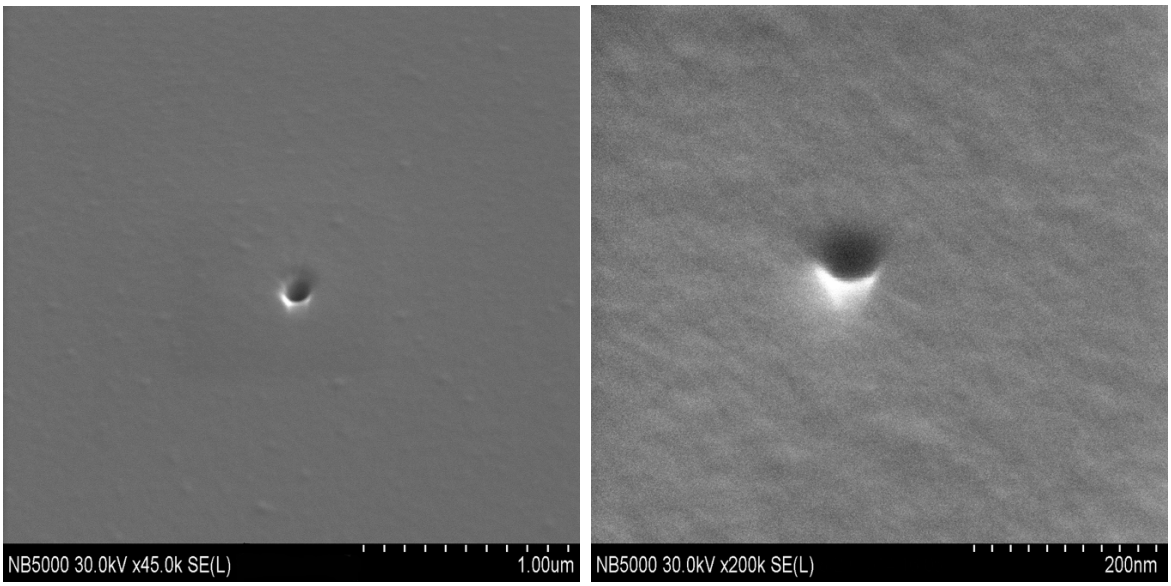

(a) (b)

Figure 3.4: Pores fabrication using 30 keV, Ga^+ ion beam on a 75 nm thick SiN_x membrane, with pore sizes (a) 100 nm and (b) 40 nm.

3.1.2.2 Transmission electron microscope

Pore fabrication was finally done using JEOL2200 FS TEM, by drilling out hour-glass shaped nanopores out of the 50 nm thick free standing SiN_x membranes. Nanopores with sizes in the range of $4 - 10$ nm were drilled using a 200 keV beam, beam current of 15 nA,

at a magnification of 800,000x. The time for pore formation varied from $1 - 3$ minutes for pores in the size range of $4 - 10$ nm. The working procedure for pore making was adopted from the work by Min Jun Kim *et al* [28]. Tomography was performed to predict the pore structure, which was found to be a hour-glass shaped as shown in Figure 3.5(c). Figure 3.5(a),(b) shows the pore images of a 4 and 6 nm pore respectively. Fabricated pores were safely secured in class 1000 cleanroom environment.

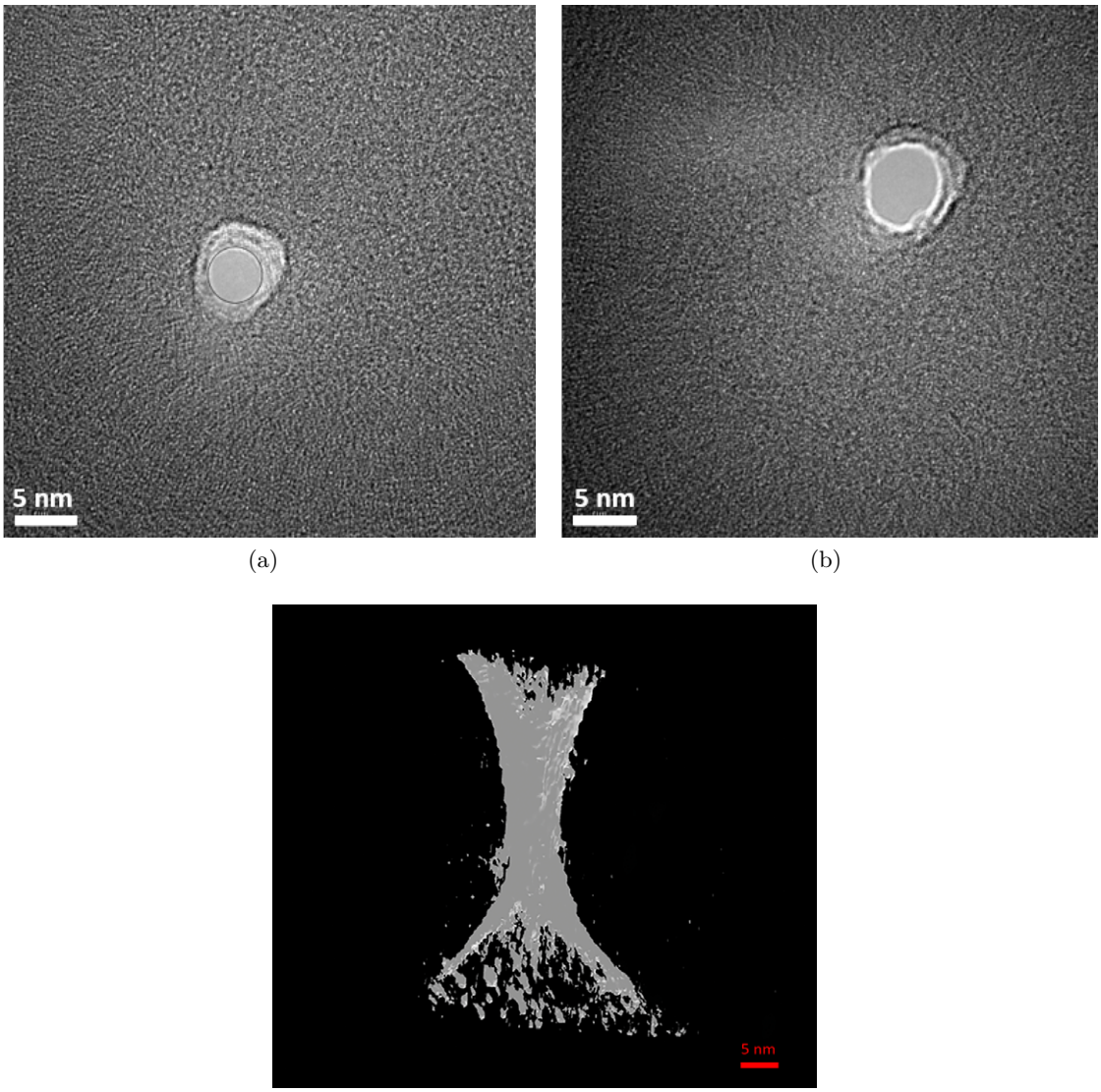

(a) (b)

(c)

Figure 3.5: Characterization of pores made using TEM. TEM pore images of a (a) 4 nm pore and (b) 6 nm pore, (c) Tomography analysis on the pore shows the hour-glass shape of the pore.

Schematic process flow of the entire fabrication steps is shown in Figure 3.6.

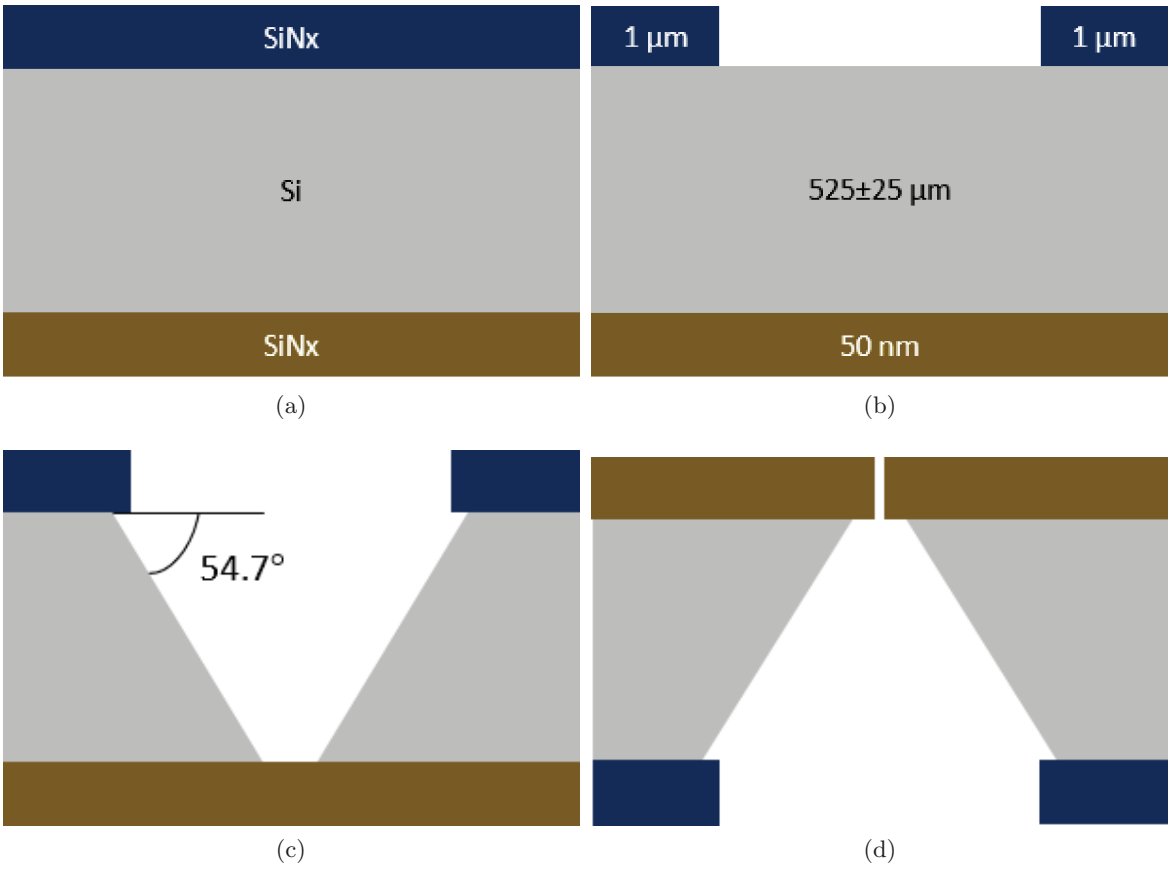

Figure 3.6: Schematic process flow of nanopore fabrication(a) SiN_x deposition using PECVD, (b) Patterning the back side SiN_x by photo-lithography, (c) Anisotropic etch of silicon, with the SiN_x acting as mask, (d) nanopore fabrication on free standing SiN_x using TEM.

3.2 Experimental Setup

The chip with nanopore acts as a path for the ionic solution (KCl here) to flow through, when sandwiched between two electrolytic reservoirs. When the reservoirs are sealed properly onto the nanopore, the pore acts as the only conduction path for the fluid in either chamber, as shown in Figure 3.7. When a potential difference is applied across the chip, the ions and the fluid are set in motion through the pore. This ionic motion produces a current. The ionic current through the nanopore can be used to characterize the nanopore. Also, when charged molecules pass through the pore, this molecule causes a shift in the measured current, which is unique for a specific molecule. Such measurements are highly sensitive and in order to extract the necessary information, a well-shielded low noise setup was designed.

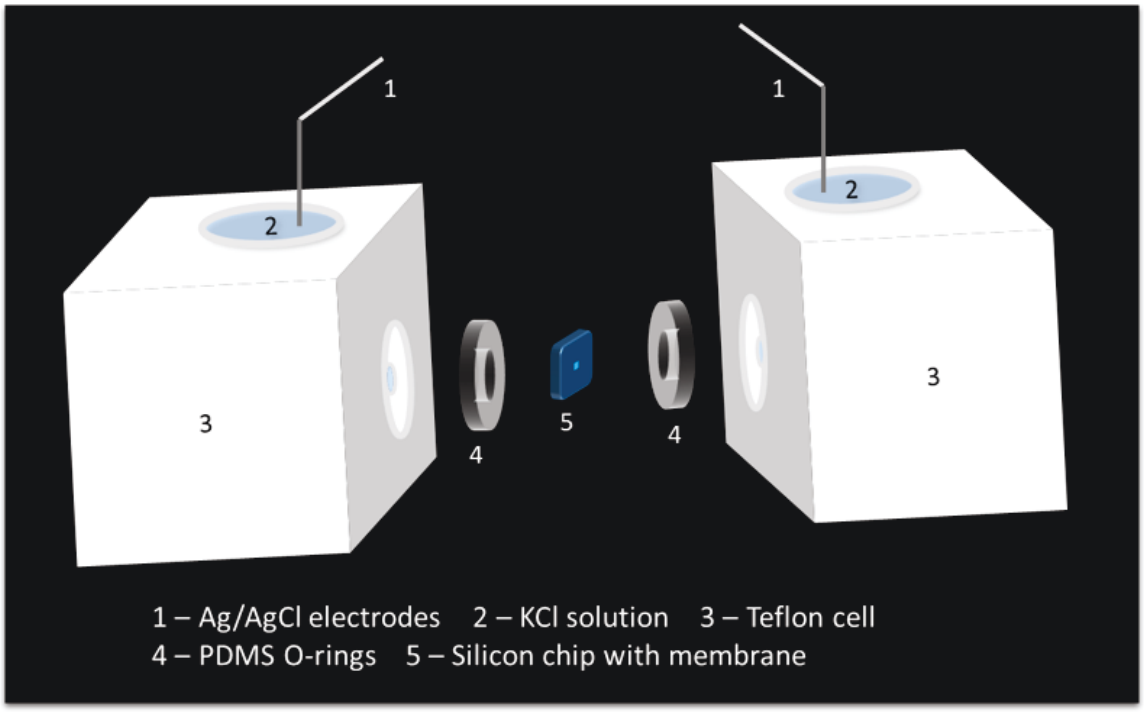

Figure 3.7: Exploded view of the measurement cell assembly. The chip with nanopore is sandwiched between PDMS gaskets, which are in turn fit into the half cells.

3.2.1 Materials used

Measurement Cell: The cell used for the measurement was made out of Polytetrafluoroethylene (PTFE), commonly known as teflon. PTFE was chosen to be the cell material, owing to its chemical resistance and inertness. The hydrophobic nature of teflon surface aids

in thorough cleaning between experiments. Electrical insulation of teflon, prevents some amount of electrical interference during measurements. The teflon cell was custom made in the machine shop.

Sealing Gaskets: In order to tightly seal the fluid flowing through the nanopore to/from the teflon cell, Polydimethylsiloxane (PDMS) gaskets were used. PDMS gaskets were found to be more effective in making a good seal as compared to silicone elastomers, thereby reducing the capacitance noise during conductance measurements [45]. Gasket making was a two-step fabrication process.
First step involved PDMS film formation

1. A clean polished 4 silicon wafer was silanized overnight, to make it's surface anti-adhesive.

2. SYLGARD® 184 SILICONE ELASTOMER Base and Hardener from Dow Corning was mixed at the ratio of 10:1 by volume, and later degassed to remove air bubbles.

3. The degassed mixture was poured onto the silanized wafer setup. Prior to pouring the mixture, an elastomer gasket with a weight on top was placed on the wafer to act as the mould for PDMS).

4. The setup was then cured in an inert atmosphere at 85^o C for 2 hours, the setup was slightly tilted to the horizontal plane to achieve a varying film thickness of 1.5 mm to 1.7 mm (to obtain a thickness that is similar to the slot width of 1.57 mm on the teflon half cell).

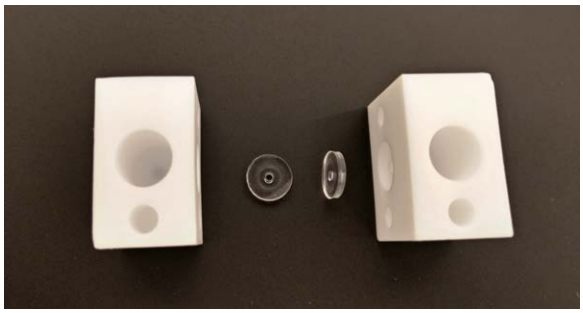

Figure 3.8: Teflon half cells and fabricated PDMS gaskets used in the experiments

For the second and final step, brass punches were used to punch out concentric PDMS gaskets out of the film, with outer diameter of 10 mm and inner diameter of 1 - 2 mm. Figure 3.8 shows an image of the cell and gaskets used for enclosing the nanopore chip.

Electrodes: Ag/AgCl electrodes were used to apply potential biases in the electrolytic reservoirs. Teflon coated, 0.25 mm thick silver wire was soldered onto gold plated 1 mm pin. The teflon encapsulation was partially removed, to coat chloride onto the bare silver. Exposed parts of the silver wires were then wiped with ethanol, Deionized (DI) water, and immersed in bleach for an hour to obtain a thick coating of chloride.

Shield: A Faraday Cage with vibration isolation was purchased from Warner instruments, the aluminum cage greatly reduced electrical interference from atmosphere. The stage of the cage was air pumped to dampen mechanical and physical vibrations. The cage contained solid brass grounding blocks to reduce electrical discharge and interference. An image of the Faraday cage can be seen in Figure 3.9

Electrical system setup: Axopatch 200B patch clamp amplifier was used to measure low noise current levels ranging from 10^{-12} to 10^{-9} amperes. The amplifier head holds sockets to insert Ag/AgCl biasing and reference (ground) electrodes, which in turn was immersed into the electrolytic reservoirs, these electrodes were used to apply a potential across the nanopore. The nanopore current measured as voltage by the headstage is initially pre-amplified, which was then filtered by a 8 pole low-pass Bessel filter from Warner Instruments and finally amplified, digitized by analog to digital, 16 Bit Data acquisition (DAQ) system : DIGIDATA 1322A from Axon Instruments. The digitized current signal was observed and recorded real time using Clampex 10.6. The DAQ system was also used to feed in externally sourced biasing from the oscilloscope. A schematic of the setup is shown in Figure 3.9.

3.2.2 Cleaning and Mounting

Prior to experimental characterization of the fabricated nanopores, the nanopore and setup involved needed to be cleaned throughly to avoid noise or pore blockage during experimentation. The chips, gaskets, teflon cell, electrodes and buffer solution used in the experiments were systematically cleaned and mounted before every experiment.

1. Piranha cleaning of pore is an essential step for removal of organics and cleaning of the pore post fabrication. Following steps explain this cleaning process.

   (a) Fabricated pores were cleaned in piranha solution, the chips were carefully removed out of their containers using tweezers and placed in a 40 mL beaker, with

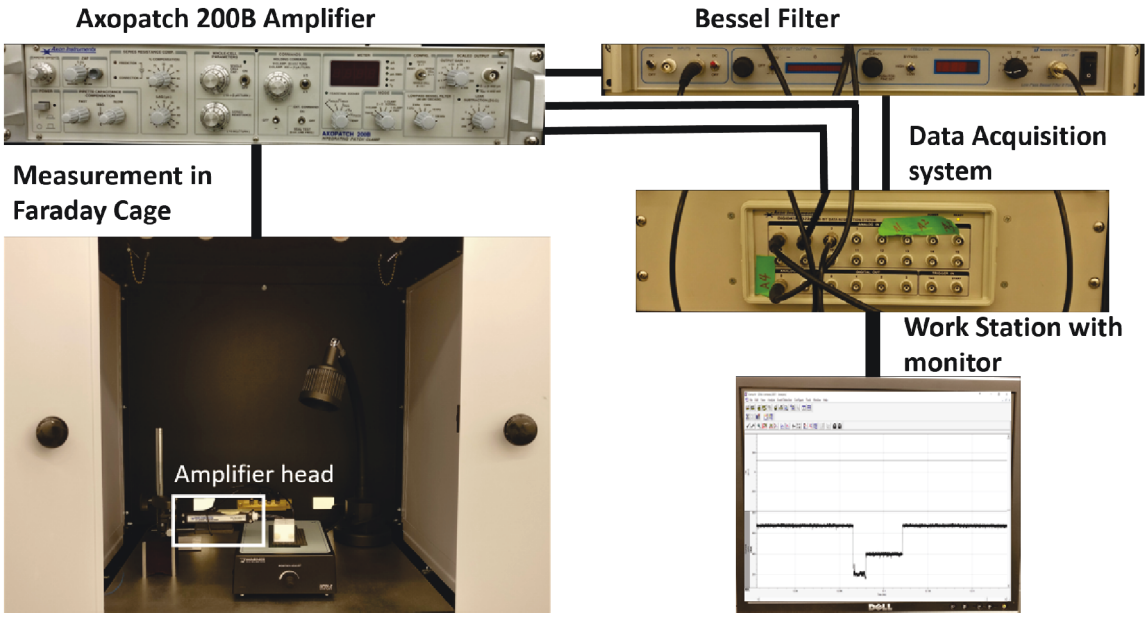

Figure 3.9: Schematic of the electrical system used for nanopore characterization.

the membrane side on top.

(b) 15 mL of 96% H_2SO_4, was added onto the beaker using a clean glass pipette. The chip was carefully pushed back into the liquid, if it floated, to ensure complete immersion of chip.

(c) 5 mL of 30% H_2O_2 was then added on top of H_2SO_4 (3 H_2SO_4 : 1 H_2O_2 ratio), refluxing was done to ensure proper mixing. Piranha involves a highly exothermic reaction, hence extreme caution was employed during solution preparation, with proper acid gear worn throughout the process.

(d) The solution was heated on a hotplate at 95^o C for a period of 2 - 3 hours, small amounts (1 to 2 mL) of excess H_2O_2 was added occasionally to keep the piranha reaction active through the heating process.

2. KCl buffer solution preparation : 1M filtered KCl solution buffered at pH 8 with 10mM Tris-HCl was prepared and stored. The stored KCl solution was degassed in a vacuum for $\sim$ 90 minutes at 40^o C, to remove air bubbles. The degassed solution was then allowed to cool to room temperature, before it was used for measurements.

3. Filtered DI water was degassed under similar temperature and pressure conditions for 90 minutes, to completely remove air bubbles, which might block the pore. The air bubbles get trapped on the pore and demonstrate very poor conductance. The

degassed water was later used for cleaning the chips.

4. The teflon cell and PDMS gaskets were sonicated in acetone and IPA, for 10 minutes each. Cleanroom swabs were used to further manually clean intricate parts of the cell. When biological specimens were employed in the experiments, additional decontamination of the cell was performed by cleaning them in boiling 20% nitric acid (HNO_3) for 30 minutes, followed by water boiling to remove the HNO_3.

5. The cell and gaskets were dried and placed in a clean zone for chip mounting.

6. Ag/AgCl electrodes were used for the measurements. Chloridized electrodes were cleaned by scrapping with sand paper, to remove the chloride and then cleaned with dilute HNO_3 for decontamination. The electrode tips were then wiped with dilute HCl, followed by ethanol and DI water wipe. Cleaned electrodes were immersed in bleach for an hour to re-chloridize the electrodes.

7. Post Piranha cleaning, the beaker with chip was moved from the hotplate and let to cool down to room temperature, before it could be cleaned with DI water from step 3. It was observed that when the chip was directly quenched into DI water, thermal stresses were imparted onto the membrane, causing the membrane and pore to stretch and thus the pore current remained unstable. Optical microscope images of bent membrane are shown in Figure 3.10.

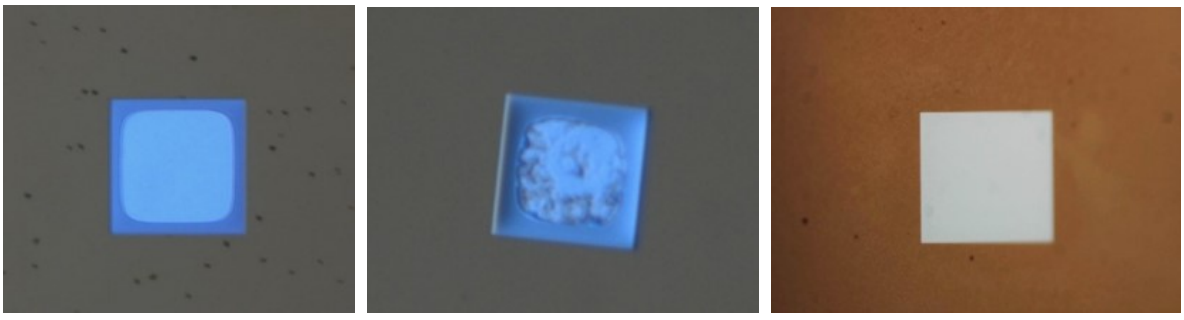

(a) (b) (c)

Figure 3.10: Effect of thermal stress on SiN_x membrane. (a) Membrane bent due to thermal stress, water segregation around the edges indicates membrane bend, (b) Bent membrane retaining left over ethanol, (c) Clean and unbent membrane, after letting the chip in piranha solution to reach room temperature before cleaning it with water.

8. The chip was then carefully pulled out of piranha solution and placed in a beaker filled with 15 mL of degassed DI water from step 6. DI water was removed from the

beaker and fresh 15 mL of DI water was flushed into the beaker using a clean pipette. The process was repeated 5 times to completely remove piranha.

9. Finally, 15 mL of ethanol was added onto the beaker, to quickly dry the chip with mild air blow.

10. The dried chip was loaded, as soon as possible after cleaning, between the PDMS gaskets, with alignment of the free standing membrane along the gasket opening done under an optical microscope. *Cis* and *trans* chambers were marked on the cell. The screws of the cell were tightened, to make sure the gaskets formed a tight seal (this ensured reducing any leak, also avoiding any stray capacitance which could add to the high frequency noise during nanopore conductance measurements [45]). Figure 3.11 shows the setup of chip sandwiched between PDMS gaskets, post alignment under optical microscope.

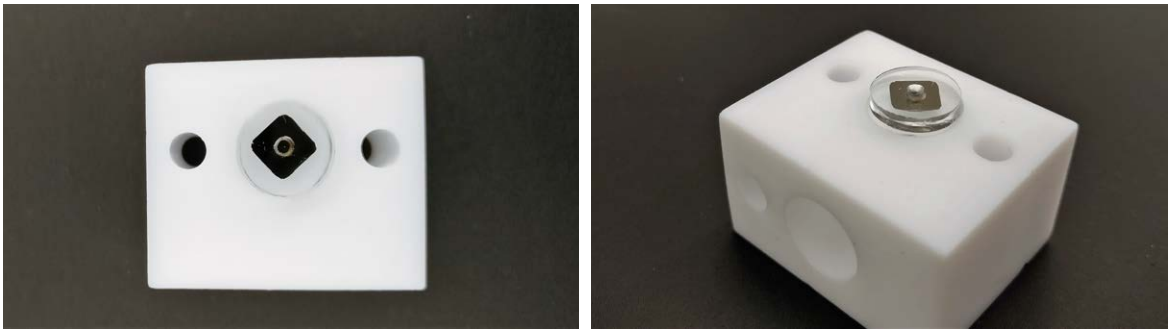

(a) (b)

Figure 3.11: (a,b) show the top and side views of the chip sandwiched between PDMS gaskets (and loaded onto the teflon half cell), post alignment under optical microscope.

11. Ethanol was filled into both the reservoirs of the cell, and the setup was placed in a desiccator under vacuum to wet the pore. The cell was placed in a glass desiccator under vacuum, until air bubbles were seen popping out of the reservoirs. This step was found to be crucial, skipping which greatly reduced the probability of electrolyte flow into the pore.

12. Next, both reservoirs were flushed with 40 mL of 1M KCl in each, flushing the reservoirs alternatively for every 10 mL. This ensured complete removal of ethanol and wetting of pore with KCl.

13. All the above mentioned cleaning and mounting steps were performed in a class 1000

cleanroom, this ensured a high probability (>70%) of measuring the pore conductance (when other steps were carried out properly), by maintaining the pore and the system clean. Extreme caution was employed while handling the chips, as the membranes are very delicate and fragile. Figure 3.12 shows optical microscope images of broken membranes, due to rough or casual handling.

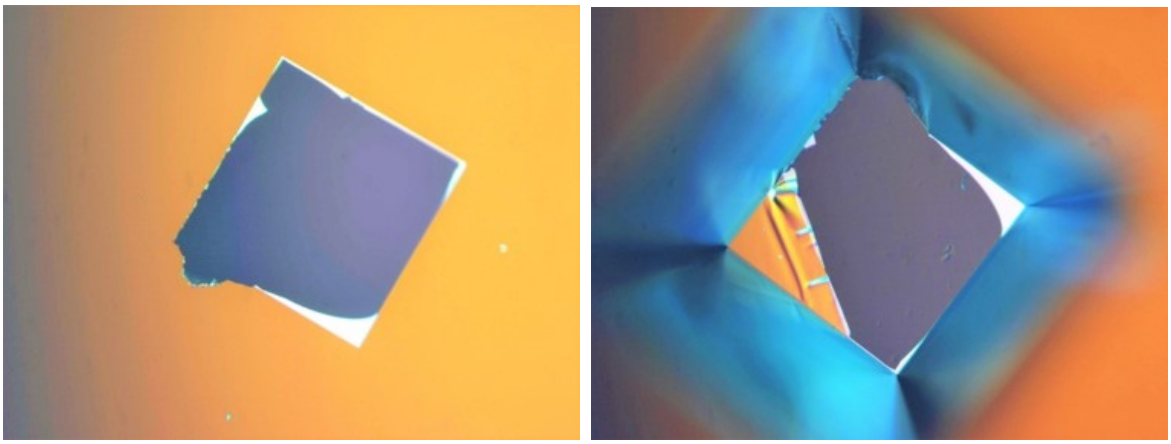

(a) (b)

Figure 3.12: Broken membrane images. (a),(b) are typical images of broken membranes due to rough handling

Following the above steps, the nanopore was ready for characterization, it was moved to the Faraday cage and characterized by placing Ag/AgCl electrodes interfaced with the amplifier head, into the reservoirs. In all experiments performed in this thesis, signals were filtered at 3.5 kHz by the low pass Bessel filter, amplified and sampled by the digitizer at a rate of 20 kHz. Occasionally, the pores were partially clogged, resulting in the measured nanopore current being unstable or less than expected for the size of particular pore. When this happened conditioning techniques were attempted (explained in next chapter). When the pore did not display a stable conductance after several attempts, the chip was removed from the cell, and all the cleaning steps were repeated for the chip, cell, gaskets, electrodes and KCl/DI water degassing was also repeated.

3.3 Numerical Model Setup

For the conductance-based characterization of solid state nanopores, a Finite Element Model (FEM) was setup to numerically solve for the conductance. COMSOL Multiphysics 5.1/5.2 was used to build an electrokinetic models to simulate and extract conductance of the

nanopore. The batteries and Fuel cells module was used for this purpose. A 2D model, with an axis of symmetry was chosen to solve the problem. A workstation with 16 GB RAM, Core i7 processor @ 2.00 GHz was used for most of the computations.

3.3.1 Parameters

The general parameters used in the model are listed in Table 1. 1M or 1000 mol.m^{-3} KCl solution was chosen as the ionic solution, the surface charge of silicon SiN_x immersed in 1M KCl, pH 8.0 at room temperature was used as -0.02 C.m^{-2} [53,54] from the literature.

Table 3.1: Parameters for the COMSOL Model

Name	Expression	Unit	Description
c_0	1000	mol.m^{-3}	bulk concentration of ions
sig	-0.02	C.m^{-2}	surface charge of SiN_x in 1M KCl
vbias	0.5	V	applied biasing potential
DiK	1.957x10^{-9}	m^2.s^{-1}	potassium ion Diffusion coefficient
DiCl	2.032x10^{-9}	m^2.s^{-1}	chloride ion Diffusion coefficient
erel	80		water dielectric constant
evac	8.856x10^{-12}	F.m^{-1}	vacuum dielectric constant
T	298	K	temperature of the fluid
visc	0.001	Pa.s^{-1}	fluid velocity
rou	1000	kg.m^{-3}	fluid density
thickness	50	nm	membrane thickness
angle	20	degree	half cone angle of the hour-glass pore

3.3.2 Geometry

The geometry of pores may affect the conductance. Thus knowing the size and shape of the pore is important in order to be able to model the pore structure for the COMSOL model. Geometry for the characterization of solid state nanopores was modeled from tomography images of the pore. TEM images were analysed using ImageJ to obtain the pore dimensions. From the tomography images as shown in Figure 3.13(b), half cone angle(θ) of the pore was found to be 20^o. Pore thickness(L) was known to be 50 nm (membrane thickness). Outer radius(R) is related to the pore radius(r) by,

$$R = r + \left(\frac{L}{2}\right) tan\theta \tag{3.1}$$

The size of the half cells on either side of the pore (electrolytic reservoirs between which the pore is sandwiched), was optimized to be 5 x 5 μm, considering the computational time and capacity. This area was found to be sufficient to calculate the conductance, as the conductance did not vary considerably with the change in this half cell size (as shown later, in section 4.2.3.3). The right half of the axis symmetrical 2D model is shown in Figure 3.13(c). Boundary 1 is the axis of symmetry, boundaries 2, 3, 8 and 9 are the walls of the cell, 5, 6 are the pore walls and 4, 7 represent the SiN_x membrane in contact with fluid in either reservoir.

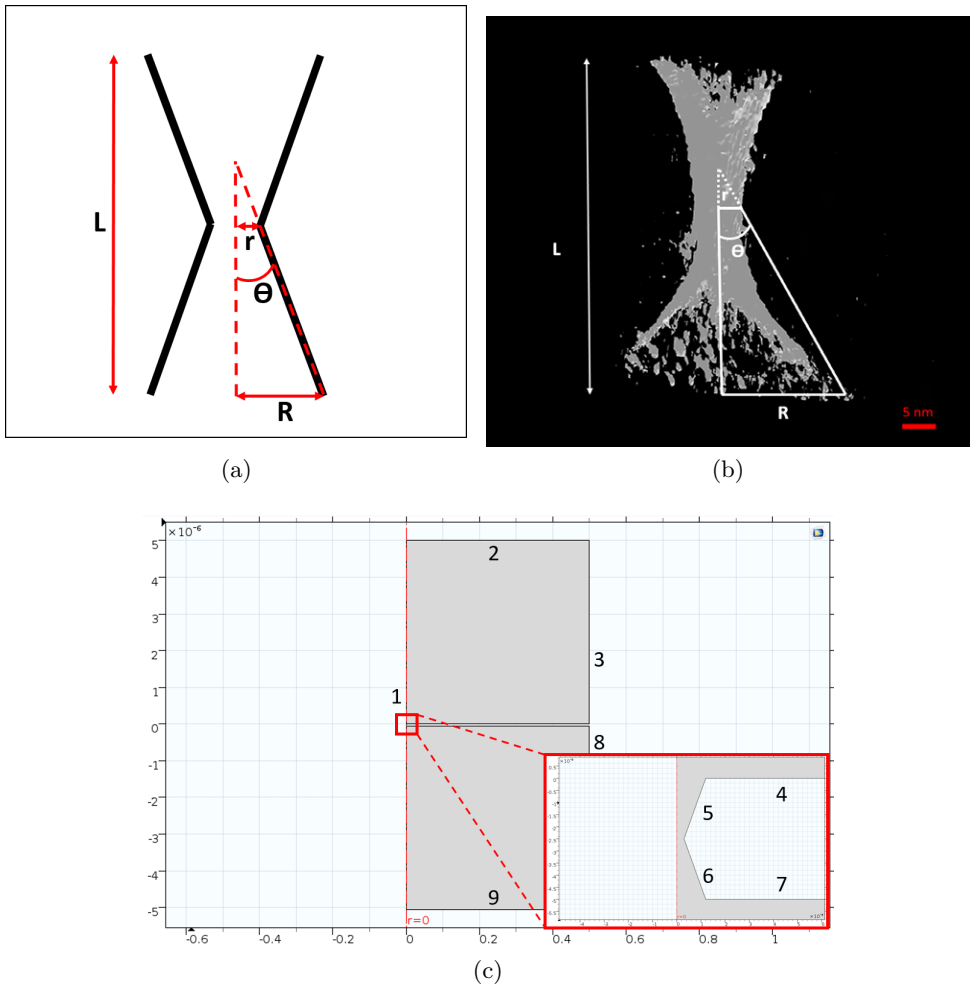

Figure 3.13: Geometry of the hour-glass shaped pore and cell. (a) Pore Geometry modeled by duplicating structure obtained from tomography, (b) Tomography image of a hour-glass shaped pore showing the pore shape, (c) Snapshot showing 2D geometry of the measurement cell around the axis of symmetry (numbered 1), inset shows zoomed in view of the pore. Axis on the image is in units of m.

Other pore geometries were also built to analyze differently shaped pores. Some of

the other geometries include cylindrical pore, conical pore, hour-glass shaped pore with a cylindrical body.

3.3.3 Physics Involved to solve for the behavior of ionic fluid passing through the nanopore

For solving the electrokinetic problem, three types of physics were solved simultaneously as described in chapter 2.

3.3.3.1 Transport of Diluted species(*tds*)

The ions and the fluid in an electrolytic solution move due to different forces like convection, diffusion and migration. This mass transfer of ions creates a mass flux, which could be used to understand the concentration distribution of different ions in the system. This physics solves for the concentration fields created by transport of ions (K^+ and Cl^-) through the surface charged nanopore using flux equations (Nernst-Planck equation) for every ion,

$$N_i = -D_i \nabla c_i - z_i \left(\frac{D_i}{RT} \right) F c_i \nabla V + u c_i \tag{3.2}$$

$$\nabla . N_i = 0 \tag{3.3}$$

Equation 3.2 and 3.3 are Nernst-Planck equation and equation of steady state respectively.Where N_i, D_i, c_i, z_i are respectively, the flux, diffusion constant, concentration and charge of species i. V and u are the local electric potential and fluid velocity, F, R, and T are the Faraday constant, universal gas constant and absolute temperature respectively. Transport of diluted species solves for the concentration terms which is then fed into the electrostatics and laminar flow physics modules.

Boundary conditions and Initial values:

The top and bottom boundaries were setup at bulk concentration(c_0) of K^+ and Cl^- ions. Rest of the geometry was given an initial concentration value of 0. Other boundaries were assigned as no flux boundaries, representing the SiN_x surface or the cell wall. Boundary conditions pertaining to this physics is illustrated on the model geometry in Figure 3.14.

3.3.3.2 Electrostatics(*es*)

The application of an external electric field causes movement of ions relative to charged surface through a nanopore. A potential distribution is created across the nanopore due to

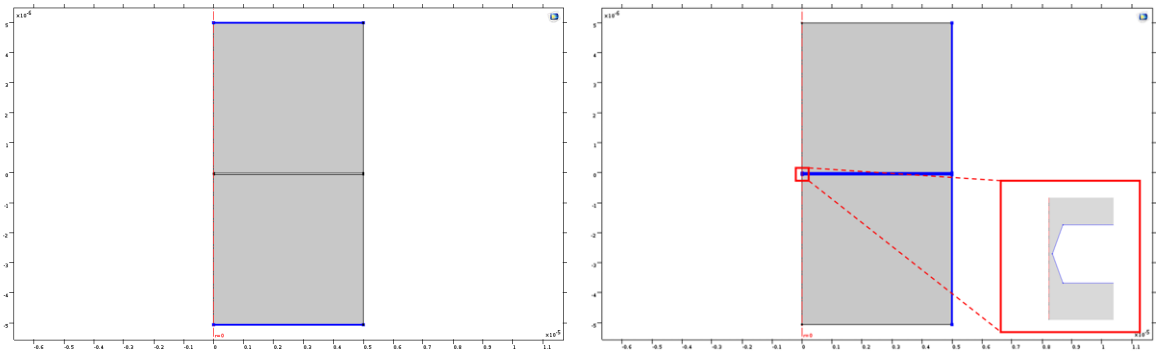

(a) (b)

Figure 3.14: Boundary conditions involved in Transport of diluted species physics. (a) bulk concentration(c_0) of K^+ and Cl^- ions at top,bottom boundaries, (b) no flux boundary condition for the pore surface, membrane and cell walls. Axis on the images is in units of m.

space charge density of different ions. This physics solves for the electric potential, which is dependent on the charge density distribution,

$$\nabla.(\epsilon_0\epsilon_r E) = \rho_v \tag{3.4}$$

$$E = -\nabla V \tag{3.5}$$

$$\rho_v = F\sum_i (z_i c_i) \tag{3.6}$$

$$\epsilon_0\epsilon_r = \epsilon \tag{3.7}$$

$$\nabla^2 V = \frac{-F}{\epsilon}\sum_i (z_i c_i) \tag{3.8}$$

Equation 3.8 is Poisson′s equation, E is the Electric field, ρ_v is the space charge density, ϵ_0, ϵ_r and ϵ are permittivity of vacuum, relative permittivity and dielectric constant of the medium respectively. Electrostatics physics solves for the electric potential distribution, which is then fed into transport of diluted species and laminar flow physics modules.

Boundary conditions and Initial values:

The nanopore walls and membrane were given a surface charge value of -0.02 $C.m^{-2}$. The two electrodes were placed at the two extremes, to make sure there is no interference to the pore electric field. The top boundary was grounded and bias voltage was applied at the bottom boundary. The walls of the cell were given a zero charge and an initial potential value of 0 was assigned to rest of the surface. Boundary conditions at the corresponding boundary is shown in Figure 3.15.

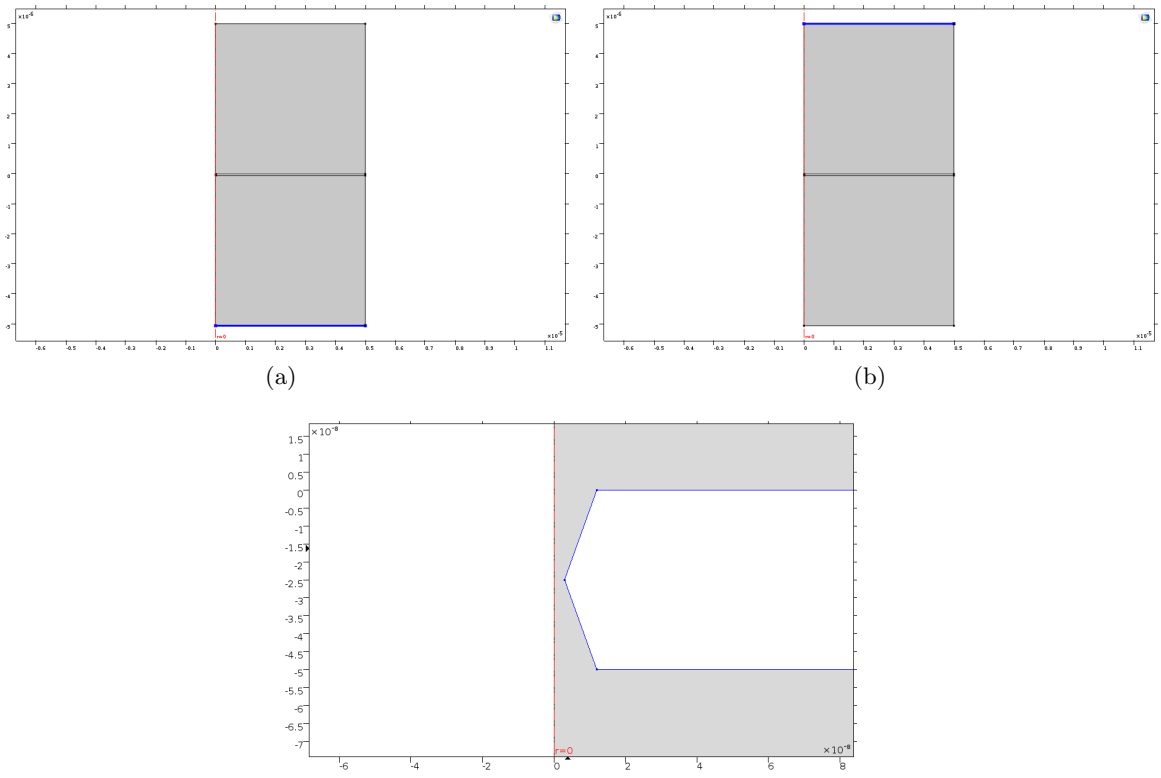

Figure 3.15: Boundary conditions involved in Electrostatics physics.(a) Electric potential applied at bottom boundary, (b) Ground applied at bottom boundary, (c) Surface charge of -0.02 C.m^{-2} applied on nanopore walls and membrane. Axis on the images is in units of m.

3.3.3.3 Laminar flow(*spf*)

The fluid flow of a system under laminar flow with constant viscosity and density is given Navier-Stokes and continuity equations. The flow of fluid in turn affects the concentration and potential distribution. This physics solves for the local position dependent fluid velocity and pressure, with concentration and potential as inputs.

$$u\nabla u = \frac{1}{\rho}(-\nabla P + \mu\nabla^2 u + F_v) \tag{3.9}$$

$$F_v = -F\sum_i (z_i c_i)\nabla V \tag{3.10}$$

$$\nabla . u = 0 \tag{3.11}$$

Equation 3.9, 3.11 are respectively, Navier-Stokes equation and equation of incompressible fluid flow. ρ, μ and P are the fluid density, viscosity and pressure respectively. F_v is the volume force. Laminar flow physics solves for the velocity and pressure distribution of the fluid system, which is then fed into electrostatics and transport of diluted species physics

modules.

Boundary conditions and Initial values:

Null pressure was assigned to the top and bottom surfaces to make sure, there is no

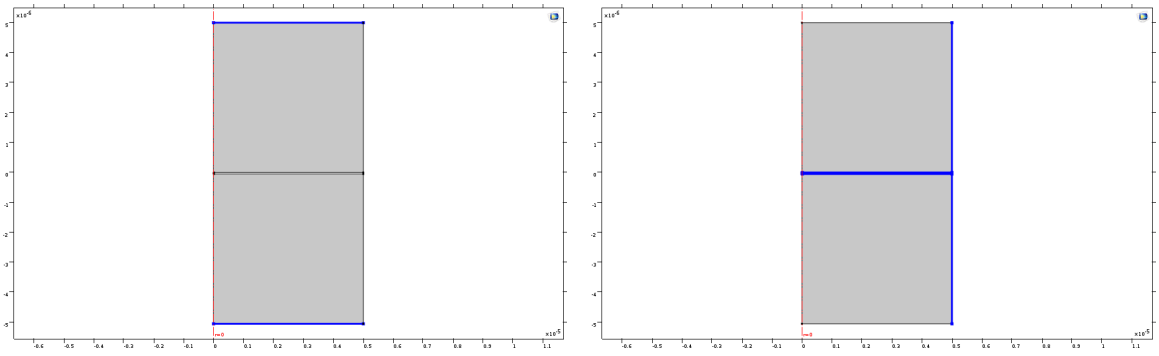

(a) (b)

Figure 3.16: Boundary conditions involved in Laminar flow physics.(a) null pressure assigned to top and bottom boundaries, (b) no slip boundary condition for the pore surface, membrane and cell walls. Axis on the images is in units of m.

other external force driving the ions and the fluid, other than the electric potential. The nanopore, cell walls and membrane were assigned no slip boundary conditions, ensuring no inflow/outflow. Initial fluid velocity and pressure were given a value of 0 for the rest of the surface. Figure 3.16 shows the different boundary conditions involved in this physics.

Each physics module assumes an initial value for all variables, and is solved simultaneously (in an iterative loop) until a concurrent solution is reached.

3.3.4 Meshing

For the physics modules from the preceding section to be solved across the geometry, a close knit mesh structure is necessary. This section describes the build up of the mesh structure for the problem under consideration.

SiN_x surface develops a surface charge when immersed in an electrolytic solution. In the present model -0.02 C.m^{-2} is used as the charge. This surface charge attracts counter ions, which in turn attracts other ions. This process generates a distribution of ions within a thin layer near the SiN_x surface, called the Electric Double Layer (EDL). The thickness of this layer is called Debye length (λ), for a symmetric electrolyte λ is given by,

$$\lambda = \sqrt{\frac{\epsilon RT}{2z^2F^2c_0}} \tag{3.12}$$

where, z is valence modulus of a symmetric electrolyte. Equation 3.12 reduces to Equation 3.13 as,

$$\lambda = \frac{3.04}{z\sqrt{M}} * 10^{-10}m \tag{3.13}$$

The Debye length is $\sim$ 3 Å for 1M KCl solution obtained by solving Equation 3.13. To resolve this double layer, a mesh size less than 1 Å was defined near the SiN_x surface. High resolution mesh was defined at intricate regions like the pore to obtain good results. A progressively growing mesh was defined for the rest of the region with a maximum element size of 0.1 μm. A typical mesh structure of a 5 nm pore is shown in Figure 3.17, the maximum mesh size at the membrane and pore surface was set at 1 Å.

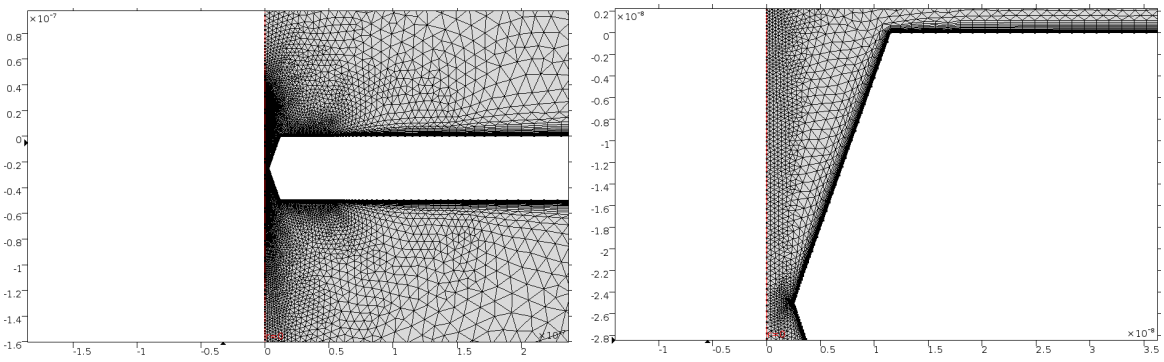

(a) (b)

Figure 3.17: Mesh structure. (a) Progressively growing mesh, (b) Highly resolved mesh at the SiN_x surface and pore region. Axis on the images is in units of m.

Upon defining all the physics, initial values, boundary conditions and upon building the mesh, the model was used to solve for all the physics simultaneously, to obtain a convergent solution.

3.3.5 Running the simulation and deducing conductance

The model was run in stationary study mode for most of the computations. Parametric sweep feature was used to observe the change in conductance by varying parameters like

applied bias, bulk concentration, surface charge, electrode length and distance, to name a few, for analyzing effect of different parameters on conductance.

3.3.5.1 Calculating Conductance from the model

The ionic current through the nanopore, is calculated by surface integration of current density over a cross sectional cut plane at the pore.

$$I = \int_S F(z_{K^+}N_{K^+} + z_{Cl^-}N_{Cl^-}).ndS \tag{3.14}$$

where I is the pore current, z_{K^+}, z_{Cl^-} are the charge of K^+ and Cl^- ions respectively, while N_{K^+}, N_{Cl^-} are the flux of K^+ and Cl^- ions. S is the surface across which the integration is performed. Figure 3.18 shows the the sliced 3D image of the cut plane.

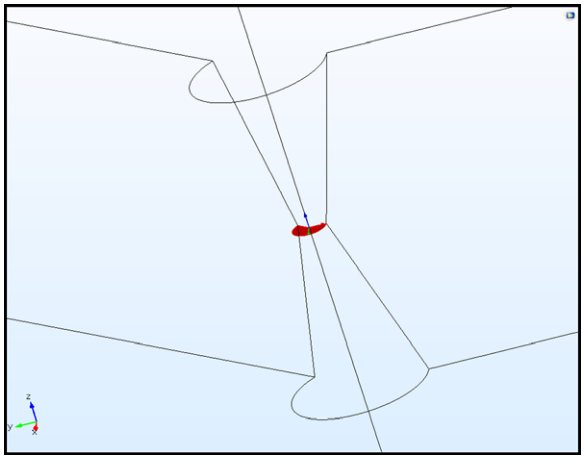

Figure 3.18: Cut plane (red in color) built at the pore to measure current.

The pore conductance(G) is then obtained from,

$$G = \frac{I}{V} \tag{3.15}$$

Upon completion of the experimental setup, nanopore cleaning and mounting. The nanopore was ready for experimental characterization. The numerical model built as described in the preceding section was used to run electrokinetic simulations to measure the conductance of different pores using simulations.

Chapter 4

Results and Discussion

This chapter presents the results of nanopore characterization by comparing the experimental and simulated conductance. Further characterization of solid state nanopore is conducted using the simulation technique, by varying several parameters like pore dimensions, structure, surface charge of the membrane, electrode position variation, etc., to observe the corresponding effect on conductance. Nanopore sensing based preliminary measurements of different biological molecules like DNA, polysaccharide and proteins are presented later in the chapter.

4.1 Conductance-based characterization of nanopores

Conductance of the nanopore is a direct measure of the amount of ions transporting through a pore of specific size. Measuring the conductance of a nanopore (known shape and thickness) aids in predicting the size of a pore, which is very useful in characterizing the nanopore. This is also important for molecular sensing and nanopore hybridization since the size of the nanopore affects the observed current during molecular events. Understanding the conductance of a nanopore is the foundation for any nanopore experiment. For the conductance-based characterization of solid state nanopores, experimental current of the nanopore was measured using a powerful amplifier. Pore conductance was then deduced from current versus potential plots. Experimentally obtained conductance was then compared with the conductance derived by simulating the experimental conditions. The pore size for simulation was obtained from TEM pore images. The nanopore was also initially tested for noise levels, which is explained in the following section.

4.1.1 Noise characterization

Nanopore noise characterization was performed by analyzing the Power Spectral Density (PSD) function plots. Current recordings were obtained at applied biases of 0 and 200 mV over a period of 10 s for 1 M KCl at pH 8.0, the corresponding PSD plots were plotted using Clampfit. Figure 4.1 shows the PSD plots for a pore (5 nm in size) at 0 and 200 mV under partially clogged (or partially wet) and clean (or fully wet) states.

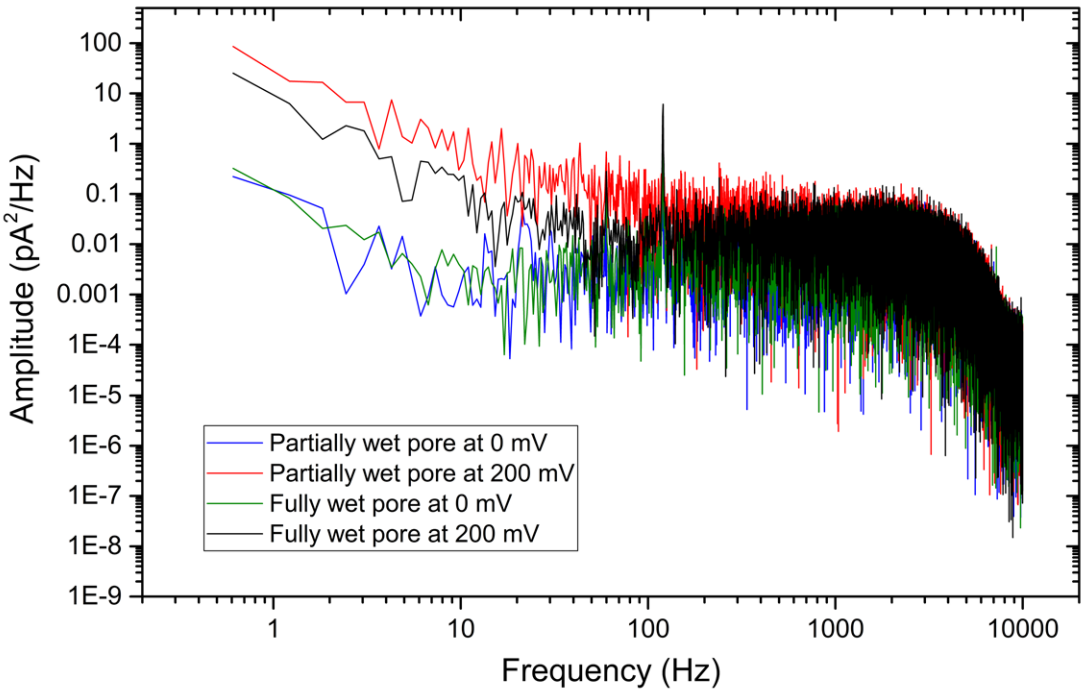

Figure 4.1: Power spectral density analysis of a 5 nm pore under partially wet and fully wet states. The plot shows the PSD measured at 0 and 200 mV applied biases.

It can be seen that the PSD noise at higher frequencies are quite similar at either potential for the two states of the pore (partially wet and fully wet) discussed here. This noise is attributed to the dielectric property of the SiN_x membrane. The low frequency flicker noise also known as $1/f$ noise observed at lower frequencies was reduced by piranha cleaning [45]. Piranha cleaning rendered the pore free from organics, making it more wettable. The noise level in a nanopore is generally characterized by determining the I_{rms} value [45]. I_{rms} was calculated for both the pore states by integrating the PSD plots at 200 mV, and

subsequently obtaining the root of the integrated values.

$$I_{rms} = \sqrt{Area\ under\ the\ PSD\ plot} \tag{4.1}$$

The I_{rms} for the partially wet and fully wet states were found to be 14.44 pA RMS and 10.398 pA RMS respectively, in a 10 kHz bandwidth. In general any pore with a I_{rms} value above 15 pA RMS is considered unfit for nanopore-based sensing experiments [15], since the noise levels are too high at that point and it becomes difficult to resolve the molecular events from base line current levels.

4.1.2 Experimental Conductance

Cleaned and mounted nanopores were tested for conductance with the electrical setup described in section 3.2.1. Figure 4.2 shows the experimental setup of a typical nanopore conductance measurement. For conductance measurements, potential sweeps were applied. Normally a potential sweep of -200 mV to 200 mV at a step of 20 mV, was used for the measurement, with each sweep lasting for 10 s (the sweeps functions were programmed using the waveform generator feature on Clampex 10.6 software, to trigger the applied potential). This potential range was chosen since higher potentials impart a stronger electric field at the pore region, which might affect the pore size [55]. Also, SiN_x nanopores display ohmic behavior in this potential range. The recorded current (1 M KCl at pH 8.0) was then plotted against the corresponding applied bias. The slope of this plot gives conductance of the nanopore. Most of the pores were also tested repeatedly to observe the consistency in conductance. The results from conductance measurements of three different pores are shown in Figure 4.3.

Figures 4.3(a,c,e) show the sweep recordings made for three different hour-glass shaped pores 4.1 nm, 6 nm and 7.4 nm in size, respectively. In each of these figures, the lower half of the image shows the applied potential sweep ranging from -200 mV to 200 mV with a step of 20 mV (each sweep indicated by a different color). The corresponding recorded nanopore current is shown on the top half of the figures under discussion. It can be noticed that the current sweeps are equidistant from each other, similar to the potential sweeps, indicating a linear trend in measured current. The linearity was further confirmed by plotting measured current (nA) against applied potential (V), the slope of this plot then gave the conductance of the corresponding pore. Figures 4.3(b,d,f) show the current vs voltage plots of 4.1 nm, 6 nm and 7.4 nm pore with conductance of 9.34 nS, 20.14 nS and 27.34 nS respectively. The pore conductance was observed to increase with the pore size, this is because of the

decrease in resistance offered by the increasing pore size for the fluid flowing through it. A linear conductance portrayed by each pore, as seen in the figures, is an indication of a clean and symmetrically shaped pore. Insets on the Figures 4.3(b,d,f) show the TEM image of the corresponding pore.

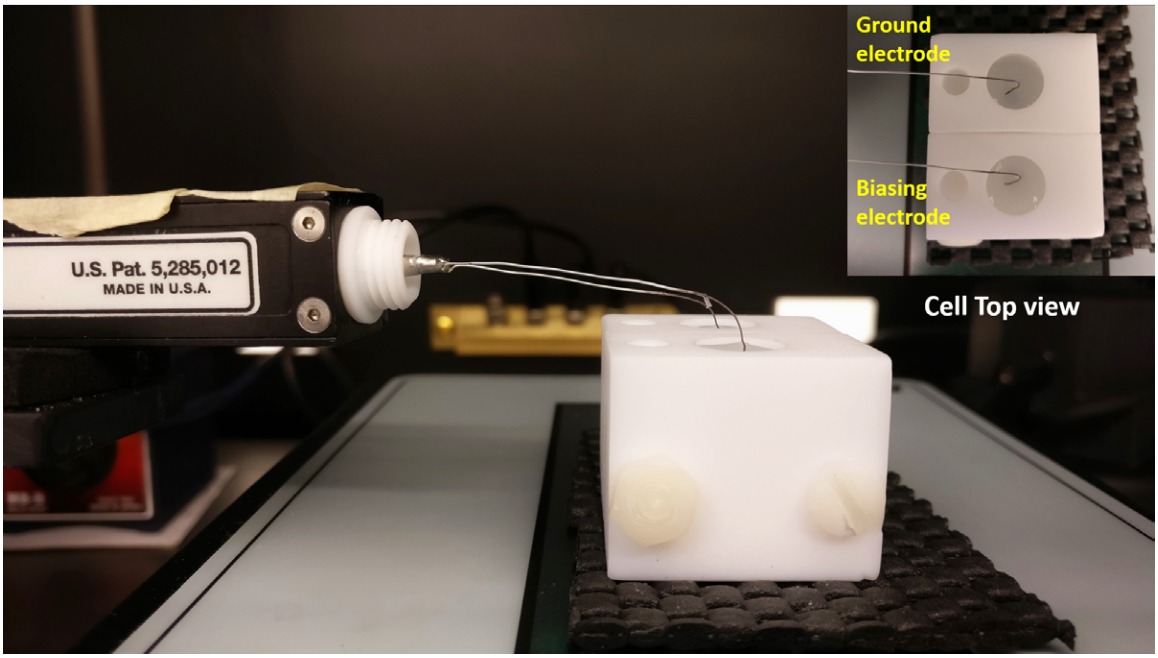

Figure 4.2: Cleaned and mounted nanopore being tested by applying a potential bias with Ag/AgCl electrodes interfaced to the amplifier head. Inset shows top view of the cell.

4.1.3 Experimental and Simulated Conductance Comparison

Experimentally measured pore conductance was matched with the simulated conductance, by plotting measured current against the corresponding applied bias. This conductance was then matched with the simulated (COMSOL) conductance. For this purpose, several hour-glass shaped pores varying in size (4.1 nm, 4.5 nm, 4.7 nm, 5 nm, 6 nm, 7.4 nm) were fabricated, cleaned and measured for pore conductance in 1 M KCl solution. For the electrokinetic simulations, pore size and other experimental conditions such as ionic solution concentration (1 M KCl), SiN_x membrane surface charge (-0.02 C.m^{-2}), fluid viscosity (10^{-3} Pa.s^{-1}), fluid density (10^{3} kg.m^{-3}), diffusion coefficient of the ions (K^+ : 1.957 x 10^{-9} m^2.s^{-1}, Cl^- : 2.032 x 10^{-9} m^2.s^{-1}), fluid temperature (298 K), half cone angle of the hour-glass shaped pore (20°) and pore thickness (50 nm), were used as inputs for the COMSOL model in order to obtain the pore current as described in section 3.3. The simulated pore current was then plotted against the applied potential to obtain the slope

and thus the conductance of nanopore.

Figures 4.4(a,b,c,d,e,f) show the characterization of several nanopores varying in size from 4.1 nm to 7.4 nm by comparing the conductance obtained from experiments and simulations. Black circular dots on these plots indicate the measured experimental current for the corresponding applied potential (potential sweep from -200 mV to 200 mV). The conductance of the different pores sized 4.1 nm, 4.5 nm, 4.7 nm, 5 nm, 6 nm and 7.4 nm were respectively measured to be 9.34 nS, 12.63 nS, 11.6 nS, 20.21 nS, 20.14 nS and 27.34 nS (as shown in Table 4.1). Slope of these plots were measured to obtain the conductance in each case. Red circular dots on these figures indicates the simulated nanopore current for the corresponding applied potential (a parametric sweep was performed to vary the applied potential for each pore). It can be seen that the simulated and experimental current vary linearly with the applied potential for all the pores, owing to the symmetric pore structure. By again measuring the slope, simulated conductance of the different pores sized 4.1 nm, 4.5 nm, 4.7 nm, 5 nm, 6 nm and 7.4 nm were respectively measured to be 12.03 nS, 13.32 nS, 14.02 nS, 15.04 nS, 18.54 nS and 23.71 nS (as shown in Table 4.1).

Table 4.1: Experimental and Simulated conductance comparison

Pore size	Experimental conductance	Simulated conductance	Error percentage
4.1 nm	9.34 nS	12.03 nS	22.34%
4.5 nm	12.63 nS	13.32 nS	6.46%
4.7 nm	11.6 nS	14.02 nS	17.15%
5 nm	20.21 nS	15.04 nS	-33.19%
6 nm	20.14 nS	18.54 nS	-8.66%
7.4 nm	27.34 nS	23.71 nS	-14.31%

The variation of experimental conductance from simulated conductance is shown in Table 4.1. Simulated conductance matches the experimental conductance closely within an error range of 5 % to 30 %. The simulated and experimental conductance increase with increasing pore size, although some experimentally measured pores (like the 4.7 nm or 5 nm pore) show deviation from the observed trend. This deviation could be due to multiple reasons like the TEM drilled pore shape and structure being different from the initial predicted model for some pores, pore size change during the course of experiments owing to the harsh chemical treatment its rendered with [56] and/or the electric field applied at the pore altering the size [55] over longer duration experimental runs.

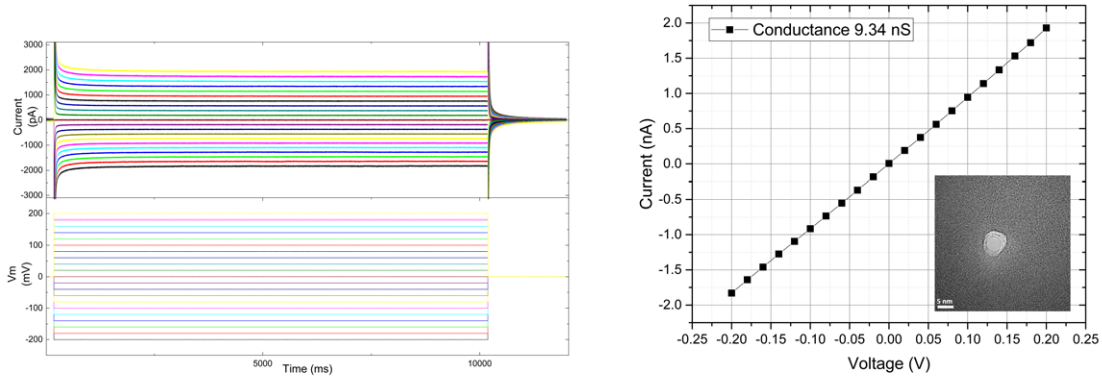

(a) (b)

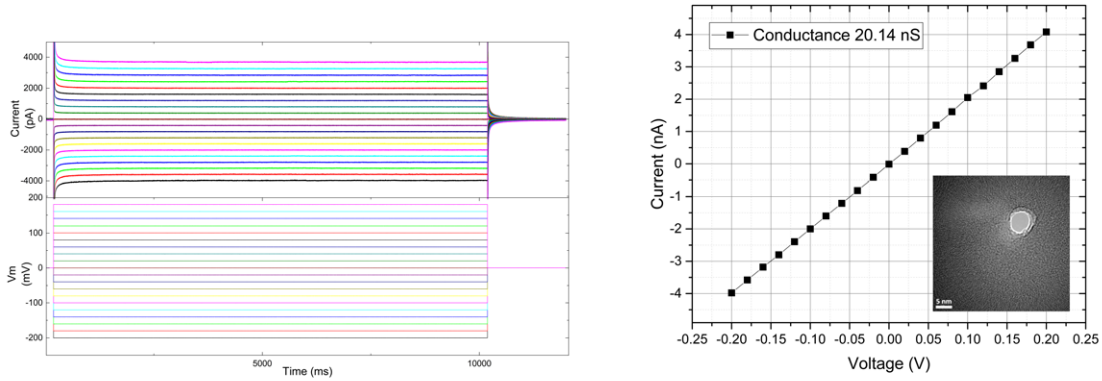

(c) (d)

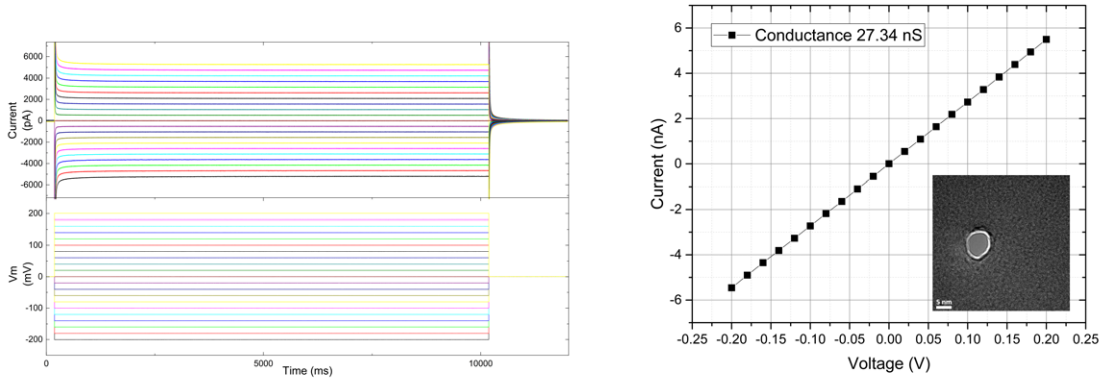

(e) (f)

Figure 4.3: I vs V plotted from potential sweep measurements for different pore sizes. (a) Potential sweep for a 4.1 nm pore and (b) corresponding I vs V plot, (c) Potential sweep for a 6 nm pore and (d) corresponding I vs V plot, (e) Potential sweep for a 7.4 nm pore and (f) corresponding I vs V plot. Potential sweep varied from -200 mV to 200 mV, with a step bias of 20 mV, buffer solution being 1M KCl at pH 8.0. Insets on figures (b),(d),(f) show the TEM image of the corresponding pore.

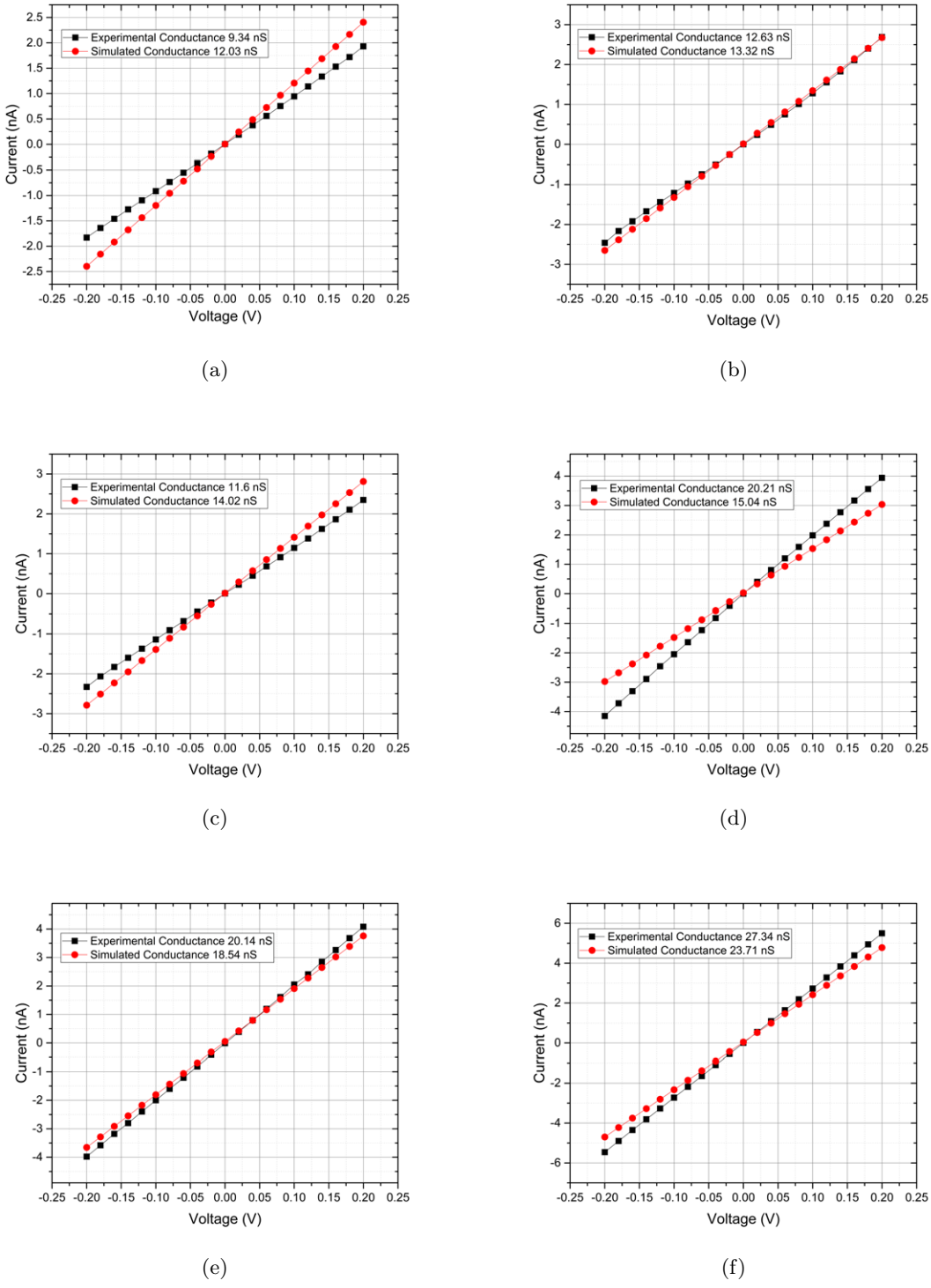

Figure 4.4: Experimental and simulated Conductance comparison for various pore sizes. (a) 4.1 nm pore, (b) 4.5 nm pore, (c) 4.7 nm pore, (d) 5 nm pore, (e) 6 nm pore, (f) 7.4 nm pore. Parametric conditions used in the COMSOL model for conductance determination, 1M KCl, SiN_x surface charge -0.02 C.m^{-2}, fluid viscosity 10^{-3} Pa.s^{-1}, fluid density 10^3 kg.m^{-3}, diffusion coefficient of K^+ : 1.957 x 10^{-9} m^2.s^{-1} and Cl^- : 2.032 x 10^{-9} m^2.s^{-1}, fluid temperature 298 K, half cone angle of the hour-glass shaped pore 20°, pore thickness 50 nm.

4.1.4 Pore Conditioning

Although the experimental conductance is seen to be steady and linear, it was observed that the pore gets blocked occasionally during molecular testing or due to small particles from the ambiance or due to incomplete wetting of the pore. When this happens the conductance became unstable with excessive noise. The following techniques were attempted to solve the problem

- Electrical conditioning was attempted to remove molecule or dirt blocking the pore. Higher potentials (> 400 mV) were applied to electrophoretically pull the molecule stuck at the pore, with a greater force.
- When the above mentioned technique failed to render the pore clean, which happened

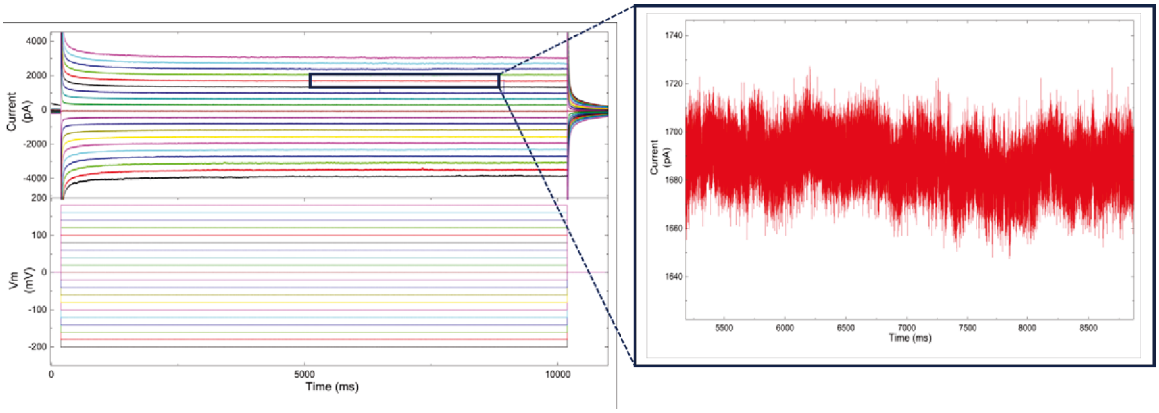

(a)

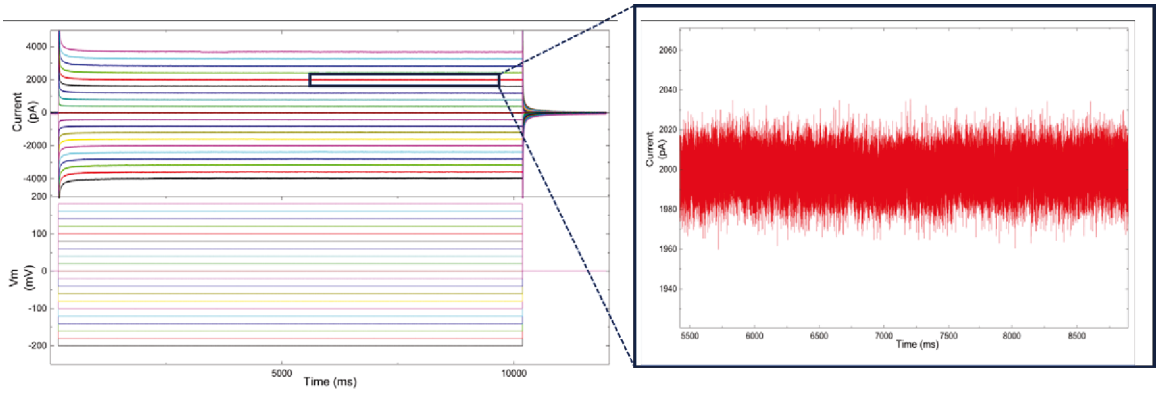

(b)

Figure 4.5: Pore conditioning for a 6 nm pore. (a) Clogged pore with reduced conductance $\sim$ 17 nS, zoomed image shows the unstable and reduced current level of a clogged pore at 100 mV applied bias(b) Cleaner pore with a conductance $\sim$ 20 nS post piranha cleaning, zoomed image shows the stable and improved current level of a cleaned pore at 100 mV applied bias.

to be the case most of the time, the chip was removed from the setup and cleaned in piranha. The entire setup, the cell, gaskets, electrodes and the chip were cleaned as described in section 3.2.2. Figure 4.5 shows how piranha cleaning helps in removing the blockage in a 6 nm pore. Figure 4.5(a) shows the recorded current of a blocked 6 nm pore for a potential sweep from -200 mV to 200 mV. The zoomed in inset on the right shows the unstable and reduced current level at an applied bias of 100 mV. It was observed that the conductance of this pore improved from $\sim$ 17 nS to $\sim$ 20 nS. The current remained stable with lesser noise post piranha treatment as shown in Figure 4.5(b). The pores were cleaned with piranha after each experiment to make sure the pore is clear off any clog or obstacle. The harsh chemical treatment and prolonged electrical measurements affected the actual pore size, resulting in a rise of measured conductance.

4.1.5 Conductance fit

A conductance fit for the experimental data, proved useful in predicting the conductance expected of a particular pore size. This section discusses about the simulated conductance fit and compares it with the experimental and analytical conductance fit (obtained from literature [7]).

Figure 4.7 is a comparison plot of experimental conductance with simulated and analytical conductance model. The simulated conductance fit was obtained by running simulations in COMSOL for various hour-glass shaped pores (half cone angle of 20°) ranging in size from 2 nm to 12 nm were (curve in red). The analytical conductance fit model was adopted from the work by Kowalczyk, *et al* [7]. In this work Kowalczyk, *et al* deduced a numerical relation for the resistance R_{hyp} of a hyperbolic pore (hour-glass shaped pore), given by

$$R_{hyp} = \frac{2\rho}{\pi d}.\frac{\sin\alpha}{1-\cos\alpha}\ \tan^{-1}\left(\frac{\sqrt{D^2-d^2}}{d}\right) \tag{4.2}$$

where ρ is the bulk resistivity of the solution, and is the inverse of the solution bulk conductivity (10.5 S.m^{-1} at room temperature), d the pore diameter, D the larger outer opening of the hour-glass shaped pore and α the asymptotic opening angle of the pore (refer to Figure 4.6), given by

$$\sin^2\alpha = \frac{D^2-d^2}{l^2+D^2-d^2} \tag{4.3}$$

In order to account for the access resistance (resistance along the pore openings) Kowalczyk *et al* used the relation $\rho/\pi D$ given by Hall [57] to calculate the upper and lower limits for total resistance R,

$$R_{hyp} + \frac{2\rho}{\pi D} < R < R_{hyp} + \frac{\rho}{D} \tag{4.4}$$

The access resistance was given as an average value of $2.57\rho/\pi D$, for the calculation of analytical conductance in this thesis. Pore size d, larger pore opening D (obtained from Equation 3.1), and membrane thickness l (50 nm) were inputed into Equation 4.2 to obtain α for all pore sizes. These variables were then used as input for Equation 4.1 along with the additional access resistance to obtain the total resistance for all pore sizes. The inverse of resistance for each pore was plotted against the pore size as shown in Figure 4.7 to obtain the analytical conductance fit (curve in blue). The error between simulated and analytical conductance remains between $10\% - 20\%$. This deviation of the simulated conductance could be partially attributed to the contribution of access resistance being different in each model and due to the effect of surface charge being ignored in the analytical model. However, the simulated conductance provides a better fit to the experimental data in general, as compared with the analytical conductance. This can be seen from Figure 4.7 and Table 4.2.

Table 4.2: Errors between experimental, simulated and analytical conductance

Pore size	Error between simulated and experimental conductance	Error between analytical and experimental conductance	Error between simulated and analytical conductance
4.1 nm	22.34%	3.07%	19.88%
4.5 nm	6.46%	-16.99%	20.04%
4.7 nm	17.15%	-2.32%	19.03%
5 nm	-33.19%	-64.41%	18.99%
6 nm	-8.66%	-32.16%	17.78%
7.4 nm	-14.31%	-35.20%	15.45%

Experimental conductance data points (red dots) match the conductance fit closely within an error range of $5\% - 30\%$. Most of the nanopores used for the purpose of this thesis, were repeatedly tested (for conductance measurement). The conductance (and size) of different pores varied with repeated measurements (cleaning and mounting performed prior to each measurement), as a consequence of severe chemical, heat treatment and electric field application. Figure 4.8 shows the conductance variation of different pores (4.1 nm, 4.5 nm ,4.7 nm, 5 nm, 6 nm, 7.4 nm) with repeated measurements. This variation in conductance

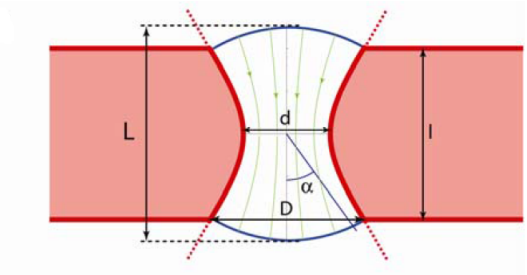

Figure 4.6: Schematic of a hyperbolic pore with the dimensional parameters marked. Image adapted from [7].

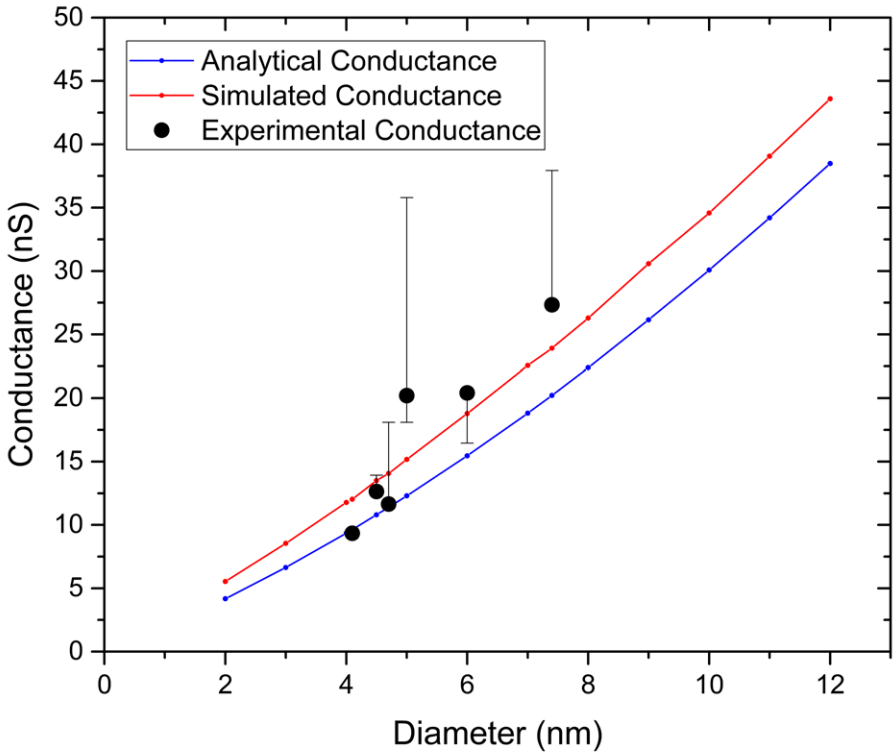

Figure 4.7: Plot showing the simulated and analytical conductance fit for experimental data. Curve in red and blue show the simulated and analytical conductance fit of hour-glass shaped pore (half cone angle 20°) for pore sizes ranging from 2 nm to 12 nm respectively. Black circular dots indicate the experimental data points of nanopore conductance for a few pores.

was observed to follow a nonuniform trend, with the conductance varying differently for each pore beyond a few cleaning and measurement cycles.

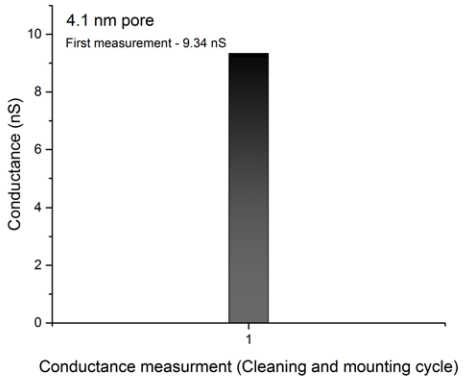

(a)

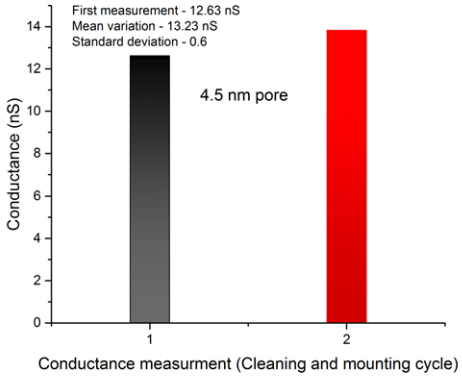

(b)

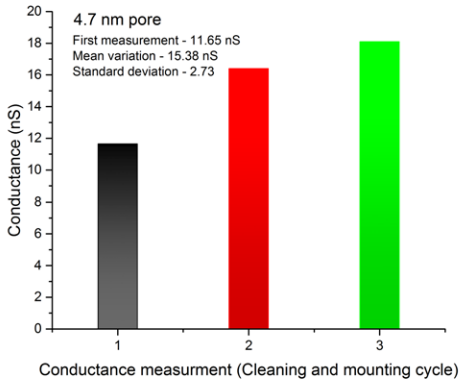

(c)

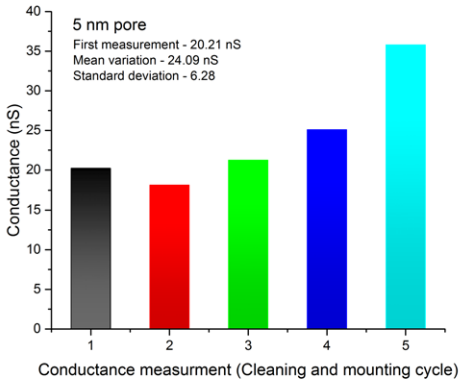

(d)

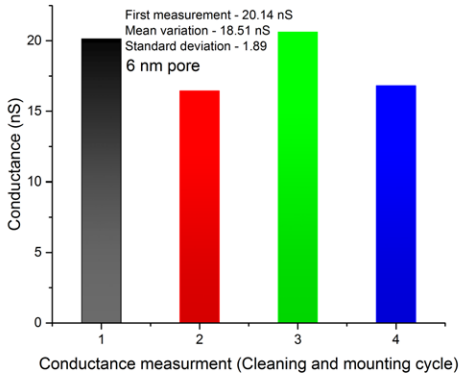

(e)

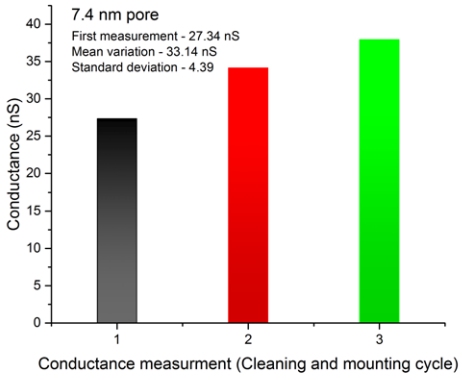

(f)

Figure 4.8: Conductance variation with repeated measurement for different pore sizes (a) 4.1 nm, (b) 4.5 nm, (c) 4.7 nm, (d) 5 nm, (e) 6 nm, (f) 7.4 nm. The mean of conductance variation and standard deviation is available on the plots (wherever applicable).

4.2 Nanopore Characterization using COMSOL Multiphysics

4.2.1 Further validation of COMSOL Model

As a further validation of the COMSOL Model for conductance measurements, the model was compared with similar work by other groups. For this purpose the geometry of the pore was modeled to duplicate the corresponding work. Results from the couple of such comparisons is discussed in this section.

- Comparison with work by Min Jun Kim, *et al* [28]

  In this work, Min Jun Kim, *et al* designed an analytical model to match the conductance measured from their experiments. A truncated double cone geometry was used in the work. This geometry was duplicated and used in the COMSOL model with appropriate parameters to obtain a conductance fit. In Figure 4.9 the inset shows

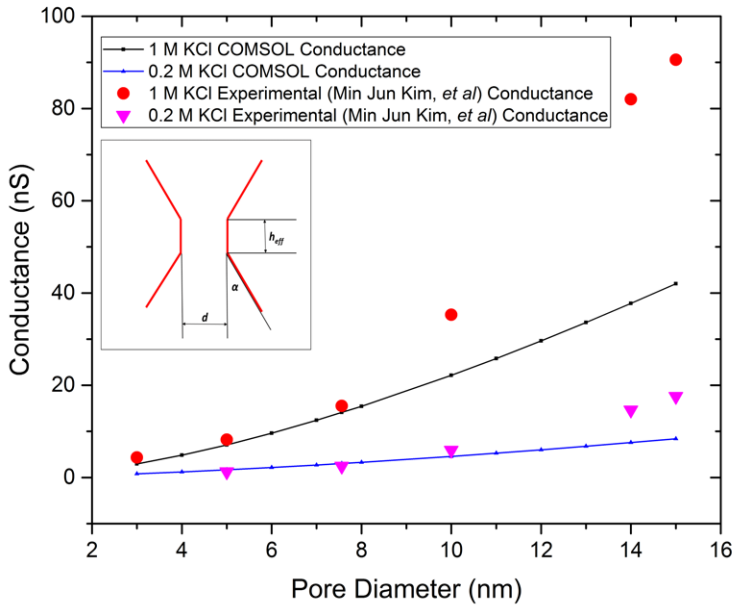

Figure 4.9: Simulated Conductance fit for Min Jun Kim, *et al* experimental conductance.Inset shows geometry of pore used in the work by Min Jun Kim, *et al*.

the pore geometry, where h_{eff} = (17±1) and (18±1) nm for the 1 and 0.2 M data, respectively, $\alpha = 30° \pm 2°$ for both cases, and d is the pore diameter. Figure 4.9 shows the comparison between simulated conductance and Min Jun Kim, *et al* experimental conductance. The error between literature [28] experimental and simulated conductance remained less than 30% for pore sizes below 10 nm in both the 1 M

and 0.2 M KCl data, and increases above 50% for higher pore sizes. This difference could be due to the COMSOL model over predicting the effect of access resistance (the resistance along the curved path near the pore inlet and outlet, as explained in chapter 2) at higher pore sizes [7], effectively increasing the deviation of simulated conductance from Min Jun Kim, *et al* experimental data, at higher pore sizes.

- Comparison with work by Kowalczyk, *et al* [7]
  In this work, Kowalczyk, *et al* deduced analytical models for cylindrical and hyperbolic pores. Equation 2.4 was initially used by them to fit their experimental data, however this equation was found to work only for cylindrically shaped pores. Later they deduced a hyperbolic (hour-glass shaped pores as explained in Section 4.1.5) analytical model to fit their experimental data. In this thesis, the analytical model parameters were inputed into COMSOL model to predict the efficiency of the COMSOL model in matching Kowalczyk, *et al* analytical and experimental conductance. The pore geometry for different simulated conductance fits were modeled by inputing the corresponding pore dimensions (cylindrical or hour-glass). For the cylindrical pore, the pore size and membrane thickness of 20 nm were used. For the hour-glass shaped pore, the pore size, outer diameter (pore size + 20 nm [7])and the membrane thickness of 20 nm were used. Simulations were conducted for pore sizes varying from 4 nm to 30 nm.

  Figure 4.10(a) and (b) shows the match between analytical and simulated conductance for cylindrical and hour-glass geometries respectively. Cylindrical and hour-glass pore analytical conductance models [7] match with the simulated conductance fits, within an error limit of < 13 % and $< 25\%$ respectively. The error could be due to the difference in the access resistance contribution in each model and/or due to effect of surface charge being considered in the COMSOL model. Figure 4.10 (c) shows the simulated hour-glass pore conductance fit for Kowalczyk, *et al* experimental data. It was observed that the simulated conductance fit matches the experimental data pretty closely, within an error limit of 25%.

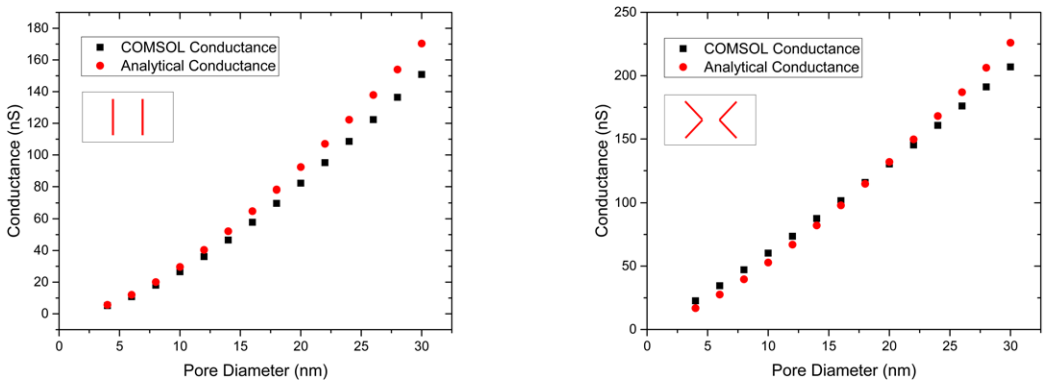

(a)

(b)

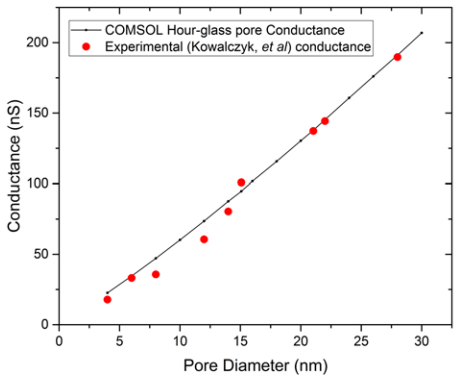

(c)

Figure 4.10: (a) Analytical (Kowalczyk, *et al*) and simulated conductance model match for cylindrical pore, (b) Analytical (Kowalczyk, *et al*) and simulated conductance model match for hour-glass pore. Insets shows shape of the pore geometry used in each case. (c) Simulated conductance (hour-glass pore) fit for experimental data (Kowalczyk, *et al*).

4.2.2 Pore structure dependence of Nanopore Conductance

Different pore fabrication techniques can produce different pore shapes and structures as explained in Chapter 2. A single pore fabrication technique could also be used to fabricate different pore structures (or shapes). For example, a parallel beam on a TEM could be used to sputter out cylindrically shaped pores, while a converging beam could be used to sputter out non-cylindrical pore shapes. The beam position and focusing could also be varied, to fabricate different shapes and structures. With the change in shape, structure or size, the conductance of a nanopore varies. The close match between the experimental and simulated conductance measurements for hour-glass shaped pores, provided an exciting opportunity

to observe the conductance of different pore structures.

COMSOL simulations were performed to measure the conductance for some of the commonly possible pore structures, namely, hour-glass, conical, hour-glass with cylindrical body, cylindrical. All pore structures, except the cylindrical shaped ones were built with a half cone angle of 12° (since, 12° is closer to literature values of half cone angles [50, 53] for pores fabricated using different techniques) for this study, with the rest of the parameters being constant. The hour-glass pore with cylindrical body was build with the cylindrical part being 18 nm ($\sim$ one-third of the pore thickness). Pore radius for all pore structures were varied from 1.1 nm to 15 nm (in order to be able to study small and big nanopores) to observe the effect on conductance.

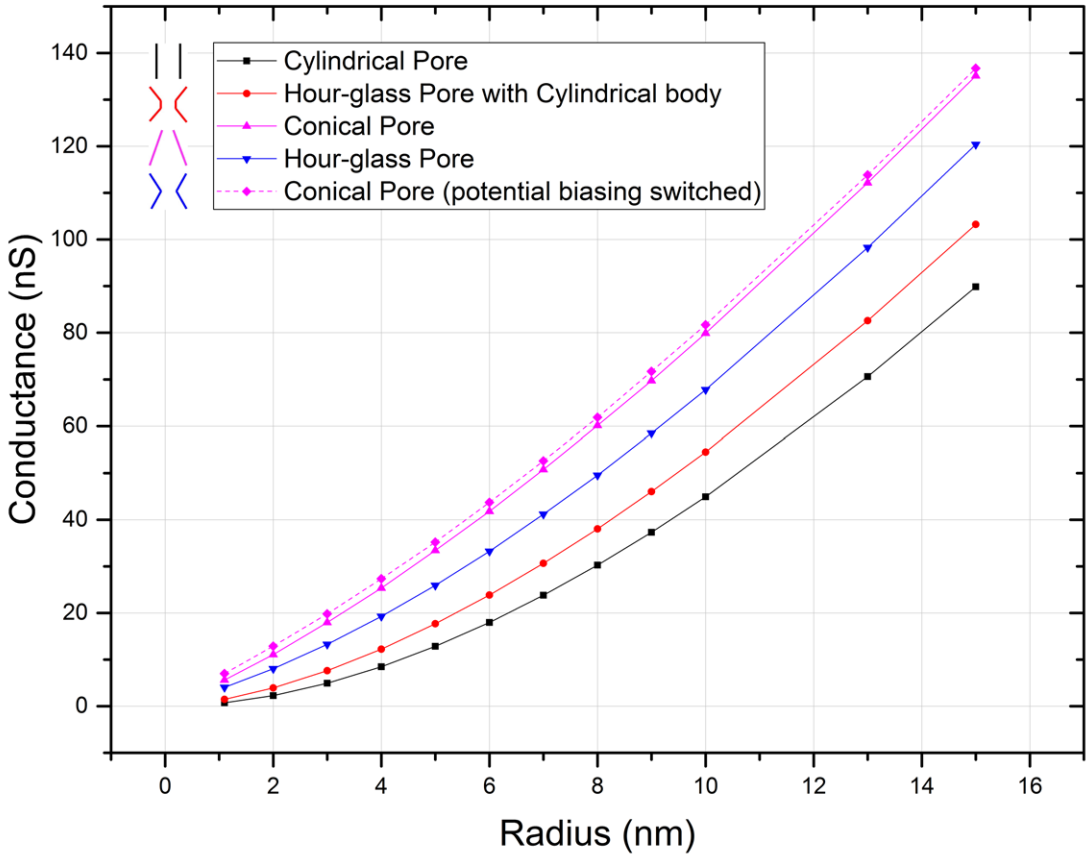

Figure 4.11: Conductance comparison of differently shaped pores for varying pore radius from COMSOL simulations. Different pore shapes include, cylindrical pore (curve in black), hour-glass pore with cylindrical body (curve in red), hour-glass pore (curve in blue), conical pore (curves in magenta). All pores are 50 nm thick, with a half cone angle of 12° (excepting cylindrical pore).

In Figure 4.11 it can be seen that the conductance of all pore structures follow a similar

Table 4.3: Simulated conductance of different pore structures for pore radius, 1.1 nm and 15 nm

Pore shape	1.1 nm pore radius	15 nm pore radius
Cylindrical	0.73 nS	89.86 nS
Hour-glass with cylindrical body	1.46 nS	103.26 nS
Hour-glass	4.03 nS	120.39 nS
Conical	5.61 nS	135.12 nS
Conical (biasing switched)	7.01 nS	136.75 nS

trend. However for a given pore radius, conductance was observed to be largest in the case of conical pore structure among all the structures and the least for the cylindrical pore structure. The conductance of different pore structures (for a given pore radius) followed the order, conical > hour-glass > hour-glass pore with cylindrical body > cylindrical as shown in Table 4.3. The conductance of the nanopore seems to increase with the volume of the pore. Interestingly, the two fits for the conical pore (curves in magenta color) are the simulated conductance curves for opposing polarity of applied bias. Conical pore owing to the asymmetric ion fluxes at the pore, hosts a phenomenon called ion current rectification (ICR) [58–60]. Owing to ICR, for a given pore size, the nanopore current (magnitude) for a particular potential bias is slightly higher than the current (magnitude) for the same potential bias of opposing polarity. Further discussion on ICR is presented in Sections 4.2.2.1, 4.2.3.4.

The simulation technique can be used to predict the exact shape and structure of a pore to obtain a desired conductance. It can also be used to simulate a conductance fit for a particular pore shape and structure, which could be used to predict the experimental conductance expected of different nanopore sizes.

4.2.2.1 Ion current rectification

Some conically shaped pores were fabricated using JEOL2200 FS TEM, to observe the conductance. Similar beam parameters as explained in section 3.1.2.2 were used, with the beam intensified at base of the pore to make conical pores. Tomography was performed to predict the pore structure and half cone angle (measured using ImageJ), the inset on Figure 4.12 is the tomography image of a conically shaped pore (tomography imaging and pore current measurements were done on different pores with similar pore structure and

fabricated using similar beam parameters). Results from the current measurement of one

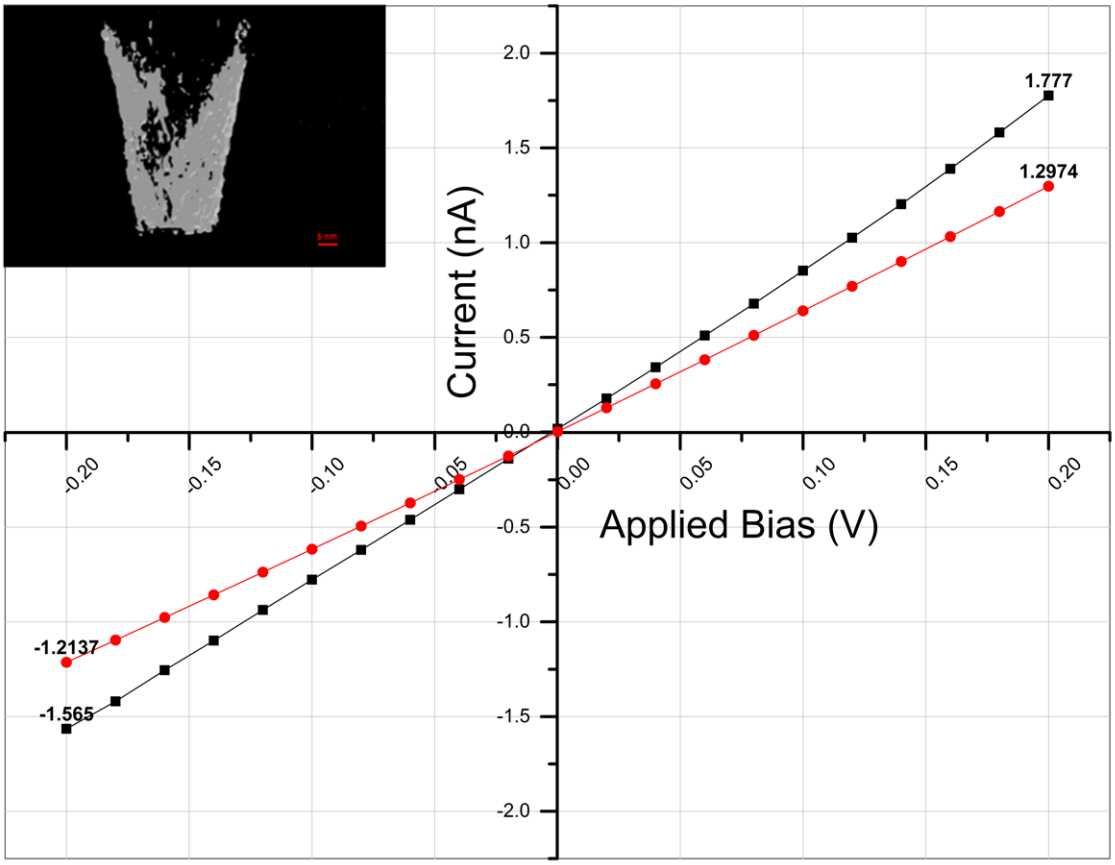

Figure 4.12: ICR in conical nanopores. Experimental (black) and simulated current (red) vs applied bias plots for a 4 nm conical pore with a half cone angle of 4.5°, measured in 1M KCl. Inset shows the TEM tomography image of a conical nanopore.

such conical pore is shown in Figure 4.12. The pore current of a 4 nm conical pore with a half cone angle of 4.5° was measured in 1M KCl at pH 8.0, by varying the potential bias from -200 mV to 200 mV. The geometry of the pore for simulation was obtained from tomography (measured using ImageJ) and the simulated current vs applied potential was plotted along with the experimentally measured current. The experimental current deviates from the simulated current within an error range of 25%. Conical pore, owing to its asymmetrical structure displayed ion current rectification, with the pore current being higher in amplitude for positive potential biasing (1.78 nA for 200 mV), than for negative potential biasing of same amplitude (-1.57 nA for -200 mV), as shown in Figure 4.12.

4.2.3 Effect of Pore dimensions, Electrode length and distance variation, Surface charge of membrane on Pore Conductance

Several parametric factors affect the conductance of a nanopore, the physical dimensional and chemical surface parameters of the nanopore are of particular interest for the purpose of this thesis. COMSOL Multiphysics was used to perform a detailed analysis, to study the effect on conductance due to the variation in the following parameters,

- Pore or membrane thickness
- Half cone angle
- Electrode length and position
- Surface charge
- Pore volume

The pore conductance might be uniquely affected in each case, the results from this analysis is discussed in this section. Standard values from section 3.3.1 were used for unmentioned parameters in all the analysis, in the following discussions.

4.2.3.1 Effect of Pore thickness on Nanopore Conductance

Thickness of the free standing nitride membrane on which the nanopores could vary depending upon the nitride deposition technique and/or time. Thickness could also be changed by etching or milling the membrane, this would directly affect the thickness of the pore fabricated on the free standing membrane. The effect of pore thickness on conductance was studied for two types of pore structures : a simple symmetric cylindrical structure without any conical feature and an unsymmetric conical pore. Pore size of 10 nm was used for both the pore structures, and a half cone angle of 12° was used for the conical pore, with the rest of the parameters being constant. For the cylindrical pore, a mathematical model proposed by Kowalcyzk, *et al* [7] was used to compare the simulation results,

$$G = \sigma \left[\frac{4l}{\pi d^2} + \frac{1}{d} \right]^{-1} \tag{4.5}$$

where σ is the conductivity of the electrolyte solution with a standard value of 10.5 $\mathrm{S.m^{-1}}$ for 1 M KCl at 25 °C, l is the thickness of the pore, d the pore size and G the conductance. The simulated conductance results matched the mathematical conductance within an error limit of 10 % − 13 %. Figure 4.13 shows the effect of varying the pore thickness from 10

nm to 1000 nm on conductance of a cylindrical pore. It can be seen that the conductance decreases rapidly with increasing pore thickness until about 100 nm indicating the higher and higher resistance offered to the flow of ionic fluid by the increasing pore thickness. Beyond 100 nm the rate of conductance decrease slows down, almost saturating at higher thickness, indicating a saturation in the resistance offered by the pore to the fluid flow beyond a certain pore thickness (100 nm).

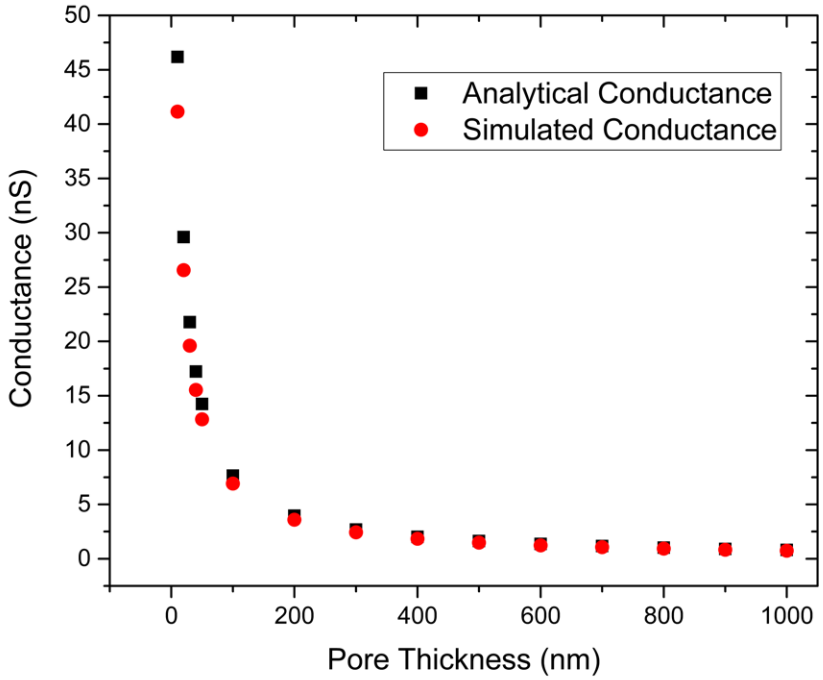

Figure 4.13: Conductance dependence on pore thickness of cylindrical pore. Pore size being 10 nm and pore thickness of 50 nm.

In the case of conical pore, the pore thickness was again varied from 10 nm to 1000 nm, and it was observed that the conductance fell steeply up until 100 nm and the rate of fall reduced greatly from there on. The longer the pore thickness, the higher is the resistance for ionic fluid to pass through the pore, and thus the conductance is lower. In the case of conical pore, the conductance reduces with increasing pore length, but the pore base also widens up as pore length increases. The rate of decrease in resistance reduced with the increasing pore length and saturated at around 900 nm pore thickness. The conductance seemed to slightly increase at pore thickness beyond 900 nm, with the widened pore probably offering lesser resistance to ionic fluid flow at higher pore thickness (> 1 μm). Further analysis is

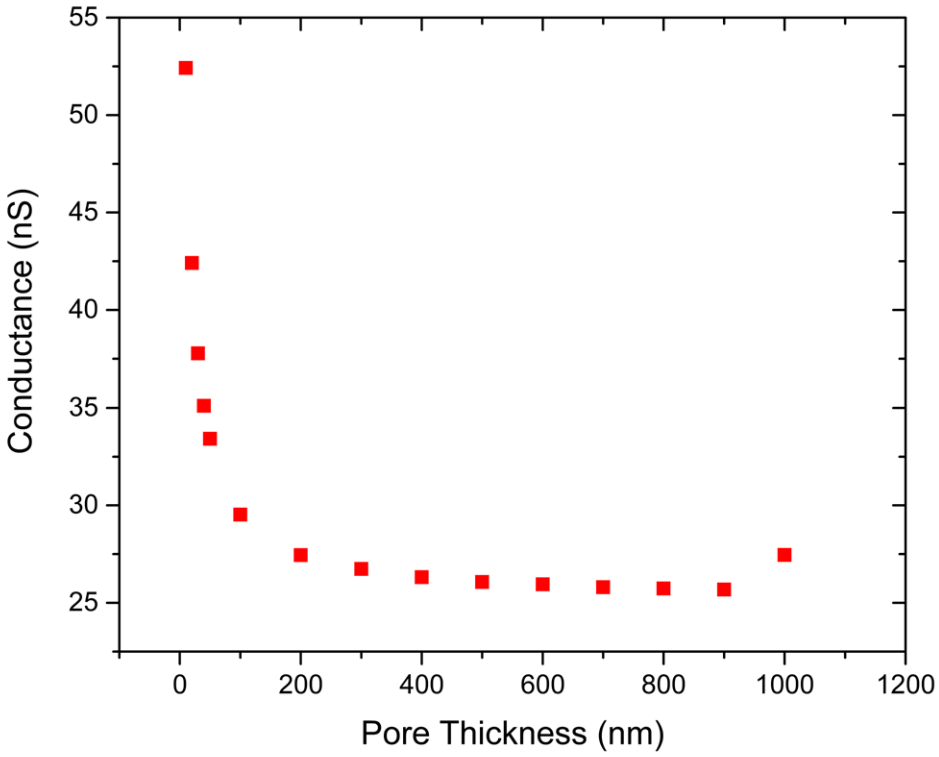

Figure 4.14: Conductance dependence on pore thickness of conical pore. Pore size being 10 nm and pore thickness of 50 nm.

required to understand this behavior. Figure 4.14 graphically describes these results.

4.2.3.2 Effect of Half cone angle on pore Conductance

Half cone angle of a non-cylindrical pore structure is defined by the pore fabrication technique and the parameters involved in the fabrication like time, power, material property, etc. The effect of half cone angle on conductance was studied. For this purpose, the half cone angle of a 10 nm conical pore, 50 nm thick was varied from 0° (cylindrical structure) to 12°, the corresponding change in conductance was measured using COMSOL simulations.

In Figure 4.15 it can be seen that the conductance increases almost linearly with the increase in half cone angle from an initial cylindrical pore structure (0° half cone angle). Conductance improved by about three times from 12.84 nS to 33.4 nS on varying the half cone angle from 0° to 12°. This can be partially attributed to the widening of the pore base offering lesser and lesser resistance to ionic fluid flow. It was observed that the conductance is highly sensitive to change in cone angle for pore sizes $\sim$ 10 nm.

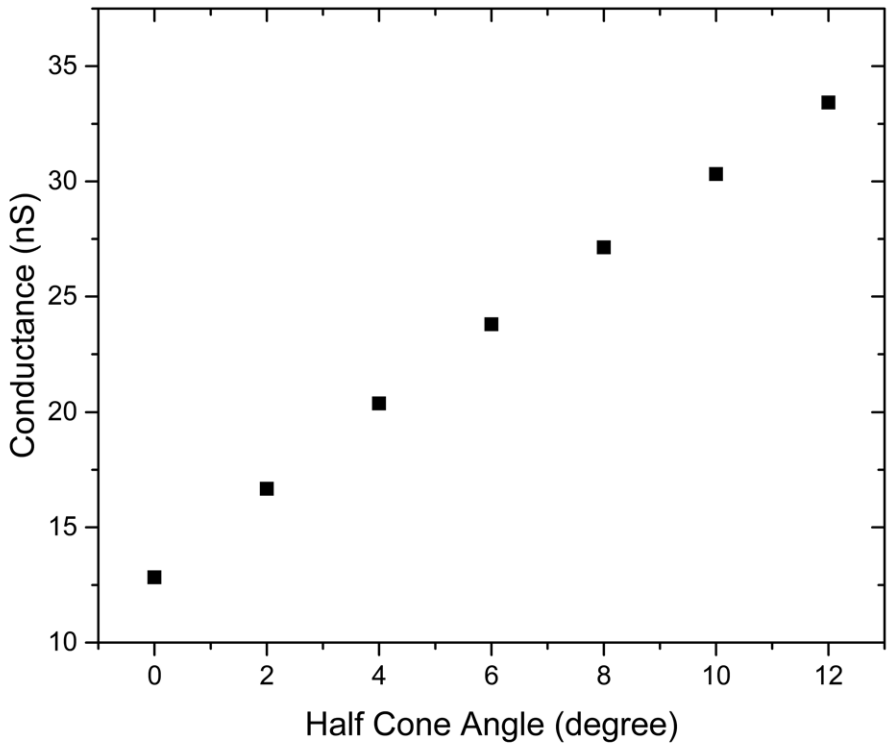

Figure 4.15: Effect of half cone angle on pore conductance. Pore size being 10 nm and pore thickness of 50 nm.

4.2.3.3 Effect of Electrode Length and position on Conductance

Electrode length and position (distance from pore) vary greatly in a real, conductance measurement experiment. However, the position or length of the electrode does not affect the pore conductance in real experiments. COMSOL simulations were used to verify and study the effect of electrode length and distance from the pore on the conductance of a 10 nm cylindrical pore. The cell dimension (two half cells, each 5 x 5 μm) used in the COMSOL model was modified to vary the length of the electrode, distance of the electrode from the pore. Since the electrodes are positioned at the ends of the cell (refer to section 3.3.3.2), varying the half cell dimension not only varies the cell size but also changes the position and length of the electrode. Both the parameters, length and distance were varied from 5 μm to 0.6 mm to observe the change (if any) in conductance. These simulations were highly time and capacity consuming, owing to the bigger geometry and higher number of mesh elements. A slightly coarser mesh structure was built to compensate for the time

and capacity of the processor.

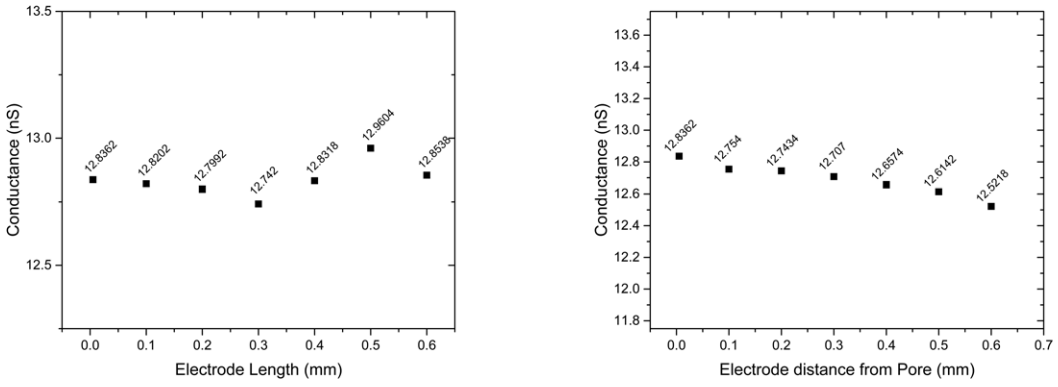

(a) (b)

Figure 4.16: Conductance dependence on electrode position for a 10 nm cylindrical pore measured using simulation. (a) Conductance vs Electrode length variation, (b) Conductance vs Electrode distance from pore variation

In Figure 4.16 it can be seen that the conductance is almost constant for all length, distance variations of the electrode. This result indicates that the pore conductance is weakly dependent on electrode position. The result was in concurrence with the experiment, as the position of electrode did not affect the conductance in experiments as well. It is also worth mentioning that, the results from this study also supports that changing the cell size does not affect the measured conductance. This result was in turn used to fix the cell size at 5 x 5 μm in section 3.3.2.

4.2.3.4 Effect of membrane Surface charge on Conductance

When a dielectric material like SiN_x is immersed in an ionic solution, the material develops a surface charge, the magnitude and polarity of the surface charge is dependent on the pH [54], concentration and temperature of the solution. For a given pH, concentration and temperature of a solution, the surface charge is also different for different materials. Different membrane materials develop a unique surface charge when immersed in an ionic solution, for example Al_2O_3 nanopores develop a positive surface charge [61], while SiO_2 [50] or Si_3N_4 nanopores develop a negative surface charge.

To observe the effect of surface charge on simulated current (and thus conductance), the surface charge on the membrane (both the pore surface and outer membrane) was varied from -0.1 C.m^{-2} to 0.1 C.m^{-2} (generally different materials display a surface charge

within this range) for a 6 nm cylindrical pore, at an applied bias of 0.5 V. In Figure 4.17 it can be seen that the total current (blue in color) reduces with reducing surface charge only to increase again for positive surface charge. The current for the positive surface charge is also almost equal to the current for negative surface charge of same magnitude. A deeper inspection into the individual ion currents provides an insight for the above discussed trend. Since K^+ and Cl^- ions have similar mobility, diffusivity and hydrated ion size,

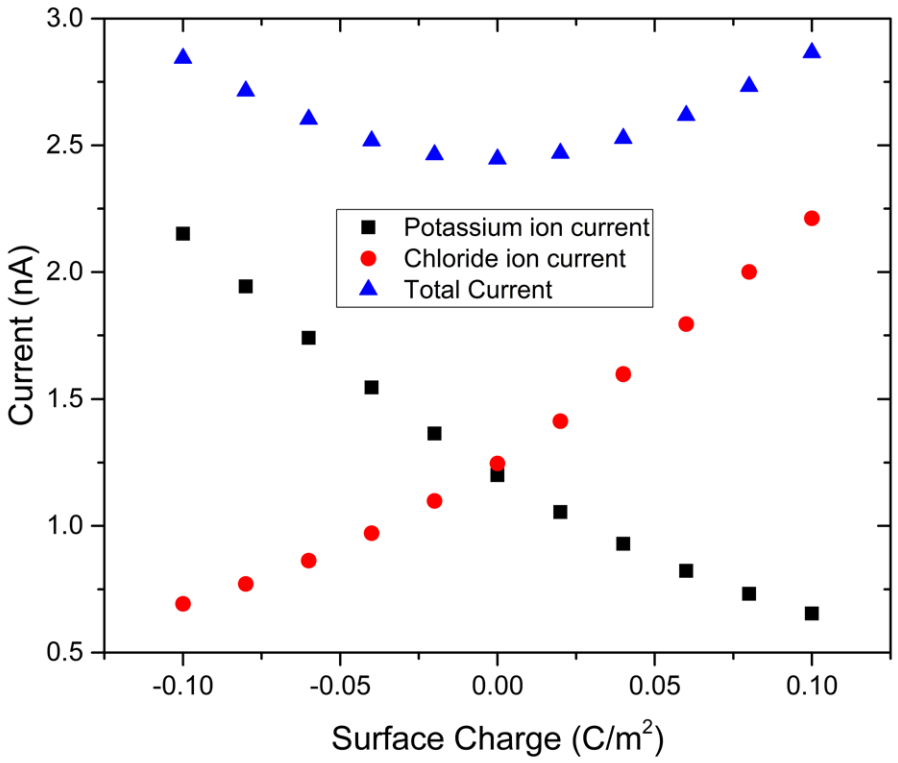

Figure 4.17: Effect of surface charge on current in a 6 nm cylindrical pore.

a highly negatively charged surface hosts a higher population of mobile K^+ ions in the pore, and as the charge magnitude reduces, the population of K^+ ion reduces, only to be compensated by Cl^- ions. This process reverses for a positive charge, with the Cl^- ion population being compensated by K^+ ion for reducing positive charge. Resulting in the total current contribution being the similar for membrane surface charges of same magnitude and opposing polarity, as illustrated in Figure 4.17.

In a conical nanopore, the current trend with variation in surface charge is shown in Figure 4.18. A 0.5 V potential bias was applied on a 6 nm conical pore (with a half cone

angle of 12°) for this study.

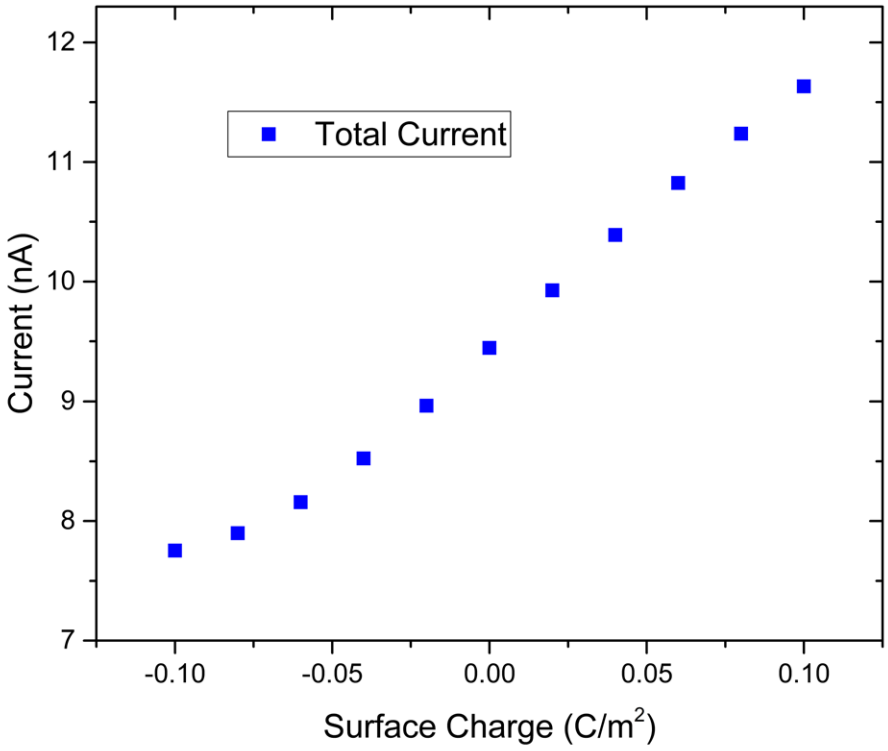

Figure 4.18: Effect of surface charge on current in a 6 nm conical pore.

As seen in the figure, current increases consistently when the surface charge is varied from -0.1 C.m^{-2} to 0.1 C.m^{-2}, in contrast to the cylindrical pore. This was understood by looking into the ion fluxes at the pore. The explanation is similar to the explanation for ICR given by Woermann [58–60]. According to H.S.White and A.Bund [50], for a negatively charged pore surface like SiN_x, when a positive bias is applied (at the bottom electrode), the electrical transference roots a reduction in local KCl concentration and thus ionic current at the pore region. For a positively charged surface, the population of mobile Cl^- is higher (and higher transference number) in the double layer, owing to the affinity towards Cl^-. When a positive bias is applied (at the bottom electrode), the Cl^- ions coming into the pore from the top reservoir are free to flow through, but the K^+ trying to reach the ground (top) electrode are deflected back, due to anion transference number reaching unity at the narrow end of the pore. This process renders a higher local KCl concentration (and thus current) at the pore region. The trend shown in Figure 4.18 would switch for a negative applied

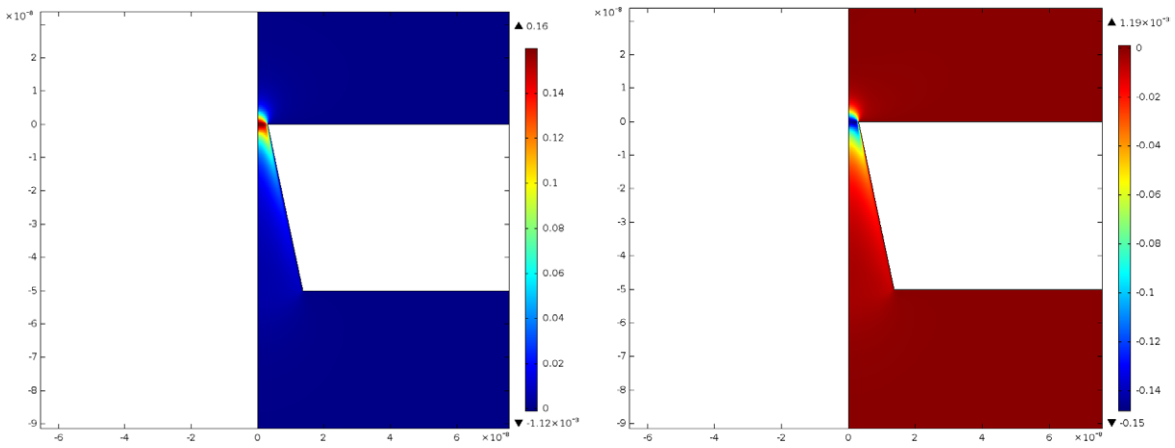

(a) (b)

Figure 4.19: z plane velocity profiles for pores with different surface charges (a) for a membrane with negative surface charge of -0.02 C.m^{-2}, (b) for a membrane with positive surface charge of 0.02 C.m^{-2}. Both at 0.5 V applied bias. Scale bar on the images is for the z velocity in units of m.s^{-1}.

bias. This is further illustrated by the COMSOL 2D plots for velocity of the fluid along the axis of rotation (z-axis velocity). In Figure 4.19, the z velocity profile of a negatively charged surface shows a increase in fluid velocity just at the pore mouth (narrow region of the pore), indicating a local decrease of KCl concentration at pore mouth and thus the pore current. However for a positively charged surface there is a drift in velocity at the pore mouth, indicating local increase in KCl concentration (and pore current). Notice that, the above explained process does not happen in a cylindrical pore, owing to its symmetric geometry around either electrolytic reservoirs, it is also worth mentioning that a 6 nm pore was chosen for this study, since the ICR effect is magnified for pore sizes similar to the order of double layer thickness [50] ($\sim$ 3 Å for 1 M KCl).

4.2.3.5 Conductance and Pore volume relation

The pore conductance and volume of the pore share an interesting relationship. Conductance increases with increase in volume of the pore for a given pore thickness. The ratio of conductance and volume of pore (conductance per unit pore volume, with units of nS.nm^{-3}) of different pore shapes, when plotted against increasing pore size, gave rise to a unique trend. The measurements were performed using the COMSOL model, with all non cylindrical pore structures built with a fixed half cone angle of 12° and thickness of 50 nm. Figure 4.20 shows the trend of conductance per unit pore volume with varying pore sizes for different pore structures.

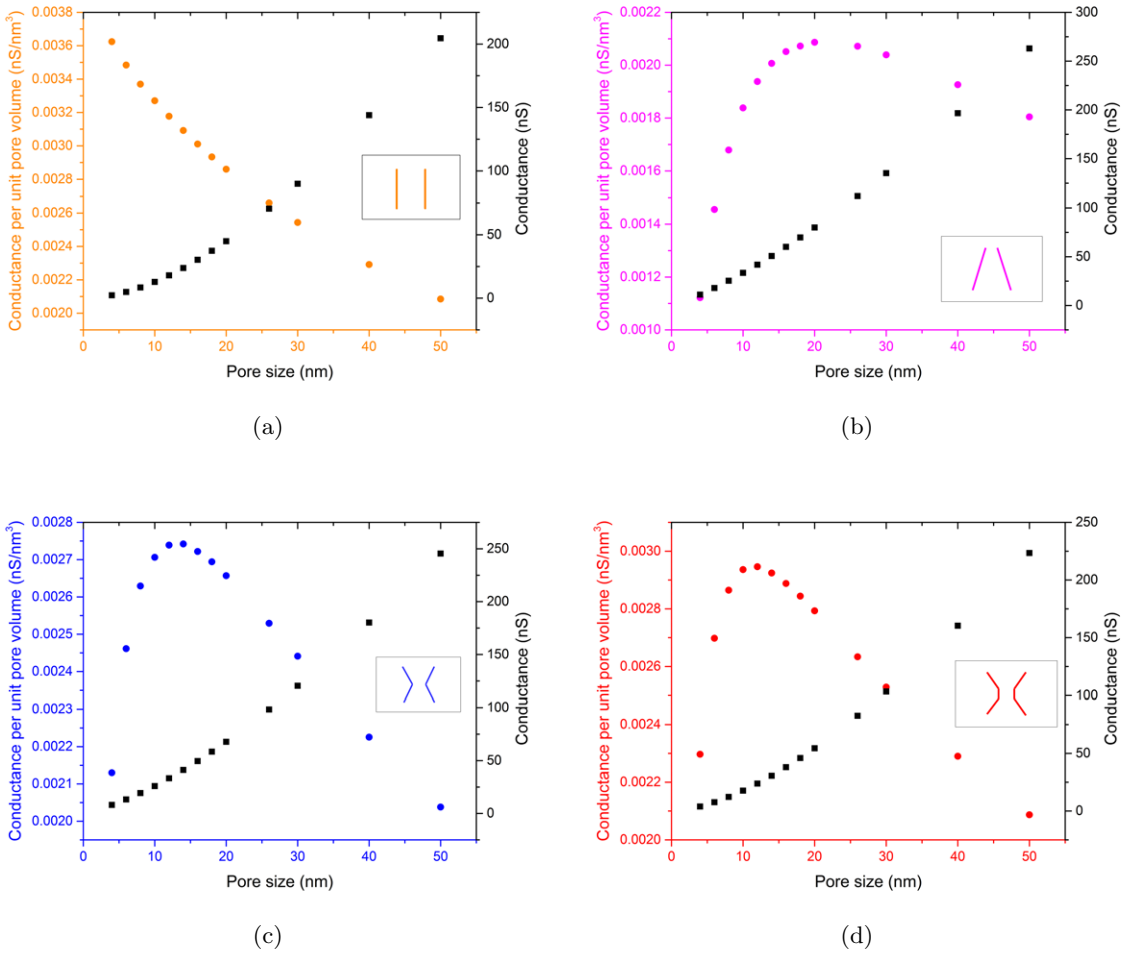

Figure 4.20: Variation of conductance per unit pore volume with pore size, for different pore structures. Inset in each plot depicts the structure of the corresponding pore (a) Cylindrical pore, (b) Conical Pore (c) Hour-glass shaped pore, (d) Hour-glass shaped pore with cylindrical body.

The following discussion is an attempt to understand this unique trend. For all non-cylindrical pore structures as the pore size increases, the rate of increase in conductance dominates over the rate of increase in pore volume (upto 10 - 15 nm). In other words, the effect of increase in flux of ions (through the pore) which contributes to the conductance, grows stronger and stronger as the pore size (and pore volume) increases upto 10 - 15 nm. The initial positive slope displayed by conductance per unit pore volume vs pore size plots in Figure 4.20(b,c,d) indicate the above explained. With further increase in pore size (beyond 10 - 15 nm), the plot of conductance per unit pore volume vs pore size displays an opposing trend, indicating the weakening effect of ion flux increase on the conductance

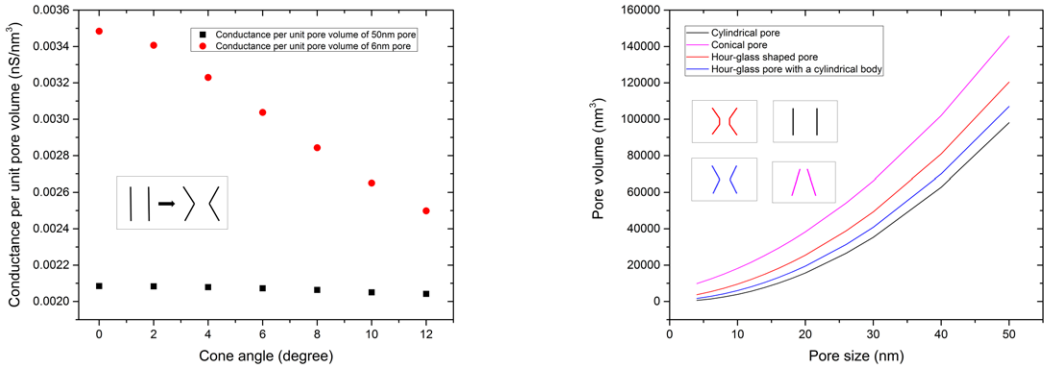

Figure 4.21: (a) Variation of conductance per unit pore volume with half cone angle for two different pores, 6 nm (red circles) and 50 nm (black cubes) in size. Inset shows the pore structure change with introduction of half cone angle to the cylindrical pore, (b) Pore volume variation with pore size for different pore structures. Inset shows the different pore shapes with corresponding color code.

with exponential increase in pore volume. This could be due to effect of access resistance being higher at larger pore sizes for conical pore shapes [7]. However, in a cylindrical pore, the rate of increase of pore volume seems to dominate consistently over the rate of conductance increase as indicated by the constant negative slope in Figure 4.20(a). It can also be observed in Figures 4.20(a,b,c,d) and 4.21(b) that the pore conductance and volume, respectively, increase in a similar fashion for all pore structures.

Further analysis showed that the conductance per unit pore volume is very sensitive when the pore structure transforms from cylindrical to hour-glass shape (varying half cone angle from 0° to 12°) for sizes below 10 - 15 nm, (a 6 nm pore was studied). While being less sensitive when the same analysis was done on a bigger pore (50 nm pore). This in turn indicated that pore structure is an important factor in defining the unique trend of conductance per unit pore volume, at pore sizes below 10 - 15 nm. Figure 4.21(a) shows the variation of conductance per unit pore volume with half cone angle for the 6 nm and 50 nm pore. The reason for the difference in trend portrayed by the cylindrical pore structure was still unclear. Further analysis is required to understand the principle behind the existence of such an unique trend for conductance per unit pore volume as observed in non-cylindrical pore structures. More detailed study is required to understand the practical effects of conductance pore unit pore volume on conductance.

4.2.3.6 Steady state time

A time study was performed with the COMSOL model to predict the time taken for the potential to stabilize in the pore region, upon application. The model was run assuming no fluid flow, due to computational complexity involved with fluid flow. For this study the time was varied from 0 to 10 ms, at a step of 0.1 ms. It was observed that the potential breaks down at the pore region, in around 1.5 ms, and continues to stabilize up until $\sim$ 9 ms (for a 5x5 μm reservoir on either side of the pore). Figure 4.22 shows series of 3D images demonstrating the potential stabilization in and around the pore for a 10 nm cylindrical pore, 50 nm thick (cylindrical part of the figures) at an applied potential bias of 100 mV.

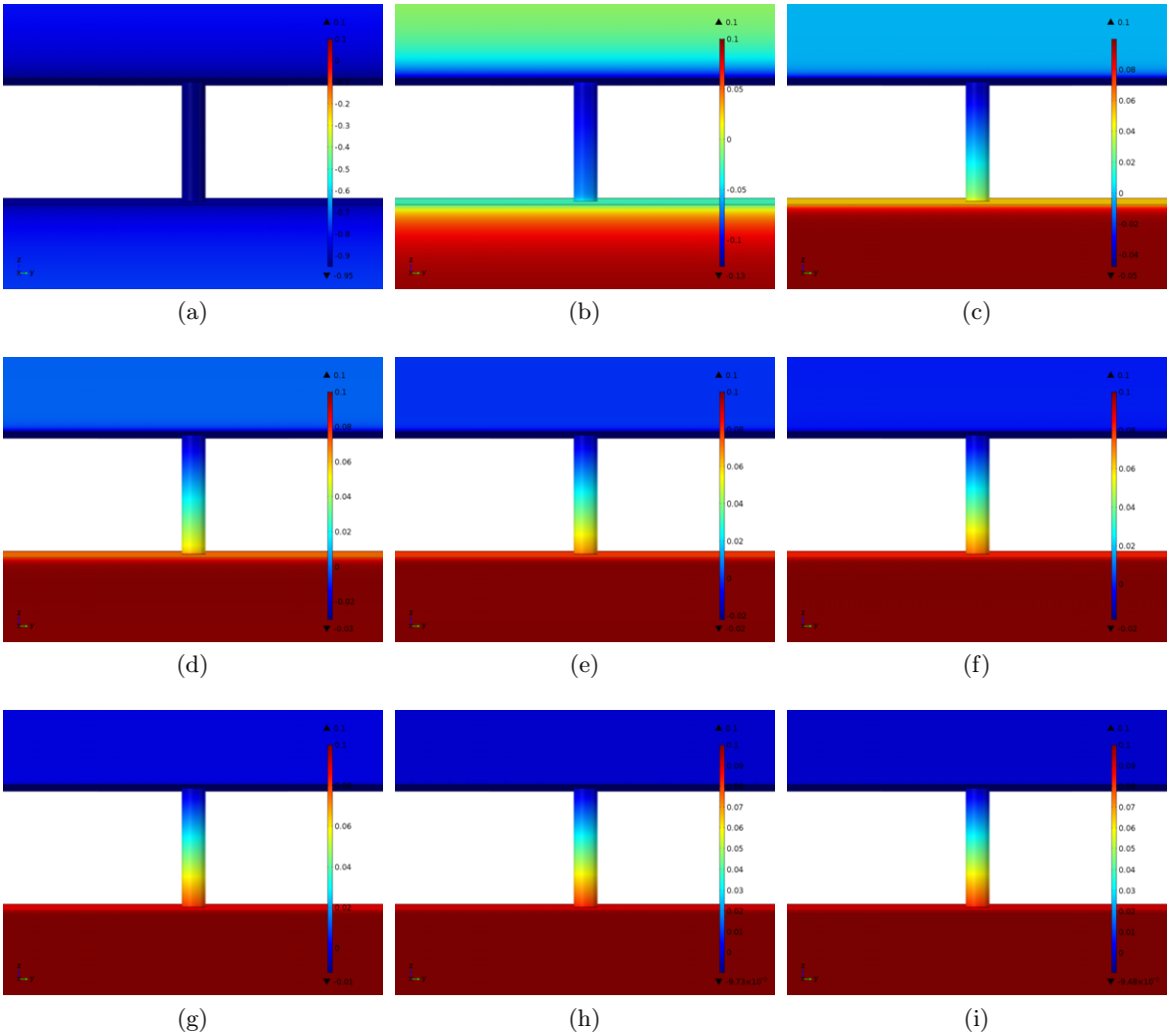

Figure 4.22: 3D Potential distribution plots at different times (a) 0.1 ms, (b) 0.5 ms, (c) 1.0 ms, (d) 1.5 ms, (e) 2.0 ms, (f) 2.5 ms, (g) 5 ms, (h) 9 ms, (i) 10 ms. Scale bar on the images is for the electric potential in units of Volts.

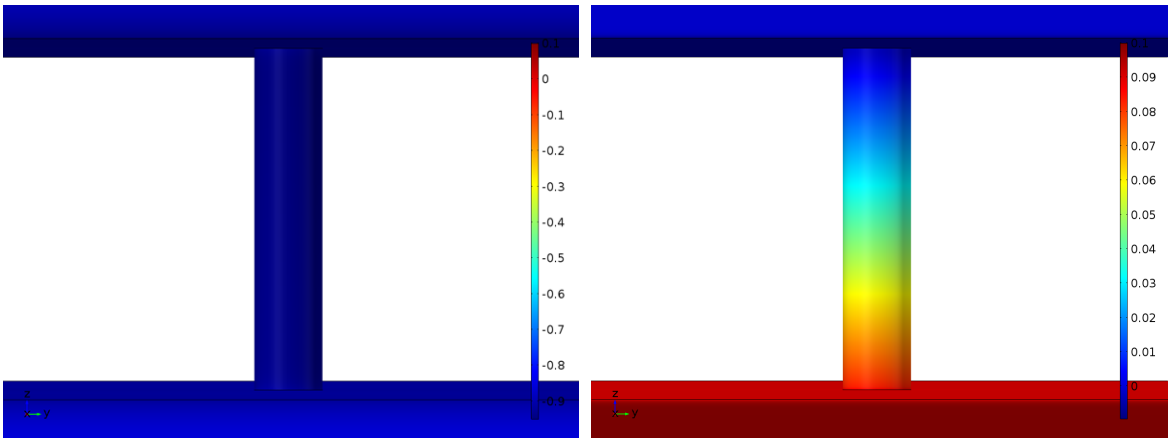

(a) (b)

Figure 4.23: Zoomed out view of the 3D potential distribution plots at (a) 0.1 ms and (b) 10 ms. Scale bar on the images is for the electric potential in units of Volts.

Figure 4.23 shows the zoomed in view of the 3D potential distribution at the initial (0.1 ms) and final (10 ms) time limits of this study. It was also observed that the steady state time increased by $\sim$ 1 ms for 6x6 μm cell model, and decreased by $\sim$ 1 ms for a 4x4 μm cell model (3D results not presented here). In a real case scenario, where the cell is of the order of millimeters, the steady state time for potential to stabilize was predicted to be of the order of a few hundred milliseconds or a few seconds. It is worth mentioning that, the model when run with integrated fluid flow physcis (Navier-Stokes) might provide more accurate result, and the results discussed here are preliminary.

This section discussed the characterization of solid state nanopores by experimentation and simulation. The conductance dependence on various parameters like pore shape, structure, size, height, and other physical and chemical surface properties were discussed in detail. As a succeeding step in solid state nanopore testing, the nanopores were tested for their sensing ability, preliminary results from the sensing experiments are presented in the next section.

4.3 Preliminary Results of Molecular Sensing with Solid State Nanopores

Upon characterization of solid state nanopores, the validation of their functionality was done by exploring the potential sensing applications. As explained in Chapter 2, nanopore sensing is a powerful and convenient technique for molecular translocation, DNA sequencing and protein detection, to name a few. In general terms, when an analyte passes through the nanopore, a certain volume of ionic fluid that contributed to the pore current is being displaced by the translocating analyte. Each translocating analyte has a specific size and length, which would result in an unique blockage (for dielectric material) or spike (for material with higher conductivity than the ionic solution) in the observed current. Thus the smaller the nanopore size the better is the sensing ability of the pore, since the measured current for larger pores (>200 nm) is probably unaffected by the presence of a small foreign molecule in the pore [7].

4.3.1 Molecular Translocation

For all molecular detection testing, the analyte was added to one of the electrolytic chambers (*cis* chamber, chamber here refers to half cell) and pulled electrophoretically to the electrode in other chamber (*trans* chamber). The analyte after addition was refluxed several times using a clean pipette to ensure uniform mixing. Molecular detection is highly sensitive and demands a stable current signal. Before every molecular testing, conductance of the mounted pore was measured, with potential sweeps as described in section 4.1.2. Unstable current is an indication of partially wet pore, which is undesirable for molecular sensing, as the resolution is greatly affected by an unstable baseline current. The presence of dirt or unwanted foreign particulate (like detergent) also affects the measurement, by causing pore blockage or unexpected translocation events. In such a scenario the chip bearing pore, measurement cell, PDMS gaskets, electrodes are cleaned and the ionic solution is filtered and degassed as explained in section 3.2.2. The cell, gaskets, the chip and buffer solutions were stored in a class 1000 cleanroom to avoid contamination.

4.3.1.1 Lambda DNA Translocation

Initial testing of the nanopore sensing ability involved an attempt to observe the translocation of Lambda double stranded DNA (λ-dsDNA). Lambda DNA is isolated from bacteriophage Lambda, and is the genome of the bacteriophage. Lambda DNA owing to its long chain length (48.5 Kbp in length, and a negative molecular charge), is bound to be

electrophoreticlly pulled by a positive applied bias, when mixed into an ionic solution. Also, dsDNA translocation has been observed by other groups [28, 55] previously, and thus could be used as a reference to test the sensing ability of nanopores (and a good initial point for molecular translocation testing). Lambda DNA, 48.5 Kbp in length was purchased from NEW ENGLAND BioLabs Inc. A typical lambda DNA is 2.2 nm wide.

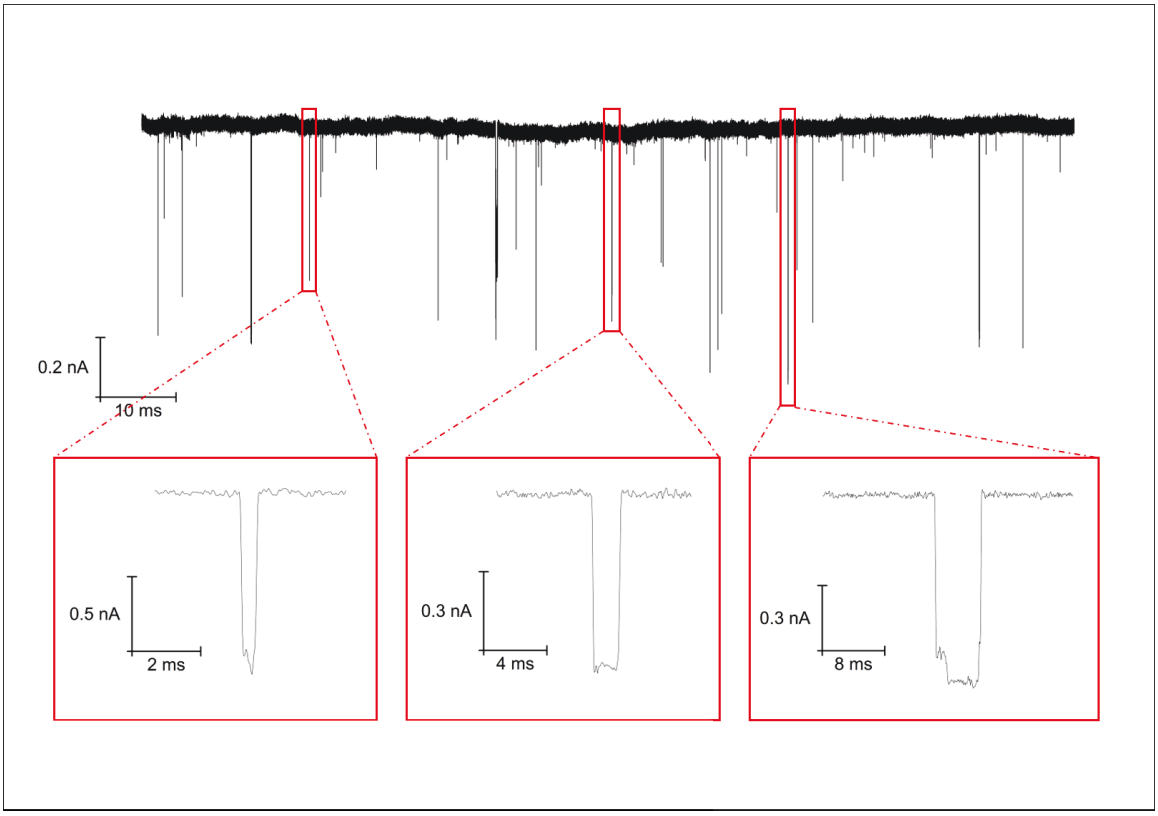

Figure 4.24: Translocation of Lambda dsDNA , 48.5 kbp in length, with a concentration of 1 ng/μL in 1 M KCl, for an applied bias of 400 mV. Zoomed out translocation profiles are displayed at the bottom.

Translocation measurements were performed by adding the analyte to the *cis* chamber at a concentration of 1 - 2 ng/μL in 1M KCl. The chamber with analyte molecules was refluxed repeatedly, to ensure uniform mixing. Potential bias was then applied to electrophoretically pull the molecule to *trans* chamber. Figure 4.24 shows the recording of lambda DNA translocaion through a 5 nm pore. A transient event was considered as translocation when the observed blockade amplitude portrayed a recognizable deviation from base line current. Current blockades created by the analyte as it translocates through the pore for an applied bias of 400 mV is shown in Figure 4.24, with some of the translocations zoomed in at the bottom. Current blockade amplitudes of the translocations were comparable with similar

experiments from literature (Min jun Kim, *et al* [28] observed the translocation of dsDNA (150 bp in length) through a 4 nm pore (on a 50 nm thick SiN_x membrane) in 1 M KCl at an applied bias of 400 mV).

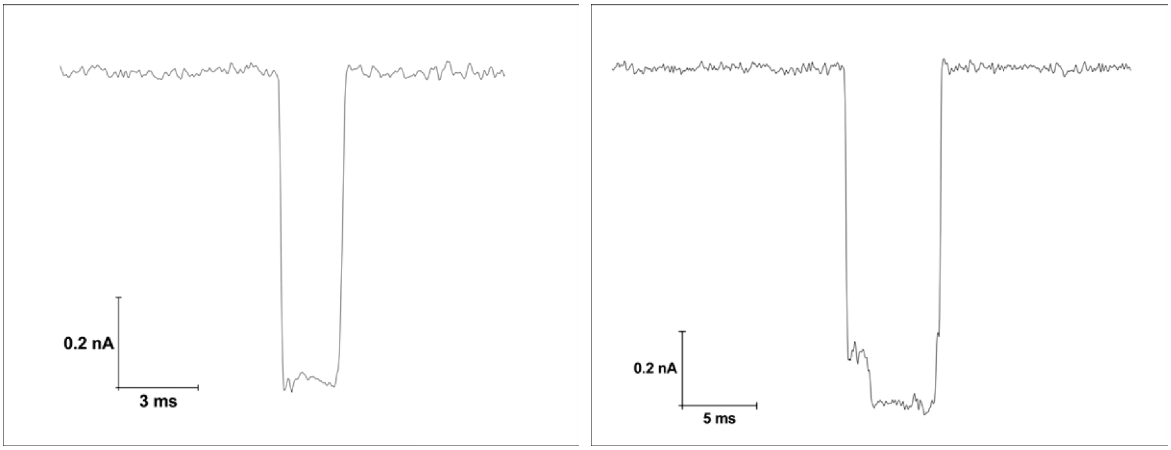

(a) (b)

Figure 4.25: Lambda DNA conformation prediction as it translocates. (a) unfolded and (b) folded DNA translocation

Two types of translocations seemed to dominate the recording, Figure 4.25 shows the two types of translocations. Figure 4.25(a) shows a straight, unfolded molecule translocation, with the blockage amplitude being 0.7 nA over a duration of 2 ms. Figure 4.25(b) shows a partially folded molecule translocation, blockage amplitude being slightly higher at 0.9 nA. A deeper look at Figure 4.25(b), and two steps are noticeable. The first step (0.7 nA in amplitude) corresponds to the unfolded part of the translocating DNA with a shorter amplitude over a duration of $\sim 1 - 2$ ms, the second bigger step (0.9 nA in amplitude) happens when the larger, folded part of the molecule translocates [24]. The larger translocation duration (6 ms) of the partially folded molecule suggests that the chain length of this particular strand is higher (than the unfolded straight molecule). As discussed in chapter 2, the length and conformation of the translocating DNA molecule can be predicted from the duration and steps observed along the amplitude of the current blockage respectively. From Figure 4.25(b), the DNA strands conformation and length can be predicted as follows, the unfolded linear part of the strand initially translocates through the pore causing a drop of 0.7 nA in the current level. This unfolded part of the strand is shorter ($1 - 2$ ms) compared to the folded part which follows later, causing a larger current level drop (0.9nA over $4 - 5$ ms). This measurement with λ - dsDNA demonstrates the capability of using the nanopore for biomolecular sesnsing.

4.3.1.2 Polysaccharide Translocation

Glycosaminoglycans (GAG), a complex polysaccharide found in tissues, cartilage [62], acts as a shock absorber and lubricant [63]. Glycosaminoglycan encode functional information in a sequence specific manner similar to DNA [64]. Sequencing of the sulfation code of a sulfated GAG might provide insight into several therapeutic solutions [65]. As a preliminary attempt, the translocation of a sulfated GAG was observed. Figure 4.26(c) is an schematic image of the long chain polysaccharide, with random sulfation sites.

Sulfated glycosaminoglycan polysaccharide (Chondroitin sulfate sodium salt from shark cartilage purchased from SIGMA-ALDRICH) translocation through a 7.4 nm hour-glass shaped pore for an applied bias of 200 mV, is shown in Figure 4.26(a). The sample at a concentration of 1 ng/μL was mixed into the *cis* chamber, and pulled by the electrode placed in *trans* chamber. The recording can be seen dominated by a single type of event (about 180 pA blockage amplitude). A histogram analysis of this segment of the recording event count vs the current amplitude (analysis performed over $\sim$ 4 minutes 30 seconds recording period), is shown in image 4.26(b), two distinct peaks can be noticed, one for the baseline current and the other for $\sim$ 180 pA long translocations.

After about 20 minutes of continuous recording, a shorter ($\sim$ 80 pA) translocation was also observed, events shown in Figure 4.27(a). Two types of translocations started appearing, with smaller ($\sim$ 80 pA) and larger amplitude ($\sim$ 180 pA). The translocations with smaller amplitude ($\sim$ 80 pA) correspond to unfolded straight analytes and the translocations with larger amplitude ($\sim$ 180 pA) correspond to folded analyte translocation. Histogram analysis in Figure 4.27(b) for the segment of recording (over 1 minute 30 seconds time period) under discussion, shows three distinct peaks for the folded, unfolded molecules and baseline current respectively, confirming the presence of two types of distinct translocations. The duration of the translocations were very long, sometimes being hundreds of milliseconds. This could have been due to molecular aggregation or collision, the exact reason is not understood. More detailed study is required to have a better understanding of the size, chain length and sulfation code of the polysaccharide molecule.

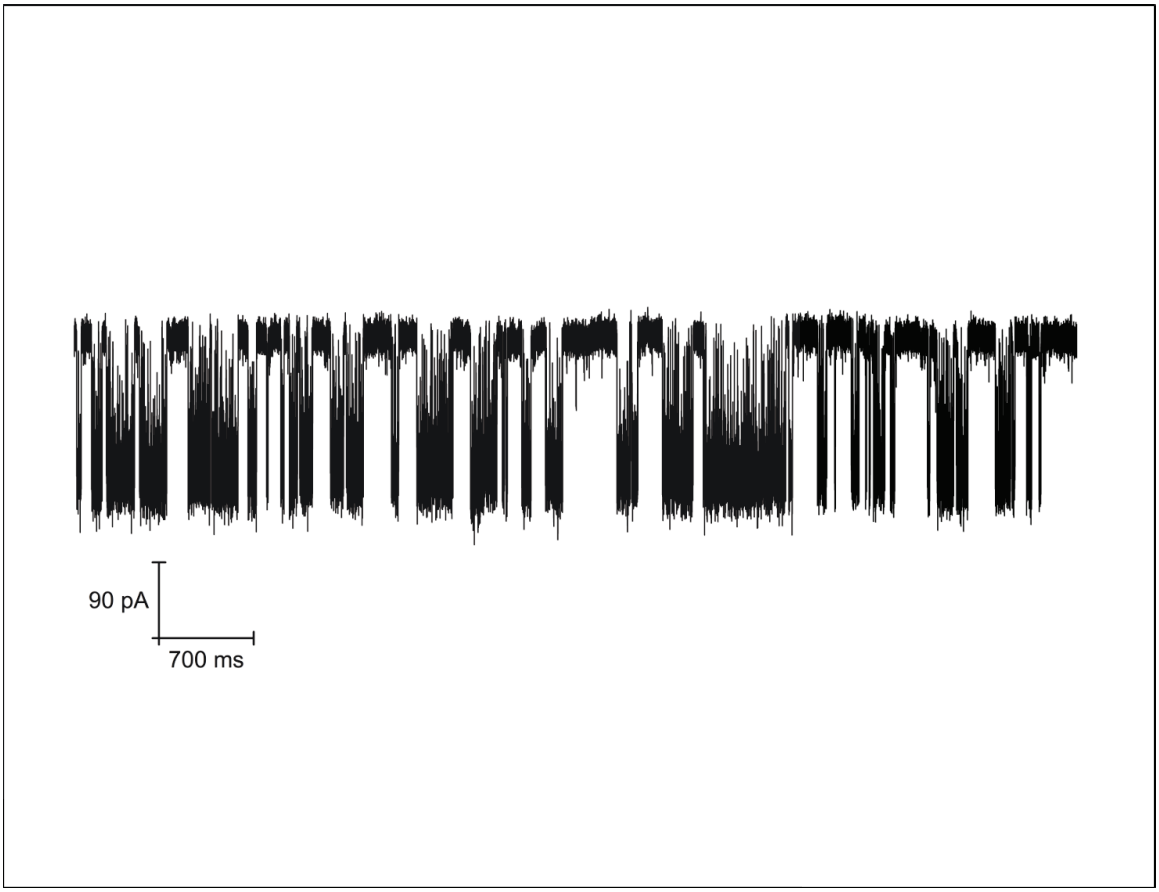

(a)

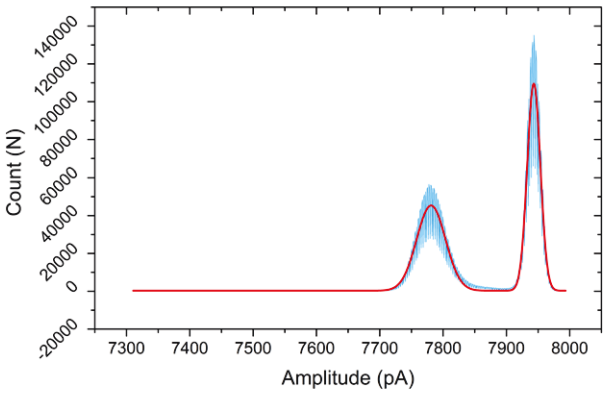

(b)

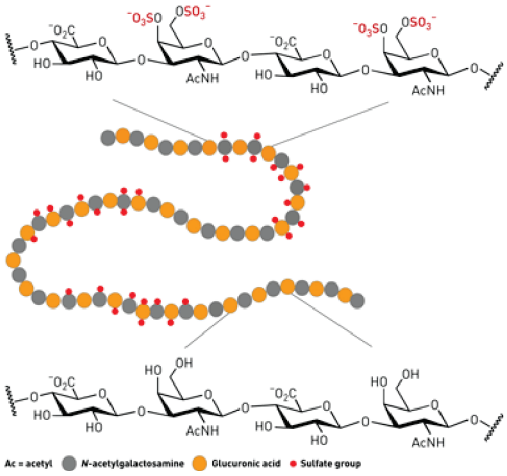

(c)

Figure 4.26: (a) Recording of polysaccharide translocation through a 7.4 nm pore, at analyte dilution of 1 ng/μL in 1 M KCl, (b) Histogram analysis of event count vs amplitude, (c) Schematic image of polysaccharide chain obtained from [8].

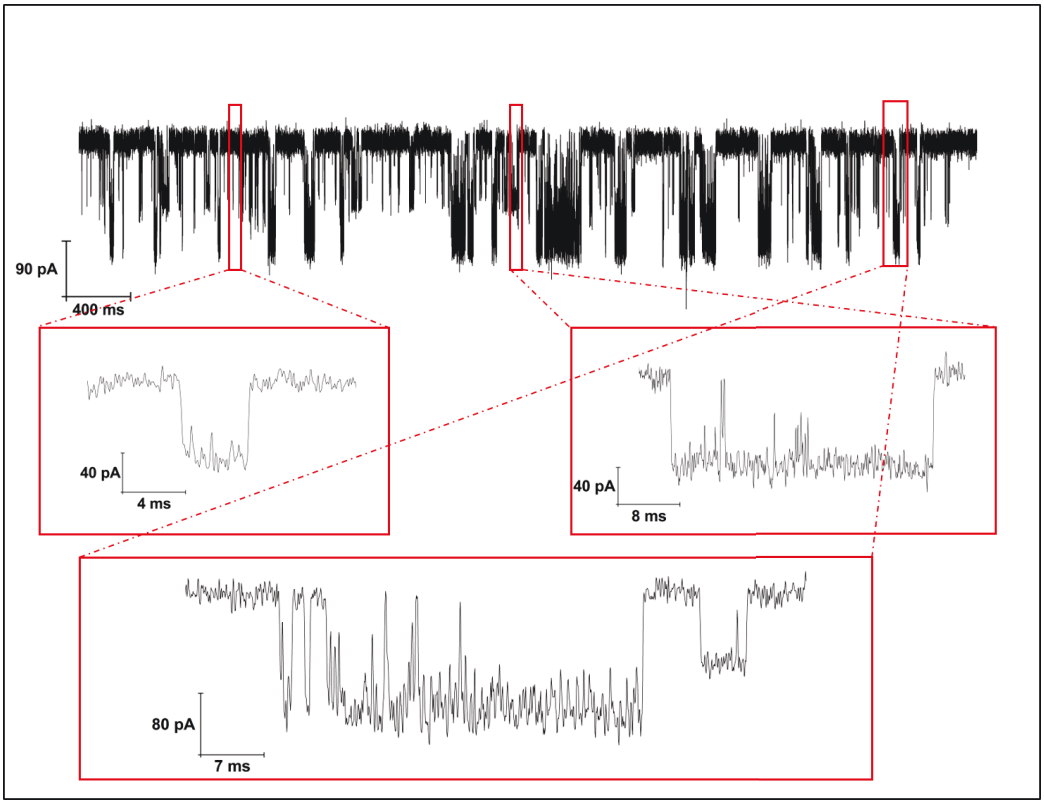

(a)

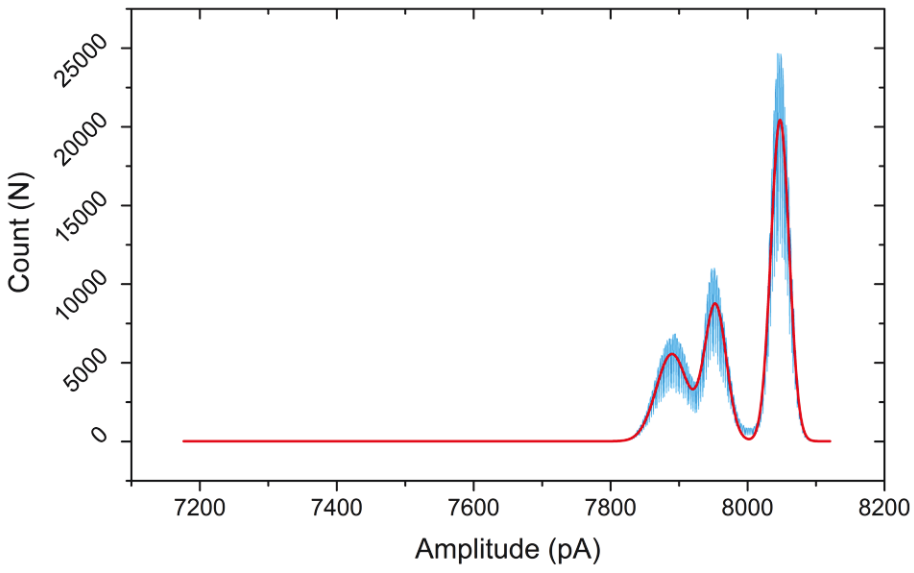

(b)

Figure 4.27: (a) Polysaccharide translocation recording displaying folded and unfolded molecule translocation, Zoomed out views of the translocation are shown at the bottom, (b) Histogram analysis of event count vs amplitude.

4.3.2 Hybrid Nanopore

Solid state nanopores are durable, susceptible to harsh chemical environment and can be integrated with semiconductor technology, however, they also suffer from poor specificity and are not as effective as biological pores in controlling the translocation speed of analyte molecule. A hybrid pore as discussed in the introduction would bridge the capabilities of both biological and solid state pore and thereby would aid in overcoming several disadvantages. A hybrid pore built with a selective sensing ability (biological pore) on a durable and rigid platform (solid state pore) would act as a powerful sensor. The results from an attempt to create such a hybrid pore with biological and solid state counter parts, is presented in this section.

4.3.2.1 OmpG-DC30 insertion onto Solid state nanopore

Outer membrane protein G (OmpG), a barrel shaped porin pore was chosen as the biological pore. Outer membrane proteins in general display gating ability [66, 67]. Gating ability of OmpG protein pore could be used to partially open and close the pore [68]. Figure 4.28 shows the schematic image of OmpG protein. Engineered OmpG monomer (with an outer diameter ~ 3.3 nm and inner diameter ~ 2 nm) attached to a DC - 30 (deoxyribose cytosine, 30 base pairs in length) DNA strand (buffered in detergent) was used for protein insertion onto solid state nanopore. The DNA strand was attached to the protein to electrphoretically guide the protein pore onto the solid state pore in the electrolytic solution (owing to the DNA strands higher molecular charge in ionic solution). The sample at a concentration of 1 ng/μL was mixed into the *cis* chamber, and pulled towards a 4.7 nm pore by applying a potential of 200 mV at the electrode in the *trans* chamber.

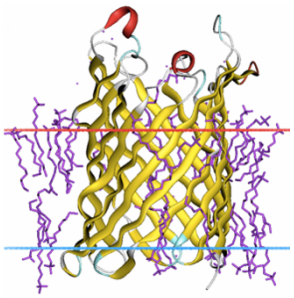

Figure 4.28: Schematic image of OmpG protein obtained from [9].

Figure 4.29 shows the current recording of this experiment. Multiple steps can be observed along the length of the recording at different times, these steps correspond to the

multiple protein insertion onto the solid state pore. In Figure 4.29(a) the regions circled

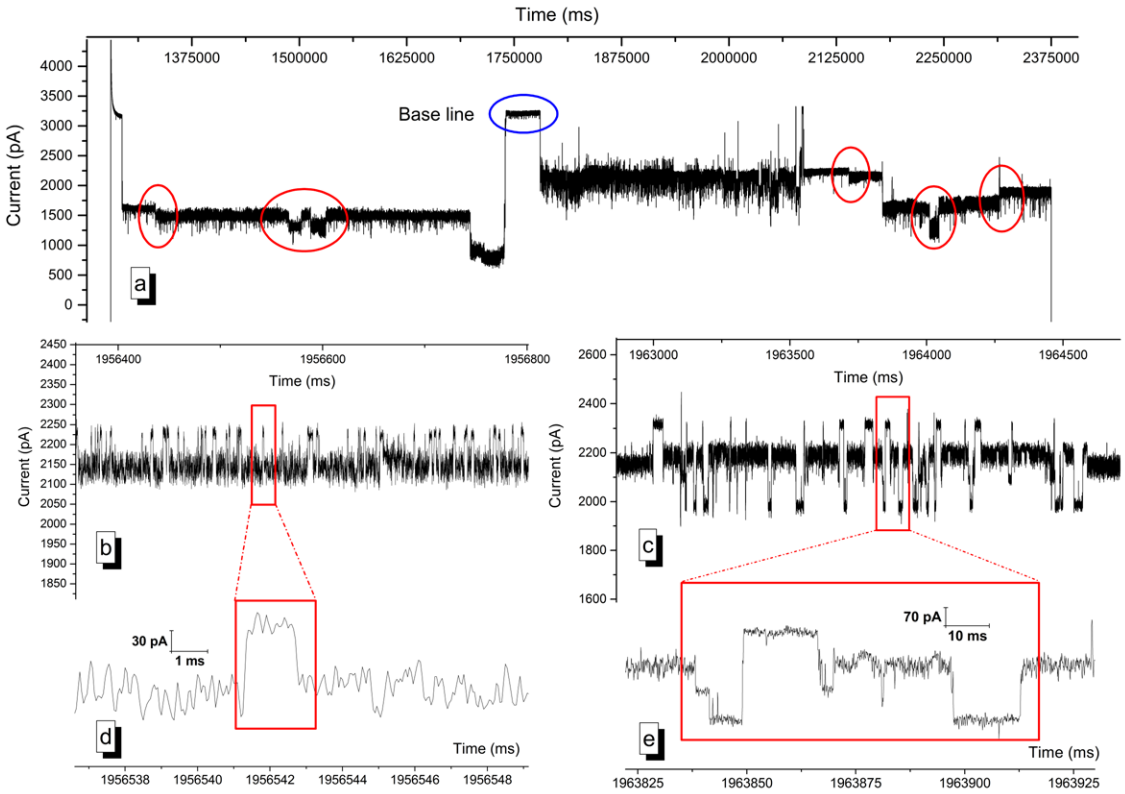

Figure 4.29: (a) Recording of OmpG-DC 30 insertion onto solid state nanopore, (b, d) zoomed in image of single protein gating, (c, e) zoomed in image of multiple protein gating.

in red, indicate some of the regions where, additional protein(s) insertion or protein(s) removal rooted a step in the observed current, and the region circled in blue indicates the base line current without any protein insertion. Figure 4.29(b) shows image of (probable) single protein partial opening and partial closing. The protein is said to be in partially open state when the current level is seen to be slightly higher than the base state (partially closed state). Figure 4.29(d) is a zoomed in image, showing protein partial open state, with the current level being $\sim$ 100 pA higher than the closed state, for a duration of $\sim$ 2 ms. Figure 4.29(c) shows image of multiple protein opening and closing simultaneously, eventually creating multiple partially open and close states with varying amplitude and duration, as demonstrated by the multiple steps in Figure 4.29(e). The multiple proteins remained inserted for the rest of the recording period ($\sim$ 23 minutes), until the insertions were removed by applying a negative bias (- 200 mV) on the *trans* electrode to push the inserted proteins away towards the *cis* (ground) electrode.

4.3.2.2 OmpG (without attached DNA) insertion onto Solid state nanopore

Next step involved an attempt at inserting the OmpG protein, without an attached DNA to guide it towards the pore. A 4.1 nm pore was used for this purpose (the 4.7 nm sized pore from preceding experiment had unfortunately broken during repeated measurements and cleaning sessions). The protein sample (buffered with detergent) was mixed into the *cis* chamber at a concentration of 1 ng/μL. Upon uniform mixing, the potential was slowly increased. At about 80 mV the protein insertion started becoming noticeable. Figure 4.30

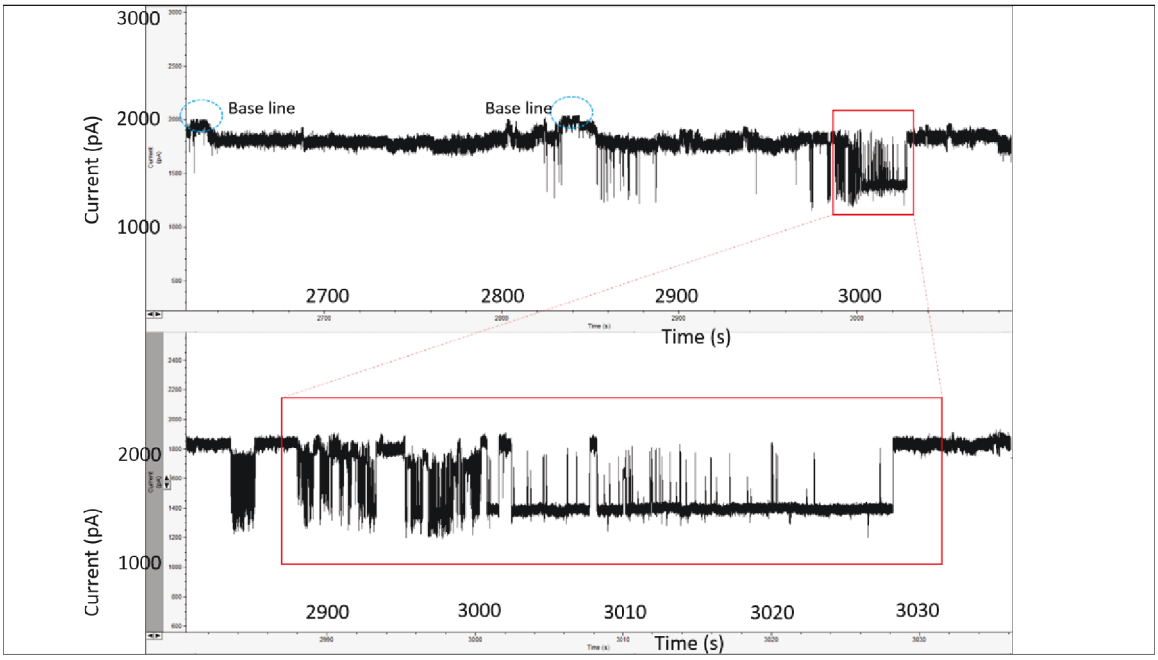

Figure 4.30: Recording of OmpG insertion onto solid state nanopore, zoomed in view of the multiple protein gating at the bottom.

shows the insertion of OmpG protein(s) onto the solid state pore at an applied bias of 200 mV. The drop in current from the base line level could be noticed on the image, upon protein insertion. Further opening and closing of the protein was also observed subsequently. The partially open and close states are zoomed in at the bottom of Figure 4.30 (refer to Appendix B for information on characterization and gating ability of OmpG in lipid bilayers).

It was also observed that the protein remained in open state for the majority of the recording duration. The reason for this was unknown. This experiment showed that it is possible to insert bare OmpG monomers, onto a solid state nanopore, without the need for a guiding DNA strand. However the OmpG protein is barrel-shaped unlike the mushroom

shaped α-haemolysin pore (the mushroom shape aids in easy insertion of the biological pore onto solid state pore, as observed in the work by Hall *et al* [6]), and hence single protein insertion onto solid state pore would require further fine tuning of the solid state pore shape and structure to ensure smooth and tight insertion. Opening and closing of OmpG can be used to selectively let molecules into the pore (pH of the solution can be used as the switch to open and close OmpG [68]). This could be used as an elegant, fast and cheap separation technique to differentiate and separate bio-markers selectively based on size or charge.

4.3.3 Summary

Preliminary studies of molecular sensing were performed with different analytes. Lambda DNA translocation was analyzed, and the length and conformation of the translocating analyte was predicted. Further fine tuning of the pore size and shape, might aid in sequencing of DNA strands. DNA sequencing would be useful in identifying modifications in genes, to detect and cure gene related diseases, in forensics, in understanding evolution and ecology, etc.

Sulfated polysaccharide translocation experiments were conducted and the folded and unfolded conformation of the analyte as it translocated was observed. Determining the sequence of polysaccharide, would provide the solution to treatment of various diseases.

OmpG-DC30 insertion onto solid state nanopore with partial opening and closing was demonstrated. Protein insertion without a guiding DNA was also demonstrated. Further fine tuning of the solid state nanopore size and shape might aid in precise and fitted insertion of single protein, improving the quality of the measured current and enhancing the application oriented value of such a powerful sensor.

Chapter 5

Conclusion and Future work

With the growing demand for single molecule detection using solid-state nanopores, it is necessary to perform a detailed characterization of solid state nanopores. The purpose of this thesis is to characterize and understand small nanopores (less than 10 nm in size) based on conductance measurements. This would also help in fabricating custom designed nanopores with desired size and shape. Solid state nanopores were fabricated based on a SiN_x membrane and processed through a series of cleaning steps in a cleanroom environment. The cleanroom-based handling of nanopores rendered them more usable ($>$ 70 % of nanopores in all experiments were found clean). For the purpose of characterization, conductance determination model compatible with different shapes, sizes and chemical environment was setup using COMSOL Multiphysics. Hour-glass shaped pores varying in size from 4 to 8 nm were fabricated using TEM and their experimental conductance was measured (in 1 M KCl) between 9.34 nS (4.1 nm pore) and 27.34 nS (7.4 nm pore). A conductance fit for the experimental conductance was obtained by performing simulations (replicating the experimental conditions). The simulated conductance fit matched the experimental data within an error range of 5% to 30%.

The study regarding conductance dependence of solid state nanopore shape and size, revealed how critical the nanopore shape is in defining the conductance. Nanopore conductance varied quickly with the slightest change in shape, radius and/or half cone angle. A 5 nm cylindrical pore on a 50 nm thick SiN_x displayed a conductance of 12.84 nS, while a hour-glass shaped pore of the same size, half cone angle of 12° displayed almost double the conductance at 25.91 nS. It was also observed that a conical nanopore portrays ICR, with the current magnitude for an applied potential bias varying based on biasing polarity. This was also confirmed by fabricating conical nanopores (using TEM) and experimentally measuring the pore current (pore current of a 4 nm conical pore with half cone angle of

4.5° was measured to be -1.57 nA at -200 mV and 1.78 nA at 200 mV). Introducing the concept of half cone angle into a cylindrical pore drastically increased its conductance from 12.84 nS to 33.5 nS, on varying half cone angle from 0° to 12°. The effect of surface charge of membrane on pore current was found to vary depending on symmetricity of the pore. While symmetric pores (cylindrical) display a symmetric current trend on varying surface charge of membrane from negative to positive, unsymmetric pore structure (conical) display an unsymmetric one. The effect of pore thickness on conductance for both cylindrical and conical pore was similar, with the conductance reducing as the pore thickness was increased from 10 nm to 1 μm. The pore conductance and volume shared an interesting relationship. Ratio of conductance and pore volume (conductance density) increased with increasing pore diameters for sizes below 10 - 15 nm, while displaying an opposing trend as the size increased (except in cylindrical pore shape). Essentially it was observed that the dimensions and surface charge of the pore significantly affects the behavior of an ionic fluid moving through it. Thus controlling this will change their performance.

Upon a detailed characterization of the nanopores, they were tested for their ability to sense molecules. Preliminary measurements of different molecular translocations (such as DNA, sulfated polysaccharide) were performed using solid state nanopores and their conformation was predicted. Initial tests on demonstration of a hybrid nanopore-based on OmpG protein in conjunction with the solid state pore were conducted. Protein insertion with and without a guiding DNA strand was also demonstrated. The ability of protein pore to partially close and open could be used for selective passage of molecules based on size and charge. This selective sensing ability of such a powerful nanopore opens up a wide array of applications in varying fields like medicine, forensics, biology and other sciences.

5.1 Ongoing and Future work

The nanopore sensing platform is clearly an elegant and powerful technique to explore different aspects of science and engineering. In order to efficiently use the sensor, the nanopore platform needs to be evolved and refined. Few of the ongoing and future work on making the sensing platform better, include,

5.1.1 Nanopore size tuning for hybrid nanopores and Modeling analyte molecule in simulation

Fabrication of nanopores less than 3 nm in size with proper size and shape tuning needs to be improved in order to insert a single protein pore smoothly and fittingly onto a solid

state pore. Helium ion microscope (HIM) is being considered for fabricating nanometer and sub nanometer sized nanopores with simultaneous thinning of membrane. These solid state nanopores can then be utilized in building improved multiple hybrid pore arrays equipped for different molecular sensing applications. COMSOL Multiphysics would be used to model and observe the translocation of an user defined molecule. Matlab codes will be used for this purpose [69].

5.1.2 High frequency noise reduction

With smaller nanopores, the capacitive noise or high frequency noise reduction needs to be improved in order to reduce noise levels. Some techniques to reduce noise levels include reducing the surface area of the free standing membrane (for further information on membrane surface area reduction refer to Appendix A) and/or applying a thin PDMS coating over the SiN_x surface (proven to be effective in reducing the high frequency noise [45]).

5.1.3 Multiple pore fabrication and simulation

Array of pores have been fabricated on a single free standing membrane, results from conductance characterization of such a pore array is shown in Appendix B. These array of pores could be used to detect higher amount of analyte or in parallel detection with isolated pores (requires additional measurement setup). Reproducibility of the nanopore in both radius and shape remains a main challenge. The ability to control the precise structure and shape of the nanopore will provide a promising solution for accurate parallel measurement. Multiple pore fabrication would be attempted using HIM. Supercomputers would be used to build and run 3D COMSOL models of a multiple pore system. This could then be further utilized to observe and characterize array of nanopores in a parallel detection scenario.

5.1.4 Surface functionalization of solid state nanopore

Ongoing experiments are being conducted to plasma activate SiN_x surface in presence of H_2 plasma and to utilize the activated surface for protein attachment under UV light. mcherry protein attachment on SiN_x surface was performed ([70]). This technique could be used to attach a biological molecule onto a functionalized solid state pore, to form a hybrid pore. Such a hybrid pore could then be used in selective sensing by controlling the pore size and pore affinity (towards different molecules).

5.1.5 Alternate hybrid nanopore proposal

The ability to construct a hybrid pore with multiple layers of silicon nitride, polymer and protein surfaces, might tremendously improve the ability of hybrid nanopores to act as bio-computers. For this purpose, a thin layer of polymer (< 10 nm) would be grown on a functionalized SiN_x surface in and around the solid state pore. This surface would be used to seal (eliminating any cross interaction) and fit the protein pore onto the solid state pore. In this way multiple hybrid pores with parallel detection ability can be built on a single free standing membrane.

Bibliography

[1] David. Goodsell. PDB-101: Molecule of the Month Image Download.

[2] Jiali Li, Derek Stein, Ciaran McMullan, Daniel Branton, Michael J. Aziz, and Jene A. Golovchenko. Ion-beam sculpting at nanometre length scales. *Nature*, 412(6843):166–169, 2001.

[3] Ulrich F. Keyser. Enhancing nanopore sensing with DNA nanotechnology. *Nature Nanotechnology*, 11(2):106–108, 2016.

[4] Maria E Gracheva, Anlin Xiong, Aleksei Aksimentiev, Klaus Schulten, Gregory Timp, and Jean-Pierre Leburton. Simulation of the electric response of DNA translocation through a semiconductor nanoporecapacitor. *Nanotechnology*, 17(3):622–633, 2006.

[5] Jene. Golovchenko and Daniel. Branton. The Harvard Nanopore group - Nanopore Sequencing. http://labs.mcb.harvard.edu/branton/projects-NanoporeSequencing.htm.

[6] Adam R. Hall, Andrew Scott, Dvir Rotem, Kunal K. Mehta, Hagan Bayley, and Cees Dekker. Hybrid pore formation by directed insertion of α-haemolysin into solid-state nanopores. *Nature Nanotechnology*, 5(12):874–877, 2010.

[7] Stefan W Kowalczyk, Alexander Y Grosberg, Yitzhak Rabin, and Cees Dekker. Modeling the conductance and DNA blockade of solid-state nanopores. *Nanotechnology*, 22(31):315101, 2011.

[8] Rockin Science. Chondroitin Outperforms Celecoxib in Knee Osteoarthritis study, article on Rockin Science, 2015.

[9] Gowtham V Subbarao and Bert van den Berg. Crystal structure of the monomeric porin OmpG. *Journal of molecular biology*, 360(4):750–9, 2006.

[10] Carmay Lim and Todor Dudev. *Chapter 10. Potassium Versus Sodium Selectivity in Monovalent Ion Channel Selectivity . The Alkali Metal Ions: Their Role for Life*, volume 16 of *Metal Ions in Life Sciences*. Springer International Publishing, Cham, 2016.

[11] Céline Merstorf, Benjamin Cressiot, Manuela Pastoriza-Gallego, Abdelghani Oukhaled, Jean-Michel Betton, Loïc Auvray, and Juan Pelta. Wild Type, Mutant Protein Unfolding and Phase Transition Detected by Single-Nanopore Recording. *ACS Chemical Biology*, 7(4):652–658, 2012.

[12] Wallace H. Coulter. US 2656508, Means for counting particles suspended in a fluid, 1953.

[13] J J Kasianowicz, E Brandin, D Branton, and D W Deamer. Characterization of individual polynucleotide molecules using a membrane channel. *Proceedings of the National Academy of Sciences of the United States of America*, 93(24):13770–3, 1996.

[14] Bala Murali Venkatesan and Rashid Bashir. Nanopore sensors for nucleic acid analysis. *Nature Nanotechnology*, 6(10):615–624, 2011.

[15] Eric Beamish. *Precise Size Control and Noise Reduction of Solid- State Nanopores for the Detection of Dna-Protein Complexes*. PhD thesis, 2012.

[16] Michael K. Miller, Kaye F. Russell, Keith Thompson, Roger Alvis, and David J. Larson. Review of Atom Probe FIB-Based Specimen Preparation Methods. *Microscopy and Microanalysis*, 13(06):428–436, 2007.

[17] Furat Sawafta, Autumn T Carlsen, and Adam R Hall. Membrane thickness dependence of nanopore formation with a focused helium ion beam. *Sensors (Basel, Switzerland)*, 14(5):8150–61, 2014.

[18] A.L. Biance, J. Gierak, E. Bourhis, A. Madouri, X. Lafosse, G. Patriarche, G. Oukhaled, C. Ulysse, J.C. Galas, Y. Chen, and L. Auvray. Focused ion beam sculpted membranes for nanoscience tooling. *Microelectronic Engineering*, 83(4-9):1474–1477, 2006.

[19] Mickael Lillo and Dusan Losic. Ion-beam pore opening of porous anodic alumina: The formation of single nanopore and nanopore arrays. *Materials Letters*, 63(3):457–460, 2009.

[20] Jack Zhou and Guoliang Yang. Focused Ion-Beam Based Nanohole Modeling, Simulation, Fabrication, and Application. *Journal of Manufacturing Science and Engineering*, 132(1):011005, 2010.

[21] J. Gierak, A. Madouri, A.L. Biance, E. Bourhis, G. Patriarche, C. Ulysse, D. Lucot, X. Lafosse, L. Auvray, L. Bruchhaus, and R. Jede. Sub-5nm FIB direct patterning of nanodevices. *Microelectronic Engineering*, 84(5):779–783, 2007.

[22] B. Schiedt, L. Auvray, L. Bacri, G. Oukhaled, A. Madouri, E. Bourhis, G. Patriarche, J. Pelta, R. Jede, and J. Gierak. Direct FIB fabrication and integration of single nanopore devices for the manipulation of macromolecules. *Microelectronic Engineering*, 87(5):1300–1303, 2010.

[23] Zifan Tang, Daihua Zhang, Weiwei Cui, Hao Zhang, Wei Pang, and Xuexin Duan. Fabrications, Applications and Challenges of Solid-state Nanopores: A Mini Review. *Nanomaterials and Nanotechnology*, page 1, 2016.

[24] A. J. Storm, J. H. Chen, H. W. Zandbergen, and C. Dekker. Translocation of double-strand DNA through a silicon oxide nanopore. *Physical Review E*, 71(5):051903, 2005.

[25] Jiunn B Heng, Chuen Ho, Taekyung Kim, Rolf Timp, Aleksij Aksimentiev, Yelena V Grinkova, Stephen Sligar, Klaus Schulten, and Gregory Timp. Sizing DNA using a nanometer-diameter pore. *Biophysical journal*, 87(4):2905–11, 2004.

[26] Diego Krapf, Meng-Yue Wu, Ralph M. M. Smeets, Henny W. Zandbergen, Cees Dekker, , and Serge G. Lemay. Fabrication and Characterization of Nanopore-Based Electrodes with Radii down to 2 nm. *Nano letters*, 2005.

[27] Henny W. Zandbergen, Robert J. H. A. van Duuren, Paul F. A. Alkemade, Günther Lientschnig, Oscar Vasquez, Cees Dekker, , and Frans D. Tichelaar. Sculpting Nanoelectrodes with a Transmission Electron Beam for Electrical and Geometrical Characterization of Nanoparticles. *Nano letters*, 2005.

[28] Min Jun Kim, Meni Wanunu, David C. Bell, and Amit Meller. Rapid fabrication of uniformly sized nanopores and nanopore arrays for parallel DNA analysis. *Advanced Materials*, 18(23):3149–3153, 2006.

[29] Hung Chang, Samir M. Iqbal, Eric A. Stach, Alexander H. King, Nestor J. Zaluzec, and Rashid Bashir. Fabrication and characterization of solid-state nanopores using a field emission scanning electron microscope. *Applied Physics Letters*, 88(10):103109, 2006.

[30] Tao Deng, Jian Chen, Weihua Si, Ming Yin, Wen Ma, and Zenwen Liu. Fabrication of silicon nanopore arrays using a combination of dry and wet etching. *Journal of Vacuum Science & Technology B: Microelectronics and Nanometer Structures*, 30(6):061804, 2012.

[31] J B Heng, A Aksimentiev, C Ho, V Dimitrov, T Sorsch, J Miner, W Mansfield, K Schulten, and G Timp. Beyond the Gene Chip. *Bell Labs technical journal*, 10(3):5–22, 2005.

[32] F. Traversi, C. Raillon, S. M. Benameur, K. Liu, S. Khlybov, M. Tosun, D. Krasnozhon, A. Kis, and A. Radenovic. Detecting the translocation of DNA through a nanopore using graphene nanoribbons. *Nature Nanotechnology*, 8(12):939–945, 2013.

[33] Mingsheng Xu, Robert G. Endres, and Yasuhiko Arakawa. The Electronic Properties of DNA Bases. *Small*, 3(9):1539–1543, 2007.

[34] X-G Zhang, Predrag S Krstić, Radomir Zikić, Jack C Wells, and Miguel Fuentes-Cabrera. First-principles transversal DNA conductance deconstructed. *Biophysical journal*, 91(1):L04–6, 2006.

[35] Amit Meller. Dynamics of polynucleotide transport through nanometre-scale pores. *Journal of Physics: Condensed Matter*, 15(17):R581–R607, 2003.

[36] Massimo Bernaschi, Simone Melchionna, Sauro Succi, Maria Fyta, and Efthimios Kaxiras. Quantized Current Blockade and Hydrodynamic Correlations in Biopolymer Translocation through Nanopores: Evidence from Multiscale Simulations. *Nano letters*, 2008.

[37] Arnold J. Storm, Cornelis Storm, Jianghua Chen, Henny Zandbergen, Jean-François Joanny, , and Cees Dekker. Fast DNA Translocation through a Solid-State Nanopore. *Nano letters*, 2005.

[38] F Sanger, S Nicklen, and A R Coulson. DNA sequencing with chain-terminating inhibitors. *Proceedings of the National Academy of Sciences of the United States of America*, 74(12):5463–7, 1977.

[39] Jiali Li, Marc Gershow, Derek Stein, Eric Brandin, and J. A. Golovchenko. DNA molecules and configurations in a solid-state nanopore microscope. *Nature Materials*, 2(9):611–615, 2003.

[40] James Clarke, Hai-Chen Wu, Lakmal Jayasinghe, Alpesh Patel, Stuart Reid, and Hagan Bayley. Continuous base identification for single-molecule nanopore DNA sequencing. *Nature Nanotechnology*, 4(4):265–270, 2009.

[41] Christopher M. Dobson. Protein misfolding, evolution and disease. *Trends in biochemical sciences*, 24(9):329–32, 1999.

[42] Erik C. Yusko, Jay M. Johnson, Sheereen Majd, Panchika Prangkio, Ryan C. Rollings, Jiali Li, Jerry Yang, and Michael Mayer. Controlling protein translocation through nanopores with bio-inspired fluid walls. *Nature Nanotechnology*, 6(4):253–260, 2011.

[43] Zewen Liu, Yifan Wang, Tao Deng, Qi Chen, Zewen Liu, Yifan Wang, Tao Deng, and Qi Chen. Solid-State Nanopore-Based DNA Sequencing Technology. *Journal of Nanomaterials*, 2016:1–13, 2016.

[44] Silvia Hernández-Ainsa, Nicholas A. W. Bell, Vivek V. Thacker, Kerstin Göpfrich, Karolis Misiunas, Maria Eugenia Fuentes-Perez, Fernando Moreno-Herrero, and Ulrich F. Keyser. DNA Origami Nanopores for Controlling DNA Translocation. *ACS Nano*, 2013.

[45] Vincent Tabard-Cossa, Dhruti Trivedi, Matthew Wiggin, Nahid N Jetha, and Andre Marziali. Noise analysis and reduction in solid-state nanopores. *Nanotechnology*, 18(30):305505, 2007.

[46] Yael Liebes, Maria Drozdov, Yotam Y. Avital, Yaron Kauffmann, Hanna Rapaport, Wayne D. Kaplan, and Nurit Ashkenasy. Reconstructing solid state nanopore shape from electrical measurements. *Applied Physics Letters*, 97(22):223105, 2010.

[47] Cameron M. Frament and Jason R. Dwyer. Conductance-Based Determination of Solid-State Nanopore Size and Shape: An Exploration of Performance Limits. *The journal of physical chemistry C*, 2012.

[48] R. Qiao and N. R. Aluru. Ion concentrations and velocity profiles in nanochannel electroosmotic flows. *The Journal of Chemical Physics*, 118(10):4692, 2003.

[49] Hui Liu, Shizhi Qian, and Haim H Bau. The effect of translocating cylindrical particles on the ionic current through a nanopore. *Biophysical journal*, 92(4):1164–77, 2007.

[50] Henry S. White and Andreas Bund. Ion current rectification at nanopores in glass membranes. *Langmuir*, 24(5):2212–2218, 2008.

[51] Shizhi. Qian and Ye. Ai. *Electrokinetic particle transport in micro-/nanofluidics : direct numerical simulation analysis. Chapter 2 : Numerical Simulations of Electrical Double Layer and Electroosmotic Flow in a Nanopore*. 2012.

[52] Jeremy Golden, Harris Miller, Dan Nawrocki, Jack Ross, AZ5412E, Dissolution Rate, Seite Von, Abschnitt Bezeichnung, Usa-ma Newton, Germany Tel, Process Flow, Technical Data Sheet, and General Information. LOR and PMGI Resists. *Transition*, (617):1–6, 2012.

[53] Chuen Ho, Rui Qiao, Jiunn B Heng, Aveek Chatterjee, Rolf J Timp, Narayana R Aluru, and Gregory Timp. Electrolytic transport through a synthetic nanometer-diameter pore. *Proceedings of the National Academy of Sciences of the United States of America*, 102(30):10445–50, 2005.

[54] S. H. Behrens and D. G. Grier. The charge of glass and silica surfaces. *Journal of Chemical Physics*, 115(14):6716–6721, 2001.

[55] Eric Beamish, Harold Kwok, Vincent Tabard-Cossa, and Michel Godin. Fine-tuning the Size and Minimizing the Noise of Solid-state Nanopores. *Journal of Visualized Experiments*, (80):e51081–e51081, 2013.

[56] Qingtao Li, Qing Zhao, Bo Lu, Hengbin Zhang, Song Liu, Zhipeng Tang, Lijia Qu, Rui Zhu, Jingmin Zhang, Liping You, Fuhua Yang, and Dapeng Yu. Size evolution and surface characterization of solid-state nanopores in different aqueous solutions. *Nanoscale*, 4(5):1572, 2012.

[57] J E Hall. Access resistance of a small circular pore. *The Journal of general physiology*, 66(4):531–2, 1975.

[58] D Woermann. Analysis of non-ohmic electrical currentvoltage characteristic of membranes carrying a single track-etched conical pore. *Nuclear Instruments and Methods in Physics Research Section B: Beam Interactions with Materials and Atoms*, 194(4):458–462, 2002.

[59] D Woermann. Electrochemical transport properties of a cone-shaped nanopore: high and low electrical conductivity states depending on the sign of an applied electrical potential difference. *Physical Chemistry Chemical Physics*, 5(9):1853–1858, 2003.

[60] D Woermann. Electrochemical transport properties of a cone-shaped nanopore: revisited. *Physical Chemistry Chemical Physics*, 6(12):3130, 2004.

[61] Bala Murali Venkatesan, Amish B. Shah, Jian-Min Zuo, and Rashid Bashir. DNA Sensing Using Nanocrystalline Surface-Enhanced Alumina Nanopore Sensors. *Advanced Functional Materials*, 20(8):1266–1275, 2010.

[62] M T Bayliss, D Osborne, S Woodhouse, and C Davidson. Sulfation of chondroitin sulfate in human articular cartilage. The effect of age, topographical position, and zone of cartilage on tissue composition. *The Journal of biological chemistry*, 274(22):15892–900, 1999.

[63] https://en.wikipedia.org/wiki/Glycosaminoglycan.

[64] Cristal I Gama, Sarah E Tully, Naoki Sotogaku, Peter M Clark, Manish Rawat, Nagarajan Vaidehi, William A Goddard, Akinori Nishi, and Linda C Hsieh-Wilson. Sulfation patterns of glycosaminoglycans encode molecular recognition and activity. *Nature chemical biology*, 2(9):467–73, 2006.

[65] Seema Patel. Therapeutic importance of sulfated polysaccharides from seaweeds: updating the recent findings. *3 Biotech*, 2(3):171–185, 2012.

[66] Arnaud Baslé, Ram Iyer, and Anne H Delcour. Subconductance states in OmpF gating. *Biochimica et Biophysica Acta (BBA) - Biomembranes*, 1664(1):100–107, 2004.

[67] Eva K Schmitt, Maarten Vrouenraets, and Claudia Steinem. Channel activity of OmpF monitored in nano-BLMs. *Biophysical journal*, 91(6):2163–71, 2006.

[68] Ozkan Yildiz, Kutti R Vinothkumar, Panchali Goswami, and Werner Kühlbrandt. Structure of the monomeric outer-membrane porin OmpG in the open and closed conformation. *The EMBO journal*, 25(15):3702–13, 2006.

[69] Shizhi. Qian and Ye. Ai. Electrokinetic particle transport in micro-/nanofluidics : direct numerical simulation analysis. Chapter 8 : Electrokinetic Translocation of a Cylindrical Particle through a Nanopore. 2012.

[70] S S Rezaie, U Rengarajan, H Hoi, C Montemagno, and M Gupta. Selective plasma activation of surfaces for biosensing application. 43rd IEEE International Conference on Plasma Science, June 19 23, 2016. Banff, AB.

Appendix A

A.1 KOH etch of silicon and Photomask pattern dimension calculation

The dimensions of free standing membrane can be theoretically calculated by predetermining the pattern opening size, D the on PECVD SiN_x (assuming a square shaped opening with side length D). It is known that KOH etches silicon preferentially along (100) plane at an angle of 54.7° (θ). When the thickness of silicon wafer to be etched using KOH is H, then the square shaped free standing membrane side length d, can be determined by using the equation,

$$d = D - 2H\cot(\theta) \tag{A.1}$$

The equation can be used to theoretically determine the required pattern size D, prior to photomask fabrication. This size can be altered accordingly to obtain a smaller or larger free standing SiN_x surface. Figure A.1 shows the schematic image of KOH etch with appropriate dimensions and layers marked.

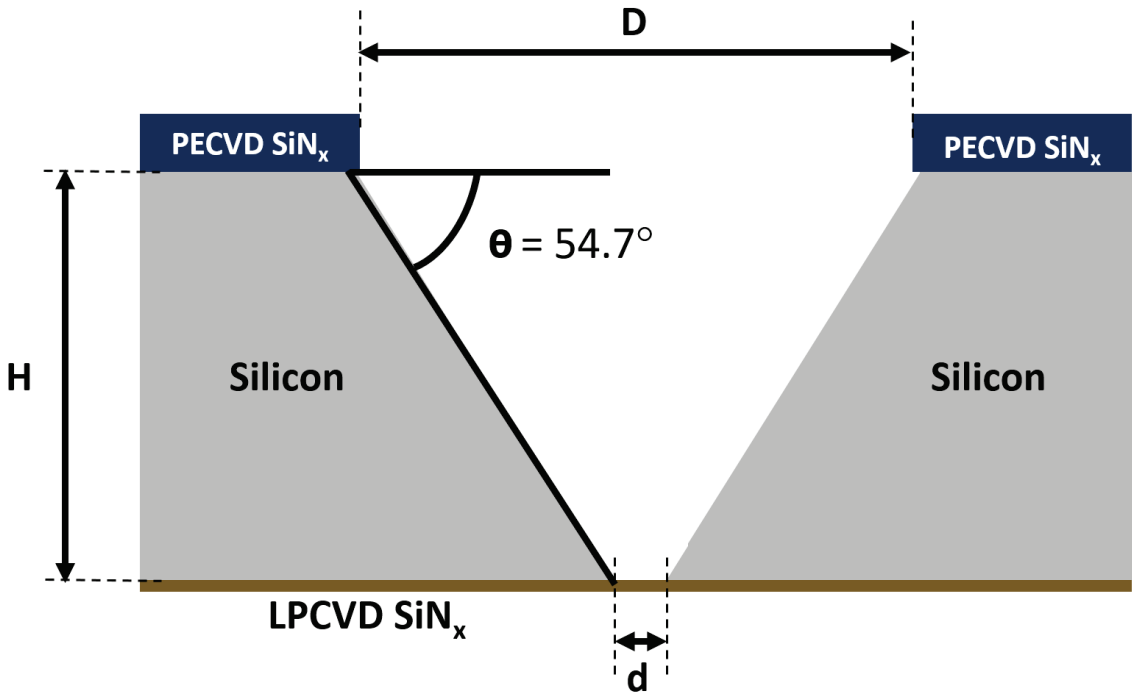

Figure A.1: Schematic of KOH etch through a silicon wafer along the (100) plane at an angle of 54.7°, with appropriate dimensions and layers marked.

Appendix B

B.1 Nanopore array characterization

A nanopore array with 8 conically shaped (half cone angle $\sim 4°$) pores on a single free standing SiN_x membrane was fabricated using TEM. Figure B.1(a) shows the image of the pore array with pore size ranging from around 2.7 nm to 4 nm. The membrane had 4 pores with size $\sim$ 2.7 nm and the rest of the pores with size $\sim$ 4 nm. The estimated conductance of such an array (sum of all pore conductance) was calculated (from COMSOL simulation) to be around 39.5 nS. Experimental characterization of the nanopore array displayed a conductance of $\sim$ 31 nS (this difference could be because of improper wetting of some of the pores, resulting in lower than expected conductance or due to pore size variation during experimentation). Figure B.1(b) shows the measured current for the corresponding applied bias across the nanopore array. Array of nanopores when fabricated with uniform size and shape can be used for analyzing translocation of higher amount of analyte sample as compared to single nanopore. The array of nanopores can also be patterned and used to perform parallel analyte detection (with additional measurement setups).

B.2 OmpG characterization in lipid bilayer

Engineered OmpG protein was characterized in different lipid bilayers, namely DPhPC and POPG/POPE. Protein gating was observed at 50 mV applied potential in 1 M NaCl buffer (pH 8.0). This characterization measurement was performed by Jeanine Koshelek and Dr. Hiofan Hoi. Figure B.2 shows the characterization and gating ability of OmpG in different lipids.

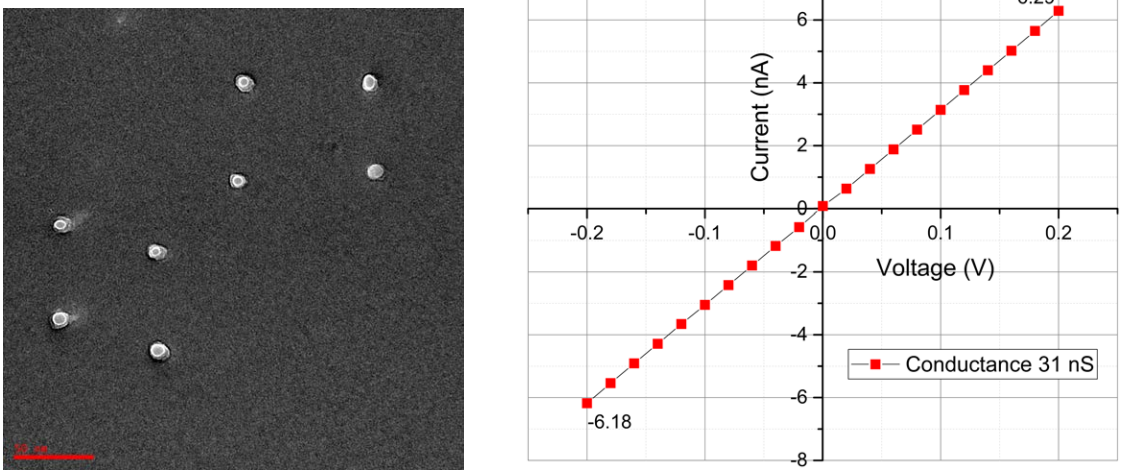

(a) (b)

Figure B.1: (a) TEM image of 8 pore array with conical pores ranging in size from 2.7 nm to 4 nm. (b) Plot of current vs applied bias measured for the 8 pore array in 1M KCl, to measure the conductance.

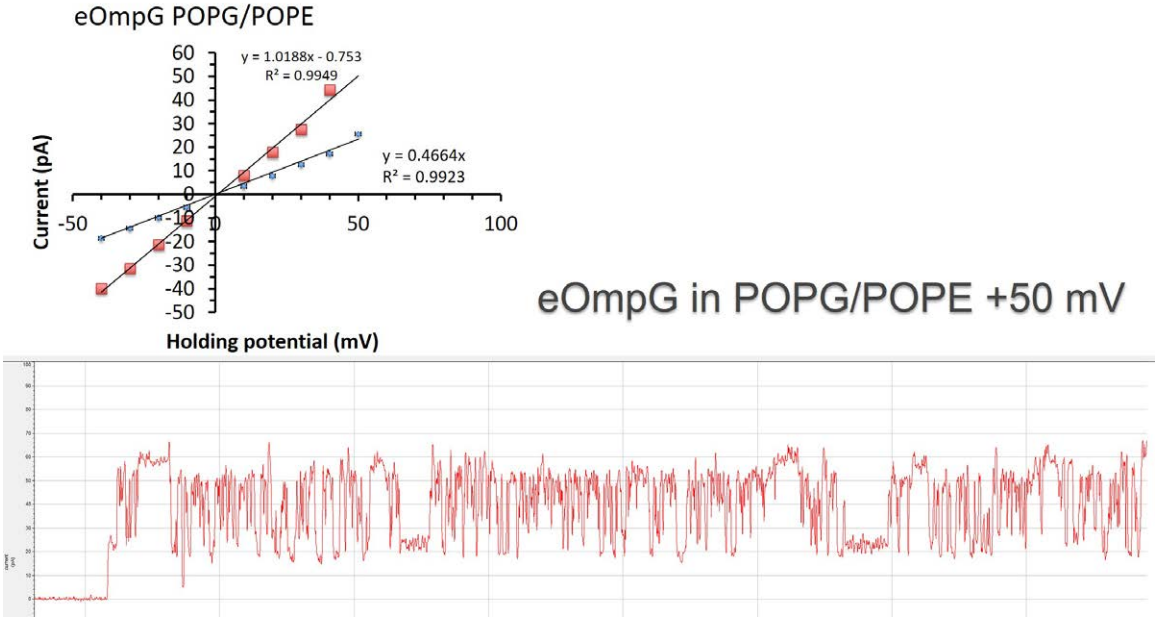

(a)

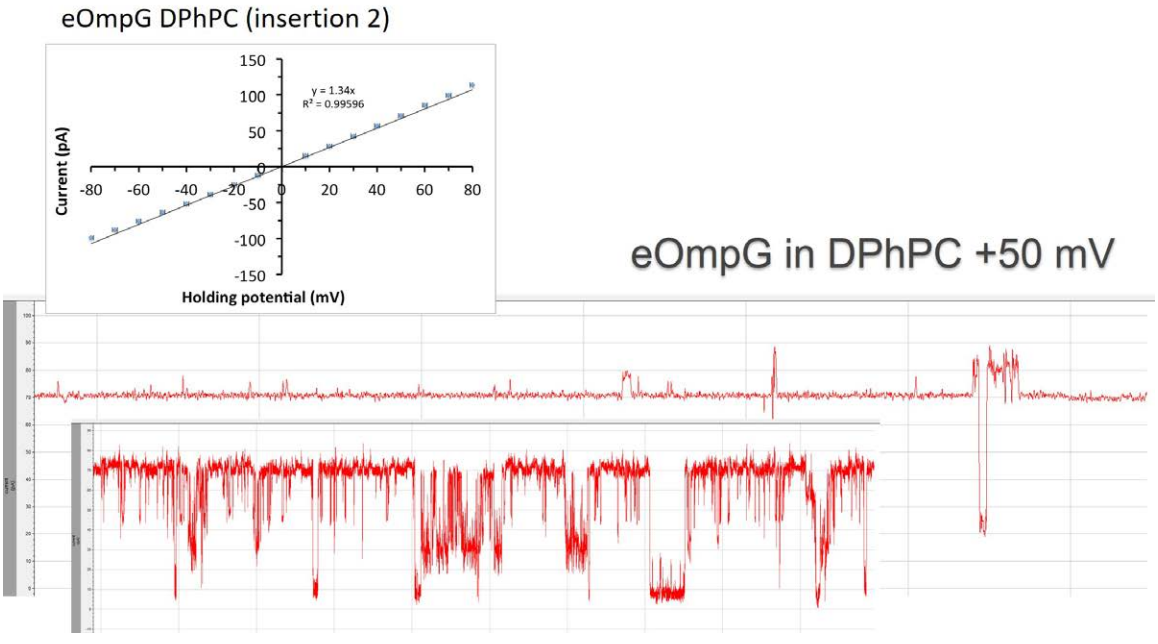

(b)

Figure B.2: OmpG characterization and gating in different lipids (a) POPG/POPE, (b) DPhPC.